

ระเบียบวิธีสเกลบาวดารีไฟไนต์เอลิเมนต์สำหรับปัญหาการค้ำของแผ่นบาง

นางสาวสิริพร ทองปากน้ำ

จุฬาลงกรณ์มหาวิทยาลัย
CHULALONGKORN UNIVERSITY

บทคัดย่อและแฟ้มข้อมูลฉบับเต็มของวิทยานิพนธ์ตั้งแต่ปีการศึกษา 2554 ที่ให้บริการในคลังปัญญาจุฬาฯ (CUIR)
เป็นแฟ้มข้อมูลของนิสิตเจ้าของวิทยานิพนธ์ ที่ส่งผ่านทางบัณฑิตวิทยาลัย

The abstract and full text of theses from the academic year 2011 in Chulalongkorn University Intellectual Repository (CUIR)
are the thesis authors' files submitted through the University Graduate School.

วิทยานิพนธ์นี้เป็นส่วนหนึ่งของการศึกษาตามหลักสูตรปริญญาวิศวกรรมศาสตรมหาบัณฑิต

สาขาวิชาวิศวกรรมโยธา ภาควิชาวิศวกรรมโยธา

คณะวิศวกรรมศาสตร์ จุฬาลงกรณ์มหาวิทยาลัย

ปีการศึกษา 2559

ลิขสิทธิ์ของจุฬาลงกรณ์มหาวิทยาลัย

THE SCALED BOUNDARY FINITE ELEMENT METHOD FOR PLATE
BENDING PROBLEMS

Miss Siriporn Thongpaknum



A Thesis Submitted in Partial Fulfillment of the Requirements
for the Degree of Master of Engineering Program in Civil Engineering
Department of Civil Engineering
Faculty of Engineering
Chulalongkorn University
Academic Year 2016
Copyright of Chulalongkorn University

Thesis Title	THE SCALED BOUNDARY FINITE ELEMENT METHOD FOR PLATE BENDING PROBLEMS
By	Miss Siriporn Thongpaknum
Field of Study	Civil Engineering
Thesis Advisor	Associate Professor Jaroon Rungamornrat, Ph.D.

Accepted by the Faculty of Engineering, Chulalongkorn University in
Partial Fulfillment of the Requirements for the Master's Degree

..... Dean of the Faculty of Engineering
(Associate Professor Supot Teachavorasinskun, Ph.D.)

THESIS COMMITTEE

..... Chairman
(Professor Teerapong Senjuntichai, Ph.D.)

..... Thesis Advisor
(Associate Professor Jaroon Rungamornrat, Ph.D.)

..... Examiner
(Associate Professor Akhrawat Lenwari, Ph.D.)

..... External Examiner
(Assistant Professor Kitjapat Phuvoravan, Ph.D.)

CHULALONGKORN UNIVERSITY

สิริพร ทองปากน้ำ : ระเบียบวิธีสเกลบาวดารีไฟไนต์เอลิเมนต์สำหรับปัญหาการดัดของแผ่นบาง (THE SCALED BOUNDARY FINITE ELEMENT METHOD FOR PLATE BENDING PROBLEMS) อ.ที่ปรึกษาวิทยานิพนธ์หลัก: จรูญ รุ่งอมรรัตน์, 79 หน้า.

วิทยานิพนธ์ฉบับนี้ได้นำเสนอขั้นตอนการหาผลเฉลยถึงวิเคราะห์โดยระเบียบวิธีสเกลบาวดารีไฟไนต์เอลิเมนต์สำหรับจำลองแผ่นบางภายใต้แรงกระทำตามขวางและเงื่อนไขขอบเขตแบบต่างๆกัน สมการกำกับหลักสร้างภายใต้กรอบทฤษฎีแผ่นดัดของเคอร์ซอฟฟ์ และใช้ระเบียบวิธีถ่วงน้ำหนักคงค้ำมาตรฐานร่วมกับการประมาณในทิศทางสเกลบาวดารีในการพัฒนาสมการสเกลบาวดารีไฟไนต์เอลิเมนต์ วิธีการพื้นฐานเชิงคำนวณ อาทิเช่น การหาค่าปริพันธ์เชิงตัวเลข การหาค่าลักษณะเฉพาะกับเวกเตอร์ลักษณะเฉพาะ การแก้ระบบสมการเชิงอนุพันธ์เชิงเส้น และการหาผลเฉลยของระบบสมการเชิงเส้น ได้ถูกนำมาใช้ในการหาฟังก์ชันไม่ทราบค่าที่เกี่ยวข้อง ขั้นตอนลำดับขั้นปรับได้แบบเอช โดยใช้โมเมนต์กู่คีนในการประมาณการค่าความคลาดเคลื่อนของผลเฉลยถูกนำมาใช้ร่วมกับระเบียบวิธีสเกลบาวดารีไฟไนต์เอลิเมนต์เพื่อเพิ่มสมรรถนะด้านการคำนวณและลดค่าใช้จ่ายในการสร้างโครงตาข่ายสำหรับการประมาณ ผลที่รายงานในวิทยานิพนธ์ฉบับนี้แสดงให้เห็นถึงความถูกต้องและการลู่เข้าของผลเฉลย และสมรรถนะด้านการคำนวณของระเบียบวิธีที่พัฒนาขึ้น

จุฬาลงกรณ์มหาวิทยาลัย
CHULALONGKORN UNIVERSITY

ภาควิชา วิศวกรรมโยธา

สาขาวิชา วิศวกรรมโยธา

ปีการศึกษา 2559

ลายมือชื่อนิสิต

ลายมือชื่อ อ.ที่ปรึกษาหลัก

5670578921 : MAJOR CIVIL ENGINEERING

KEYWORDS: PLATE BENDING / SBFEM / H-HIERARCHICAL ADAPTIVITY /
MOMENT-RECOVERY ERROR ESTIMATOR / KIRCHHOFF'S PLATE
BENDING THEORY

SIRIPORN THONGPAKNUM: THE SCALED BOUNDARY FINITE
ELEMENT METHOD FOR PLATE BENDING PROBLEMS. ADVISOR:
ASSOC. PROF. JAROON RUNGAMORN RAT, Ph.D., 79 pp.

This thesis presents an efficient and accurate semi-analytical solution procedure, based upon the scaled boundary finite element method (SBFEM), for modeling thin plates under transverse loadings and different types of boundary conditions. The key formulation is established within the framework of Kirchhoff's plate bending theory. A standard weighted residual technique is then applied together with the discretization along the scaled boundary direction to derive the scaled boundary finite element equations. Standard implementations including the numerical integration, the determination of eigenvalues and eigenvectors, a procedure for solving a system of linear ordinary differential equations, and a linear solver are adopted to construct all involved unknown functions. An h -hierarchical adaptive procedure with the moment-recovery error estimator is also integrated into the present implementation to further enhance its computational performance and reduce meshing effort. A selected set of results is reported to demonstrate the accuracy and convergence of computed solutions and the computational performance of the developed technique.

Department: Civil Engineering

Student's Signature

Field of Study: Civil Engineering

Advisor's Signature

Academic Year: 2016

ACKNOWLEDGEMENTS

Firstly, I would like to express my deepest gratitude to my advisor, Associate Professor Dr. Jaroon Rungamornrat for the kindness, for the continuous encouragement and the never ending support throughout this study. I would have never made it without his guidance, patience, and understanding. Their exhortation helped me throughout the research and the development of this thesis. Besides my advisor, I would like to thank the rest of my thesis chairman and committee: Professor Dr. Teerapong Senjuntichai, Associate Professor Dr. Akhrawat Lenwari and Assistant Professor Dr. Kitjapat Phuvoravan for their encouragement and kindly recommendations.

My sincere thanks also go to Chulalongkorn University and Thailand Research Fund 2015, which provided me an opportunity to study master degree in Chulalongkorn University for this study.

Last but not least, my foremost thanks and greatest gratitude goes to my beloved family for their moral support and unconditional help. Without my family, I would not have made it this far. Also I thank my friends in the following institution for their psychological support throughout the development of this thesis.

CONTENTS

	Page
THAI ABSTRACT	iv
ENGLISH ABSTRACT.....	v
ACKNOWLEDGEMENTS	vi
CONTENTS.....	vii
LIST OF TABLES	ix
LIST OF FIGURES	x
CHAPTER 1 INTRODUCTION	1
1.1 Motivation and Significance.....	1
1.2 Background and Review	4
1.2.1 Plate bending problems	4
1.2.2 Scaled boundary finite element method	5
1.2.3 Scaled boundary finite element method for plate bending problems	6
1.2.4 An h -hierarchical adaptive	10
1.2.5 An h -hierarchical adaptive for scaled boundary finite element method	10
1.3 Research Objectives.....	11
1.4 Scope of Work	11
1.5 Research Methodology	11
1.6 Anticipated Outcome and Contribution.....	12
CHAPTER 2 PROBLEM FORMULATION	14
2.1 Problem Description	14
2.2 Basic Equations	15
2.3 Weak Formulation	16
CHAPTER 3 SCALED BOUNDARY FINITE ELEMENT FORMULATION.....	18
3.1 Scaled Boundary Coordinate Transformation	18
3.2 Scaled Boundary Finite Element Approximation.....	21
3.2.1 Approximation of Geometry	21
3.2.2 Approximation of Solution and Weight Function.....	23
3.3 Scaled Boundary Finite Element Equations	24

	Page
CHAPTER 4 SOLUTION METHODOLOGY	31
4.1 Determination of Homogeneous Solution	31
4.2 Determination of Particular Solution	32
4.3 Final General Solution	36
4.4 Post-Process for Field Quantities	38
CHAPTER 5 H-HIERARCHICAL ADAPTIVITY	39
5.1 Moments-recovery and Error Estimation	39
5.2 An h -hierarchical Adaptive Procedure	41
CHAPTER 6 NUMERICAL RESULTS	43
6.1 Verifications	43
6.1.1 Circular plate with concentric hole under transverse shear	43
6.1.2 Circular plate under applied moment	47
6.1.3 Circular plate with concentric hole under applied moment	49
6.1.4 Circular plate with concentric hole under applied moments	52
6.1.5 Trapezoidal plate under transverse shear	55
6.2 Results from h -hierarchical adaptive SBFEM	59
6.2.1 Circular plate with concentric hole under transverse shear	59
6.2.2 Circular plate with concentric hole under partially loaded transverse shear	62
6.2.3 Semi-circular plate subjected to sinusoidal transverse shear	66
6.2.4 Trapezoidal plate under partially loaded transverse shear	70
CHAPTER 7 CONCLUSIONS AND REMARKS	74
REFERENCES	75
VITA	79

LIST OF TABLES

Table 1.1: Comparisons of features among BEM, FEM, and SBFEM.....	9
Table 6.1: Deflection at point A for circular plate containing concentric circular hole clamped along its outer boundary and loaded by uniform transverse shear load along inner boundary for various ratios of t/b	44
Table 6.2: Radial bending moment at point B ($M_r \times 10^2$) for circular plate containing concentric circular hole clamped along its outer boundary and loaded by uniform transverse shear load along inner boundary for various ratios of t/b	45
Table 6.3: Radial rotation at point A (θ_r) for circular plate containing concentric circular hole clamped along its outer boundary and loaded by uniform transverse shear load along inner boundary for various ratios of t/b	45
Table 6.4: Deflection for simply-supported, elastic, circular plate subjected to distributed moments along its boundary.	47
Table 6.5: Deflection along radial direction of circular plate containing concentric circular hole and subjected to uniform moments along its inner boundary.	51
Table 6.6: Deflection for circular plate containing concentric circular hole and subjected moments along its inner and outer boundaries for $t/b = 0.05$	53
Table 6.7: Transverse displacement at points A, B and C of trapezoidal plate (mm) loaded by uniform transverse shear force along the outer boundary.	58
Table 6.8: Comparison of computational performance of USBFEM and ASBFEM for circular plate with concentric hole under partially loaded transverse shear	63
Table 6.9: Comparison of computational performance of USBFEM and ASBFEM for semi-circular plate with concentric semi-circular hole under sinusoidal transverse shear	67
Table 6.10: Comparison of computational performance of USBFEM and ASBFEM for trapezoidal plate clamped along shorter paralleled side and subjected to linearly distributed transverse shear along longer paralleled side	71

LIST OF FIGURES

Figure 1.1: (a) Schematic of flat slab (Photo by <i>GEM NEXUS</i> , 2015 [1]) and (b) schematic of corresponding mathematical model (Photo by <i>National Geographic South Korea</i> , 2015 [2])	1
Figure 1.2: Schematic of stiffened web elements and unstiffened flange elements of structural steel beam (Adapted from “Steel Structures Design and Behavior”, by Charles and John, <i>Book of HarperCollins College Publishers</i> , 1996, fourth edition p.328 [3])	2
Figure 1.3: Notation of scaled boundary coordinate system for (a) bounded domain with side-faces and (b) unbounded domains with side-faces (figures are taken from the work of Deeks and Wolf [47]).....	6
Figure 1.4: Comparison of the maximum displacement obtained from SBFEM with different discretization and that from FEM with 30,000 degrees of freedom (This graph is taken directly from the work of Dieringer and Becker [23])......	7
Figure 2.1: Schematic of thin plate subjected to transverse and in-plane loadings	14
Figure 3.1: Schematic of scaling center x_0 and defining curve C used in the scaled boundary coordinate transformation	19
Figure 3.2: Schematic of a representative Ω and its approximation Ω^h . The dashed lines are used to represent the approximation of the defining curve, the inner and outer boundaries.....	25
Figure 5.1: Diagram indicating algorithm for h -hierarchical adaptive scheme in scaled boundary finite element method (Adapted from “The scaled boundary finite element method” by Wolf, J.P., 2003, <i>Book of John Wiley & Sons Ltd</i> , p. 336 [30])......	42
Figure 5.2: Local refinement strategies; an h -hierarchical refinement is related to a binary tree of two-node line elements (Adapted from “The scaled boundary finite element method” by Wolf, J.P., 2003, <i>Book of John Wiley & Sons Ltd</i> , p. 336 [30])......	42
Figure 6.1: Schematic of circular plate containing concentric circular hole clamped along its entire outer boundary and loaded by uniform transverse shear load along its entire inner boundary.....	43
Figure 6.2: Schematic of uniform meshes with 4, 8, 16, 32 and 64 two-node elements used in discretization of defining curve.....	44

Figure 6.3: Percent error of numerical solutions versus number of elements for circular plate containing concentric circular hole clamped along its outer boundary and loaded by uniform transverse shear load along inner boundary ($t/b = 0.05$)	46
Figure 6.4: Deflection at point A, radial bending moment at point B, and radial rotation at point A of circular plate containing concentric circular hole clamped along its outer boundary and loaded by uniform transverse shear load along inner boundary ($t/b = 0.05$)	46
Figure 6.5: Schematic of simply-supported, elastic, circular plate subjected to moments along its boundary	47
Figure 6.6: (a) Plot of deflection for simply-supported, elastic, circular plate subjected to distributed moments along its boundary and (b) mesh containing 4 elements.	48
Figure 6.7: Error in deflection of simply-supported, elastic, circular plate subjected to distributed moments along its boundary	48
Figure 6.8: Schematic of circular plate containing concentric circular hole and subjected to uniform moments along its inner boundary	49
Figure 6.9: Schematic of six meshes containing 4, 8, 16, 32, 64 and 128 elements used in discretization of defining curve.	50
Figure 6.10: Deflections along the radial direction of circular plate containing concentric circular hole and subjected to uniform moments along its inner boundary for different levels of discretization.	50
Figure 6.11: Percent error in deflection along the radial direction of circular plate containing concentric circular hole and subjected to uniform moments along its inner boundary.	51
Figure 6.12: Plots of (a) deflected shape, (b) moment M_{11}^h , (c) moment M_{22}^h , and (d) moments M_{12}^h of circular plate containing concentric circular hole and subjected to uniform moments along its inner boundary obtained from mesh with 8 element.	52
Figure 6.13: Schematic of elastic, circular plate containing concentric circular hole and subjected moments along its inner and outer boundaries.	52
Figure 6.14 : Maximum deflection of circular plate containing concentric circular hole and subjected moments along its inner and outer boundaries versus the number of elements used in discretization of defining curve for $t/b = 0.05$	54

Figure 6.15: Percent error of computed deflection of circular plate containing concentric circular hole and subjected moments along its inner and outer boundaries for $t/b = 0.05$	54
Figure 6.16: Bending moments M_{11}^h , M_{22}^h and M_{12}^h along circumferential direction of circular plate containing concentric circular hole and subjected moments along its inner and outer boundaries for $\xi = 0.5, 0.6, 0.7, 0.8, 0.9$ and 1	55
Figure 6.17: Deflected shape and contour plot of the deflection of circular plate containing concentric circular hole and subjected moments along its inner and outer boundaries obtained from mesh with 8 element and $t/b = 0.005$	55
Figure 6.18: Schematic of trapezoidal plate clamped along the inner boundary and loaded by uniform transverse shear along the outer boundary.	56
Figure 6.19: Schematic of six meshes used in discretization of defining curve of trapezoidal plate	56
Figure 6.20: Spectrum of eigenvalues for the discretization of plate with 10 elements	57
Figure 6.21: Maximum transverse displacement of trapezoidal plate versus number of elements used in discretization of defining curve.	57
Figure 6.22: (a) Deflections along the straight line = 8 mm for different levels of discretization and (b) deflections along the radial boundary for different levels of discretization.	58
Figure 6.23: Percent error of computed deflection of trapezoidal plate clamped along the inner boundary and loaded by uniform transverse shear along the outer boundary at points A, B and C.	59
Figure 6.24: Sequence of meshes resulting from the analysis by ASBFEM for target error $\eta^* = 0.001\%$	60
Figure 6.25: The energy norms of recovered moment and analytical moment obtained from [63].	61
Figure 6.26: Relationship between total error estimate $\bar{\eta}^*$ and the computational time using USBFEM and ASBFEM.	61
Figure 6.27: Bending moment along circumferential direction at $\xi = 1$ of circular plate with concentric circular hole loaded by transverse shear along its entire inner boundary.	62

Figure 6.28: Schematic of circular plate containing concentric hole, clamped at its outer boundary and subjected to transverse shear along $-\pi/6$ to $\pi/6$	63
Figure 6.29: Sequence of meshes resulting from the analysis by ASBFEM for target error $\eta^* = 1\%$	64
Figure 6.30: Bending moment along circumferential direction at the defining curve after adaptive process to target error.....	64
Figure 6.31: Relationship between total error estimate of computed moment and the number of degrees of freedom using USBFEM and ASBFEM.....	65
Figure 6.32: Relationship between total error estimate of computed moment and the computational time using USBFEM and ASBFEM.	65
Figure 6.33: Deflected shape and contour plot of transverse deflection for circular plate containing concentric circular hole, clamped at its outer boundary and subjected to partial transverse shear obtained from final mesh for target error $\eta^* = 1\%$	66
Figure 6.34: Schematic of semi-circular plate containing concentric semi-circular hole, clamped at its inner boundary and subjected to sinusoidal transverse shear at the outer boundary along $5\pi/6 \leq \theta \leq \pi$	66
Figure 6.35 : Sequence of meshes resulting from the analysis by ASBFEM for target error $\eta^* = 1\%$	68
Figure 6.36: Relationship between total error estimate of computed moment and the number of degrees of freedom using USBFEM and ASBFEM.....	69
Figure 6.37: Relationship between total error estimate of computed moment and the computational time using USBFEM and ASBFEM.	69
Figure 6.38: Deflected shape and contour plot of transverse deflection for semi-circular plate containing concentric semi-circular hole, clamped at its inner boundary and subjected to sinusoidal transverse shear obtained from final mesh for target error $\eta^* = 1\%$	70
Figure 6.39: Schematic of trapezoidal plate clamped along shorter paralleled side and subjected to linearly distributed transverse shear along longer paralleled side. ...	70
Figure 6.40: Sequence of meshes resulting from the analysis by ASBFEM for target error $\eta^* = 0.1\%$	71
Figure 6.41: Relationship between total error estimate of computed moment and the number of degrees of freedom using USBFEM and ASBFEM.....	72

Figure 6.42: Relationship between total error estimate of computed moment and the computational time using USBFEM and ASBFEM.72

Figure 6.43: Deflected shape and contour plot of transverse deflection for trapezoidal plate clamped along shorter paralleled side and subjected to linearly distributed transverse shear along longer paralleled side obtained from final mesh for target error $\eta^* = 0.1\%$ 73



CHAPTER 1

INTRODUCTION

In this chapter, the motivation and significance of the current research is first presented and then the background and review of relevant literatures indicating the historical development and recent advances of the scaled boundary finite element method (SBFEM) and its applications to the numerical analysis of plate bending problems is summarized. Next, research objectives, scope of work, methodology, and research procedure are clearly stated. Finally, the outcome and contribution of the present study are addressed.

1.1 Motivation and Significance

A plate is one of the most frequently encountered structural elements. Its behavior is considered quite important to structural designs and analyses. Plate structures are widely found in civil engineering applications and are encountered in many fields of construction technology. For this type of relatively thin structures, the bending mechanism has been found the main factor affecting the deformation perpendicular to the plane of the plate under the action of external forces and/or moments. The deflections can be determined by solving the differential equations resulting from proper plate theories to obtain the analytical solutions; however, these solutions are only limited to plates with simple geometries, boundary conditions, and loading conditions. To overcome these difficulties and disadvantages, the numerical solutions have been developed. The scaled boundary finite element method is one of attractive numerical techniques for modeling plate bending problems, which is considered the latest numerical technique that has been applied to solve several problems in applied mechanics with high achievement.



(a)



(b)

Figure 1.1: (a) Schematic of flat slab (Photo by *GEM NEXUS*, 2015 [1]) and (b) schematic of corresponding mathematical model (Photo by *National Geographic South Korea*, 2015 [2])

This research topic still remains popular due to the vast applications of plate structures especially found in broad engineering practices. A mathematical plate model, which is defined as a structure possessing one dimension much smaller than the other two, is often employed in the modeling because it provides valuable insight into the behavior of the structures and is computationally simple. An example of plate structures is the flat slab that transfers the load directly to columns without the use of beams as shown in Figure 1.1(a) and it can be modeled mathematically as illustrated in Figure 1.1(b). Another example of plate structures is a thin element of structural members such as web and flange of a beam under in-plane and out-of-plane loading conditions which transfers the transverse loads to the supports by bending and shear actions. In general, higher stresses are developed in flexural members in comparison with axially loaded members with the same level of applied load and the resulting deformation due to the bending mode is also much higher. The deflection of a beam due to the bending effect is often considered as one of the most significant factors of the design criteria. The behavior of the beam under loading as shown in Figure 1.2 has a similar characteristic to that of the plate bending theory.

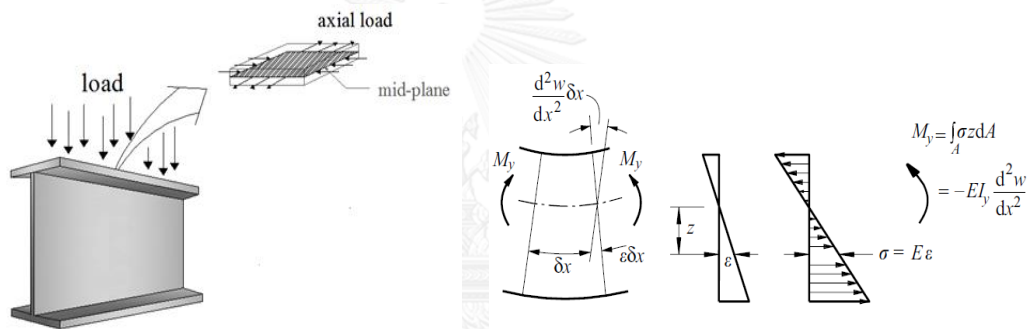


Figure 1.2: Schematic of stiffened web elements and unstiffened flange elements of structural steel beam (Adapted from “Steel Structures Design and Behavior”, by Charles and John, *Book of HarperCollins College Publishers*, 1996, fourth edition p.328 [3])

Various mathematical models have been continuously proposed to represent the behaviors of objects/bodies under different types of loading and boundary conditions. In principle, all models can be reduced to a partial differential equation system, a system of integral equations, or both depending mainly upon the type of problems and solution procedure to be employed. Nevertheless, the analytical approaches for solving those governing equations are commonly limited to problems with simple geometries and boundary conditions [4-6]. The need of more powerful solution techniques to overcome the limitation of analytical methods brings about the development of numerical techniques e.g. the finite element method (FEM) which has been used successfully and extensively for solving problems in applied mechanics. However, the FEM also has some difficulties associated with its application in certain areas i.e. the static and dynamic analysis of large or unbounded domains, problems involving cracks/notches and singular fields, and other stress concentration problems [7-12].

To circumvent the inefficiency of the FEM to solve problems involving unbounded domains, another group of numerical techniques termed the boundary element method (BEM) has been established. In such group of techniques, the key

governing equations of the boundary value problems are expressed in terms of boundary integrals containing only unknowns on the boundary of the domain and, as a direct consequence, the discretization of the field variable is restricted to the domain boundary. It is worth noting that the governing integral equations underlying the BEM require the availability of essential fundamental solutions. In addition, the form of fundamental solutions is problem dependent and is generally complicated to be constructed since they are required to satisfy the governing differential equations exactly for the entire domain [13, 14]. Besides the reduction of spatial dimension associated with the unknown data, such major disadvantage is found to reduce the capability of the boundary element method to solve general boundary value problems in comparison to the FEM.

A novel numerical method capable of modeling the deformation of solids and structures, termed the scaled boundary finite element method (SBFEM), was introduced and has been widely used for the past three decades. The SBFEM combines the advantages and features of both analytical techniques and numerical approximations [15, 16], involves the approximation of the solution in the boundary direction, and generally yields a set of linear, ordinary, differential equations in the radial direction that can be solved analytically via simple schemes found in the theory of differential equations, e.g., the method of undetermined coefficients and the representation of solutions. The enforcement of boundary conditions and the assemblage of element coefficient matrices follow the standard procedure of the finite element method. Recently, the SBFEM has been successfully applied to solve several problems of continuum/solid mechanics such as electrostatic problems, problems in transient elastodynamics and unbounded domains, linear piezoelectric problems, stress analysis of cracked bodies and simulations of crack advances, biomaterials and multi-field materials, and thin plate and laminated plate problems [17-29]. Adaptive strategies have been also incorporated into the SBFEM to enhance its computational efficiency. The optimal mesh providing sufficiently accurate results while containing the number of degrees of freedom as small as possible is of interest. To ensure the computed result quality, the analyses are generally performed on several meshes with different sizes which drastically increase the overall cost of modeling and analysis. It is also known that the accuracy of approximate solutions depends primarily on the discretization level; the higher the level of discretization, the higher the accuracy of predicted results, but also the higher the number of degrees of freedom and the more the computational expense. An inadequate level of discretization can lead to inaccurate numerical solutions. Therefore, it is desirable to use the minimum number of degrees of freedom necessary in order to achieve the required level of accuracy preferred. To achieve this task in an efficient manner, the stress-recovery and the error estimation techniques were integrated into SBFEM along with the h -hierarchical adaptive procedure to solve both bounded and unbounded domains for linear elasticity problems [30, 31]. Normally, among the adaptive strategies, the h -refinement is the most essential one and it has been accomplished by using only a single type of elements.

Even though the SBFEM has been applied to several problems of applied mechanics with high success rate; heretofore, the SBFEM for modeling thin plates under transverse loadings and different types of boundary conditions with h -hierarchical adaptive procedure has not been implemented. This research presents an h -hierarchical adaptive scaled boundary finite element method for plate bending

problems. The governing equation is derived based primarily on Kirchhoff's plate theory while the weak formulation is obtained via a standard weighted residual technique. The scaled boundary finite element equations and the solution methodology follow the standard procedure of SBFEM. An h -hierarchical adaptive scheme with the moment-recovery error estimator is integrated in the implementation to obtain the optimal level of discretization for a specified level of accuracy.

1.2 Background and Review

In this section, the historical background and review of plate bending problems, adaptive procedure, and the scaled boundary finite element method are briefly discussed. In addition, applications of the scaled boundary finite element method to plate bending problems are also provided. The advantages and disadvantages of the scaled boundary finite element method in comparison with the finite element method, the boundary element method are also presented in this section.

1.2.1 Plate bending problems

The first simulation of plate problems, which was probably done by Euler in 1776, involved the free vibration analysis. Later on, Cauchy and Poisson were among the first who formulated the problem of plate bending based on theory of linear elasticity [32]. A plate theory reduces the full three-dimensional settings to two dimensional problems by taking into account the advantage of the disparity in the length scale. To further simplify the plate bending problems, Kirchhoff plate theory or thin plate theory was also introduced. Kirchhoff model is generally applied for relatively thin plates undergoing small deflections, negligible shear energy, and uncoupled membrane-bending action and also enforcing zero transverse shear strain at a selected location of the elements [33].

Solutions of plate bending problems can be obtained by means of analytical approaches; however, their inherent mathematical difficulties and analytical solutions restricted these problems to some simple geometries and boundary conditions [4-6, 34]. As mentioned earlier, for many plate problems of considerable practical interest, analytical solutions to the governing differential equations cannot be found; thus, numerical methods must be engaged to obtain approximate solutions. There are some effective numerical methods capable of performing the analysis of plates, such as the finite element method [35], the smoothed FEM [36, 37], the boundary element method [38, 39], and the Trefftz FEM [40, 41]. Various investigations mentioned earlier have led to the significant progress in efficiently modeling the plate bending problems while eliminating the locking phenomenon. In order to satisfy the C^1 -continuity requirement in the discretization of plate bending problems, high-order elements must be employed. In 1981, Tsach [25] investigated the relationship between the shear locking and the order of polynomials used in the approximation of the displacement. This work indicated that the lower order displacement-based elements normally produce results of stresses/internal-forces with lower accuracy and the high-order elements were less prone to shear locking. Zrahia and Bar-Yoseph [26] found similar results in their investigation that in comparison with low-order elements, the spectral elements lead to higher accuracy and computational efficiency. Similarly, Xenophontos et al. [27] developed the p -version mixed interpolation of tensorial component elements. Those p -MITC elements were extremely effective for plate problems, even when the curved

elements were used, provided that special care was taken in constructing the element mappings. In addition, Man et al. [42] employed high-order spectral elements together with the SBFEM in the analysis of plate structures and demonstrated that the technique yielded higher accuracy and faster convergence in comparison with the SBFEM using linear or quadratic elements and the p-MITC using linear or quadratic basis [42].

1.2.2 Scaled boundary finite element method

The primitive work with basic ideas in the scaled boundary finite element method under the name exterior finite elements for two-dimensional field problems with open boundaries was recognized by Silvester et al. [43]. In the SBFEM, only boundaries were discretized so that the modeled spatial dimensions were reduced by one similar to the BEM; however, it does not require the fundamental solutions. Figure 1.3 illustrates the scaled boundary coordinate system for both bounded and unbounded domains. The scaling center for a bounded medium is inside the domain and is generally chosen to be coincident with the origin of reference Cartesian coordinate system. The dimensionless radial coordinate ξ starts from the origin with $\xi = 0$ to the boundary where it is commonly normalized to unity, i.e., $\xi = 1$. The bounded domain is thus covered by $0 \leq \xi \leq 1$. The s-coordinate coincides with the circumferential direction on the domain boundary.

This method had originally been developed by Wolf and Song [44] to compute the dynamic stiffness of an unbounded domain in elastodynamics. Clearly, the consistent infinitesimal finite-element cell method does not require a fundamental solution. In addition, the free surface and the fixed boundaries and the layer interfaces between different materials extending from the structure-medium interface to infinity are incorporated automatically with later developments, allowing the analysis of incompressible materials and bounded domains [45] and the body loads inclusion [46]. The complexity of the original derivation of the technique was formulated by using a weighted residual approach and a mechanical-based approach to obtain the scaled boundary governing equations [16]. This solution procedure was clearly demonstrated by solving both homogenous bounded and unbounded media. Later, Deeks and Wolf [47] applied the principle of virtual work to derive the scaled boundary formulation. It was found that the semi-analytical SBFEM can be also obtained in a similar manner to the standard FEM and has the potential to be used with the great success rendering this method more accessible.

It has been shown that the SBFEM was highly benefits modeling stress singularities present at crack-tips by Zhenjun Yang [48] and, in addition, the developed methodology was capable of accurately and effectively predicting mixed-mode cracking paths and load–displacement relations for a wide range of problems. The SBFEM was also extended and employed in the modeling of two- and three-dimensional stress singularities in piezoelectric multi-material systems [49] and analysis of problems in transient elastodynamics [18]. All of the research studies indicated above showed that the SBFEM is an alternative, powerful and robust numerical technique useful for constructing approximate solutions of problems in applied mechanics. The scaled boundary finite element method can be classified as a combination of the boundary element method and the finite element method since only unknowns on the boundary appear in the key governing equation and the idea of finite element approximations is employed in the discretization. It also has appealing features of its own, for instance, the certain straight boundaries passing through the scaling

center are not necessary to be discretized. In addition, the SBFEM also combines the advantages of both numerical and analytical procedures. Features of the scaled boundary finite element method compared with those of the finite element and boundary element methods [15, 30] are indicated in Table 1.1.

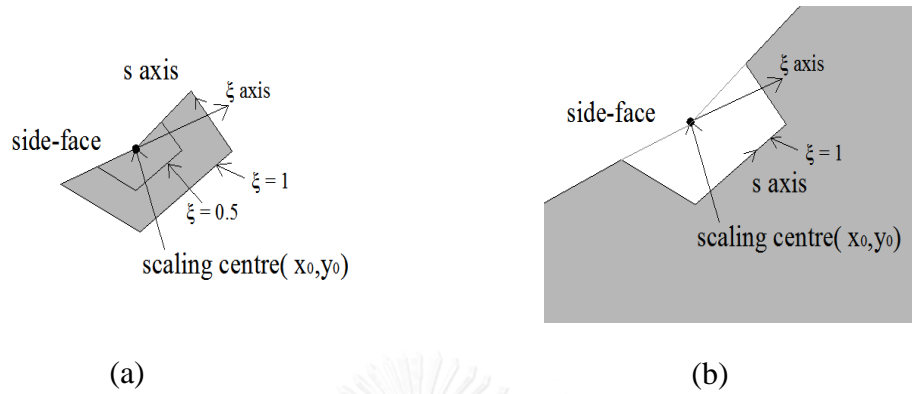


Figure 1.3: Notation of scaled boundary coordinate system for (a) bounded domain with side-faces and (b) unbounded domains with side-faces (figures are taken from the work of Deeks and Wolf [47])

While the SBFEM has been used successfully in the analysis of various classes of problems, the method still possesses some limitations and shortcomings. For example, the SBFEM has been developed mainly for solving problems with linear governing equations, although it was also applied to address nonlinear problems by a linearization of the physical problem prior to the SBFEM calculations [50]. The technique is also not flexible to deal with arbitrary material property distribution, although some specific distribution modes can be addressed. In this regards, the substructuring technique can be applied as a resort, although it introduces extra number of degrees of freedom [51]. Apart from this, the SBFEM has been found not competitive to the FEM in solving problems concerning bounded domain and when the smooth stress variations is present, but it outperforms the FEM in cases that the stress singularity appears even though a bounded computational domain is involved. With limited cases of drawbacks, the SBFEM has been applied to many engineering fields and has the great potential to further expand its applications.

1.2.3 Scaled boundary finite element method for plate bending problems

The application of the SBFEM to analyze plate problems under the framework of Kirchhoff's plate theory was first recognized in the work of Dieringer and Becker[23]. In their work, the principle of virtual work was employed to derive the scaled boundary equation by ignoring the transverse shear deformations and body loads and Hermitian polynomials of cubic order were used as the displacement shape functions. According to the virtual work equivalence, the scaled boundary equation of the transverse displacements was represented by the fourth-order eigenvalue. A system of Euler-Cauchy, ordinary differential equations, is then obtained from the scaled boundary finite element approximations. Applying a discrete form of the Kantorovich reduction method leads to a set of ordinary differential equations, which can be further solved in

a closed form. The assemblage of element stiffness matrices and the solution strategy can be preceded following the standard finite element procedure. Along the discretized boundaries, the approximation at present corners must be treated specially to ensure the satisfaction of the C^1 -continuity requirement since the gradient of the displacement may not be specified uniquely along the corner line of two adjacent elements. Various numerical examples have indicated that the SBFEM is efficient for solving plate bending problems. In particular, the number of the degrees of freedom used in the approximation is reduced drastically in comparison with the FEM but still retains the high quality of approximations. As can be seen from Figure 1.4, the scaled boundary finite element solution converges rapidly to the reference finite element solution generated by a very fine mesh with 30000 degrees of freedom. For a discretization with only four elements along the plate boundary, with exactly forty degrees of freedom, the relative error is found less than 0.2% [23].

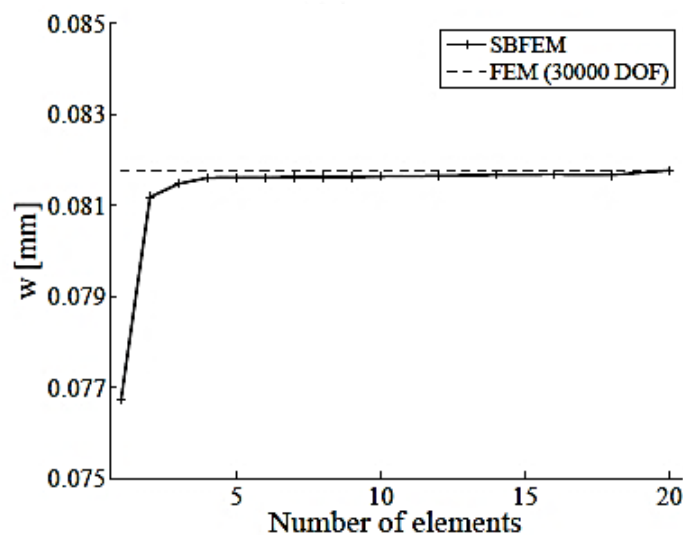


Figure 1.4: Comparison of the maximum displacement obtained from SBFEM with different discretization and that from FEM with 30,000 degrees of freedom (This graph is taken directly from the work of Dieringer and Becker [23]).

Later, Dieringer and Becker [52] applied the SBFEM in the analysis of notches and cracks contained in circular Kirchhoff plates. The scaled boundary finite element method was used to directly compute the order of singularity for a crack of notched circular plate. If the scaling center was selected at the crack tip or notch root, the SBFEM enabled the effective and precise computation of the order of singularity [52]. Furthermore, Man et al. [22] had developed a unified 3D-based technique for plate bending analysis using scaled boundary finite element method. The formulation was based on the three-dimensional governing equation without enforcing the same kinds of kinematics used in plate theories. Only the in-plane dimensions were discretized into a collection of finite elements. Any two-dimensional, displacement-based elements could be employed in the approximation. The solution along the thickness was expressed analytically by using a matrix function. This technique was in line with the three-dimensional theory and applicable to both thick and thin plates without exhibiting

the numerical locking phenomenon. The scaled boundary finite element equations for displacement of plate structures were in the second-order. Also, the Gauss–Lobatto–Legendre quadrature was used to discretize the in-plane dimensions of the plate. The numerical study on four plate bending problems was applied to the patch test with the aim to verify the proposed technique to be able to describe the exact state of a constant bending moment [22]. Obtained results indicated that this technique can pass the patch test and possesses the high accuracy and the fast convergence compared the FEM. For the open-hole square plate subjected to bending loads, the proposed technique was found to accurately capture the stress-concentration was observed and computed results showed the good agreement with the conventional FEM.

Recently, Man et al. [42] developed the high-order plate bending analysis based on the scaled boundary finite element method which significantly improved the prescribed method in terms of efficiency and simplicity for thin to moderately thick plates. The SBFEM in this paper was derived for the plate bending problems through the principle of virtual work. The scaled boundary formulation was derived directly from the three-dimensional, field equations. The in-plane dimensions of the plate were modeled by two-dimensional finite elements. The solution along the thickness was expressed analytically via the Padé expansion by using the SBFEM. Furthermore, the utilization of high-order spectral elements, in turn, allows the accurate treatment of plates with curved boundaries, leads to the high accuracy and convergence rate, and remove the shear locking [42]. Results from their study also indicated the high computational efficiency and accuracy when compared with analytical and finite element solutions. All examples revealed that the proposed technique was able to converge to thin plate solutions when reducing the thickness-to-length ratio without causing any locking phenomenon. Examples with the curved boundaries also underlined the competency of the proposed technique to model curves with minimal number of high-order spectral elements. This technique was able to gain high accuracy and fast convergence as well as to accurately handle plates with relatively complex boundaries.

Table 1.1: Comparisons of features among BEM, FEM, and SBFEM

Features	BEM	FEM	SBFEM
• No fundamental solution required, expanding the scope of application and singular integrals to be evaluated		X	X
• Reduction of spatial dimension by one as only the boundary is discretized with surface finite elements, reducing the data preparation and computational efforts	X		X
• Radiation condition satisfied exactly for unbounded medium	X		X
• Body loads processed without additional domain discretization and thus additional approximation	(X)	X	X
• Symmetric static-stiffness and mass matrices or dynamic-stiffness matrix and symmetric dynamic-stiffness and unit-impulse response matrices for unbounded media.	(X)	X	X
• No approximation other than that of the surface finite elements on the boundary.	X		X
• Straightforward calculation of stress concentrations and intensity factors based on their definition			X
• No discretization of free and fixed boundaries or interfaces between different materials			X
• Analytical solution inside domain permitting efficient calculation of displacements, stresses, and stress-intensity factors			X
• No fictitious eigen-frequencies for unbounded medium		X	X
• Straightforward coupling by standard assemblage of structure discretized with finite elements with unbounded medium		X	X

Note. From “The scaled boundary finite element method” by Wolf, J.P., 2003, *Book of John Wiley & Sons Ltd*, p. 148 [30].

1.2.4 An h -hierarchical adaptive

Numerical methods are computationally efficient when error dispersion is taken into consideration during the refined model construction. Babuška and Rheinboldt [53] introduced adaptive approaches in the finite element analysis. They originally developed the posteriori estimate which indicates how the results can be extended to the nonlinear case without losing their effectiveness. The error indicators are very effective and optimal approach in the adaptation of finite element meshes [53]. Several studies have been reported regarding methods to produce refined finite element and boundary element meshes from a considered distribution of errors or the energy norm of errors (e.g., [54]). In the h -hierarchical approach, the whole mesh is regenerated from the domain-boundary definition and the computed error distribution at each step. The h -hierarchical adaptive procedure tries to automatically refine meshes, the connection between nodes in each element with interpolations in the same order of the shape functions. The entire mesh is the description of the domain boundary which determines the error distribution at each step. This type of adaptivity is the most popular one since its procedure can be easily implemented in the analysis [55]. Rank et al. [56] investigated the computational performance, such as the accuracy and convergence, of h -, p -, and h - p adaptivities. Results from their study indicated that the h - p adaptivity is the best strategy and exhibits the exponential rate of convergence. It was also concluded that the h -adaptive scheme with linear elements is nearly as good as the h - p adaptive scheme and the convergence rate also depends on the geometric configuration [56]. Deeks and Wolf [31] reviewed applications of error estimator used in the adaptive procedures for both finite element and boundary element methods. In the boundary element method, the h -hierarchical adaptivity is often derived by adding h -hierarchical shape functions to the original elements. This procedure has shown the advantage regarding to the build-up of the coefficient matrices in the current iteration and, as a result, it can save both the computational time and storage in the next iteration and the matrices are simply augmented during the iteration process. Nevertheless, this strategy does not work well for the finite element analysis since the banding of the stiffness matrix is demolished and the computational time increases more than necessary to reduce the coefficient matrices [57, 58].

1.2.5 An h -hierarchical adaptive for scaled boundary finite element method

An h -hierarchical adaptive procedure and the stress recovery procedure to obtain the error estimation for the scaled boundary finite element method have been developed by Deeks and Wolf [59]. The h -hierarchical adaptive scheme has been formulated and integrated into the scaled boundary finite element method to further enhance its capability. The adaptive procedure results in significant computational time savings over a uniform mesh if the discretized boundary contains a singular point. If the variation of solutions in the circumferential direction is mild, the procedure can be regarded a convenient method to achieve a specified level of error; however, it does not lead to the significant saving of computational time. The error estimators are assessed based mainly on the energy norm of the stress errors and the computational cost spent with the same accuracy level can be compared. Basically, the computed stresses and displacements are in very close agreement; however, the scaled boundary finite element method can yield results with higher accuracy near points of singularity and for unbounded problems [31, 59]. Yang et al. [60] further developed the method by

deriving a stress recovery technique that was later adopted in the adaptive h -refinement technique applied to structural elasto-dynamics. Results computed by the adaptive SBFEM were in good agreement with those from the literature and those calculated from the adaptive FEM. An adaptive procedure was devised to be capable of automatically identifying an optimal mesh to effectively capture the stress wave propagation in each time step. Then effectiveness and accuracy of the developed method have been concluded [60].

The scaled boundary finite element method has been found to reduce the computational effort considerably. Various investigations have shown that the SBFEM has several positive features such as the accuracy, simplicity, and efficiency for plate bending problem analysis. However, on the basis of extensive literature review, such the adaptive schemes have not been implemented for plate bending problems. For simplicity, the discussion in the present research is limited only to the h -refinement, although any of other refinement methods could be equally applied to the SBFEM with the same ease. The SBFEM supplied by the h -adaptivity can be seen as a means to automatically generating the optimal refinement by maintaining the level of accuracy.

1.3 Research Objectives

The key objectives of the proposed research are to (i) develop the h -hierarchical SBFEM for solving plate bending problems and (ii) investigate the computational performance of developed technique such as the accuracy and convergence of numerical solutions.

1.4 Scope of Work

The proposed study is to be carried out within following context: (i) plate is made of a homogeneous, isotropic, and linearly elastic material; (ii) plate is assumed initially flat and its behavior is completely governed by a Kirchhoff's plate bending with no corner along its entire boundary; (iii) plate is loaded by arbitrarily distributed transverse forces; and (iv) both infinite and finite plates are considered.

1.5 Research Methodology

The present investigation mainly concerns the development of a numerical technique, based on the scaled boundary finite element technique, for solving plate bending problems. The computational performance of the implemented technique is fully explored to demonstrate its accuracy and convergence. In order to accomplish the key objectives indicated above, the following methodology and research procedure are proposed.

- (1) A classical theory of plate bending (i.e., Kirchhoff's plate theory) is utilized to derive the governing differential equations of plates subjected to transverse loading.
- (2) A conventional weighted residual technique together with the integration by parts via Green-Gauss divergence theorem is adopted to construct the weak-form equation.
- (3) A scaled boundary coordinate transformation is introduced to describe the geometry of the plate and, in addition, all differential operators involved in the

formulation are transformed into those concerning the scaled boundary coordinates.

- (4) The geometry of the plate and the corresponding differential operators are approximated via the discretization of the defining curve along with the description of the scaled boundary coordinate transformation.
- (5) The weight function and the deflection are approximated in terms of unknown nodal functions defined in the scaling coordinate direction by using standard element-based basis functions defined in the boundary coordinate direction.
- (6) The scaled boundary finite element equation is established by applying the scaled boundary finite element approximation along with the integration by parts to the weak-form equation. For this particular step, the weak-form equation is properly converted into a system of linear, nonhomogeneous, fourth-order, ordinary differential equations, and a set of boundary conditions.
- (7) A standard technique in the theory of differential equations is utilized to determine a homogeneous solution of the obtained system of linear differential equations. The resulting linear eigenvalue problem is then solved numerically using a selected efficient Eigen search algorithm.
- (8) A particular solution of the obtained system of linear differential equations associated with applied transverse loads and prescribed conditions on the side faces is obtained systematically using the method of undermined coefficients.
- (9) The general solution of a particular boundary value problem is obtained directly by enforcing prescribed conditions on the boundary of the plate.
- (10) All field quantities of interest such as the deflection, force, and moment resultants can be computed using the interpolant involving the nodal basis functions in the boundary coordinate direction and the solved unknown nodal functions in the scaling coordinate direction.
- (11) An h -adaptive scheme together with the moment recovery technique for computing the error estimator is implemented into the developed SBFEM.
- (12) The implemented algorithm is verified with available benchmark solutions for certain cases and its computational performance is then fully investigated for various scenarios.

1.6 Anticipated Outcome and Contribution

This research should offer an alternative, efficient, and accurate numerical technique that is capable of performing the analysis of plate bending problems with h -hierarchical adaptivity. The integration of the h -adaptivity should enhance the capability of the proposed technique to generate results with the optimal mesh within the specified level of accuracy. The proposed technique can be considered as a semi-analytical approach that only requires the discretization along the boundary direction. This apparently renders the significant reduction of the number of degrees of freedom in the approximation and also reduces efforts associated with the pre-processing step such as the mesh generation and mesh adaptation. One obvious application of this computational tool with such integrated features is the use in the modeling/analysis of

flat slab and local analysis of thin components of structural members such as web and flange under the conditions of in-plane and out-of-plane loading.



CHAPTER 2

PROBLEM FORMULATION

In this chapter, a clear problem description is first presented and then the integration of three basic equations from the well-known Kirchhoff's plate theory (i.e., kinematics, constitutive relations, and equilibrium equations) to form a complete set of linear differential equations governing the plate bending problems is addressed. Finally, a weak-form statement is derived using a standard weighted residual technique.

2.1 Problem Description

The present study focuses on a thin plate of uniform thickness h with its in-plane geometry fully described by a two-dimensional region Ω . For convenience in further reference and presentation of relevant results, a reference Cartesian coordinate system $\{x_1, x_2, x_3\}$ is introduced such that the x_3 -axis is perpendicular to the plate and directs downward whereas Ω is contained in the $x_1 - x_2$ plane. The boundary of the plate, denoted by Γ , is assumed to be piecewise smooth and the outward unit normal vector at any smooth point is denoted by $\mathbf{n} = \{n_1 \ n_2\}^T$. Further restrictions on the geometry of the plate will be clearly addressed further below once the scaled boundary coordinate transformation is introduced. For the present investigation, the plate is made of a homogeneous, isotropic, and linearly elastic material with the prescribed Young's modulus E and Poisson's ratio ν . The plate is loaded by a sufficiently smooth distributed transverse force $p(\mathbf{x})$, $\mathbf{x} \in \Omega$, as illustrated in Figure 2.1. The boundary of the plate Γ can be decomposed into Γ_n on which the natural boundary conditions (i.e., shear and moment resultants) are fully prescribed, Γ_e on which the essential boundary conditions (i.e., deflection and rotation) are fully prescribed, and Γ_m on which the mixed boundary conditions are fully prescribed.

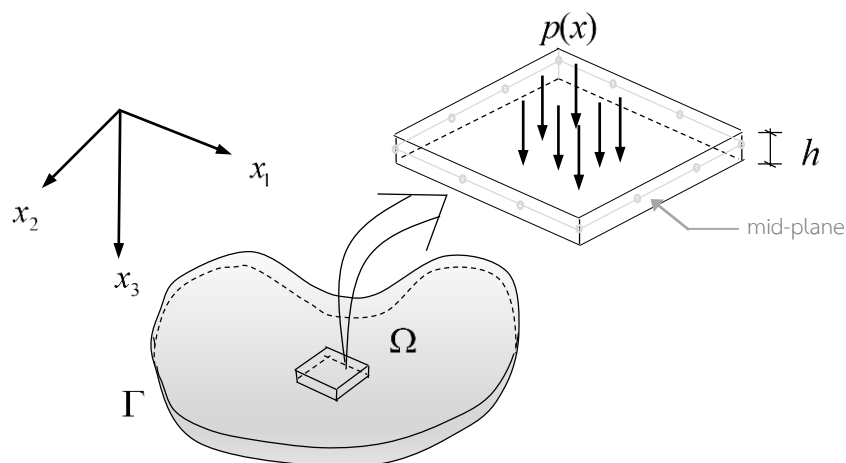


Figure 2.1: Schematic of thin plate subjected to transverse and in-plane loadings

The statement of the problem is to find the solution of the vertical deflection, the rotation, and the corresponding internal resultants such as the shear forces, the bending moments, and the twisting moments due to the action of the applied loads and prescribed boundary conditions.

2.2 Basic Equations

Basic field equations governing responses of the plate including the kinematics, the moment-curvature relationship, and equilibrium equations are obtained from the well-known Kirchhoff's plate theory. The key assumptions and the detailed derivation of all equations are standard and can be found from existing literatures (e.g., [61, 62]). The rotation vector, denoted by $\boldsymbol{\theta} = \{\theta_1 \ \theta_2\}^T$ where θ_1 and θ_2 denote the rotations about the x_1 and x_2 -axes, respectively, the curvature-twist vector, denoted by $\boldsymbol{\kappa} = \{\kappa_{11} \ \kappa_{22} \ \kappa_{12}\}^T$ where κ_{11} , κ_{22} and κ_{12} are the curvature about the x_1 -axis, the curvature about the x_2 -axes and the twisting curvature, respectively, and the vertical deflection, denoted by w , at any point of the plate are linearly related by following linearized kinematics:

$$\boldsymbol{\theta} = \nabla w \quad (2.1)$$

$$\boldsymbol{\kappa} = -\mathbf{L}(\nabla w) \quad (2.2)$$

where ∇ and \mathbf{L} are linear differential operators defined by

$$\nabla = \left\{ \begin{array}{c} \partial/\partial x_1 \\ \partial/\partial x_2 \end{array} \right\} \quad (2.3)$$

$$\mathbf{L} = \begin{bmatrix} \partial/\partial x_1 & 0 \\ 0 & \partial/\partial x_2 \\ \partial/\partial x_2 & \partial/\partial x_1 \end{bmatrix} \quad (2.4)$$

The in-plane moment vector, denoted by $\mathbf{M} = \{M_{11} \ M_{22} \ M_{12}\}^T$ where M_{11} and M_{22} represent the bending moments per unit length about the x_2 -axis and x_1 -axes, respectively, whereas M_{12} denotes the twisting moment per unit length, can be linearly related to the curvature-twist vector $\boldsymbol{\kappa}$ by

$$\mathbf{M} = \mathbf{E}\boldsymbol{\kappa} \quad (2.5)$$

where the matrix \mathbf{E} depends primarily on Young's modulus, Poisson's ratio, and the thickness of the plate given explicitly by

$$\mathbf{E} = \frac{Eh^3}{12(1-\nu^2)} \begin{bmatrix} 1 & \nu & 0 \\ \nu & 1 & 0 \\ 0 & 0 & (1-\nu)/2 \end{bmatrix} \quad (2.6)$$

By enforcing equilibrium of the plate in its deformed configuration together with the infinitesimal deformation assumption, it leads to the following equilibrium equations

$$\nabla^T \mathbf{N} = \mathbf{0} \quad (2.7)$$

$$-\nabla^T \mathbf{Q} = p \quad (2.8)$$

$$\mathbf{L}^T \mathbf{M} = \mathbf{Q} \quad (2.9)$$

where \mathbf{I} is an identity matrix and the shear force vector \mathbf{Q} is defined by

$$\mathbf{Q} = \begin{Bmatrix} Q_1 \\ Q_2 \end{Bmatrix} \quad (2.10)$$

The vertical force per unit length on the boundary of the plate, denoted by V_Γ , can be related to the shear force vector \mathbf{Q} generated by

$$V_\Gamma = \mathbf{Q}^T \mathbf{n} \quad (2.11)$$

where $\mathbf{n}^T = \{n_1 \ n_2\}$ denotes the outward unit normal vector to the boundary of the plate and V_Γ is positive if it directs along the x_3 -coordinate direction. Similarly, the in-plane moment vector on the boundary of the plate, denoted by $\mathbf{M}_\Gamma = \{M_1^\Gamma \ M_2^\Gamma\}^T$, can also be related to the moment components \mathbf{M} by

$$\mathbf{M}_\Gamma = -\bar{\mathbf{n}} \mathbf{M} \quad (2.12)$$

where $\bar{\mathbf{n}}$ is matrix containing components of the outward unit normal vector \mathbf{n} given by

$$\bar{\mathbf{n}} = \begin{bmatrix} n_1 & 0 & n_2 \\ 0 & n_2 & n_1 \end{bmatrix} \quad (2.13)$$

By combining equations (2.2), (2.5), and (2.7)-(2.9), it leads to a non-homogeneous, linear, fourth-order, partial differential equation governing the vertical deflection of the plate w :

$$(\mathbf{L}\nabla)^T \mathbf{E}(\mathbf{L}\nabla w) = p \quad (2.14)$$

Now, the problem statement simply reduces to find the vertical deflection $w = w(\mathbf{x})$ that satisfies (2.14) $\forall \mathbf{x} \in \text{int } \Omega$ and the boundary conditions along $\Gamma = \Gamma_n \cup \Gamma_e \cup \Gamma_m$.

2.3 Weak Formulation

The weak statement of the linear partial differential equation (2.14), which is essential for the development of the scaled boundary finite element method presented in the next

chapter, can be accomplished by applying the standard weighted residual technique together with the integration by parts via Green-Gauss divergence theorem. By multiplying the equilibrium equation (2.8) by an arbitrary, sufficiently smooth weight function $v = v(x_1, x_2)$ and then integrating the result over the entire domain, it yields

$$-\int_{\Omega} v \nabla^T \mathbf{Q} \nabla w dA = \int_{\Omega} v p dA \quad (2.15)$$

By performing the integration by parts of the first integral of (2.15) using Green-Gauss divergence theorem and then applying the relation (2.11) to treat the boundary term, it gives rise to

$$\int_{\Omega} (\nabla v)^T \mathbf{Q} dA = \int_{\Omega} v p dA + \int_{\Gamma} v V_{\Gamma} dl \quad (2.16)$$

By applying the relation (2.9) to the second integral of (2.16), then performing the integration by parts via Green-Gauss divergence theorem, and finally employing the condition (2.12), it results in

$$-\int_{\Omega} (\mathbf{L} \nabla v)^T \mathbf{M} dA = \int_{\Omega} v p dA + \int_{\Gamma} v V_{\Gamma} dl + \int_{\Gamma} (\nabla v)^T \mathbf{M}_{\Gamma} dl \quad (2.17)$$

Finally, by substituting the moment vector \mathbf{M} in terms of the vertical deflection w via the moment-curvature relationship (2.5) and the linearized kinematics (2.2), the weak-form equation becomes

$$\int_{\Omega} (\mathbf{L} \nabla v)^T \mathbf{E} (\mathbf{L} \nabla w) dA = \int_{\Omega} v p dA + \int_{\Gamma} v V_{\Gamma} dl + \int_{\Gamma} (\nabla v)^T \mathbf{M}_{\Gamma} dl \quad (2.18)$$

It should be evident from the derivation that there is no restriction placed on the choice of the weight function v except that it must be sufficiently smooth rendering all involved integrals exist in an ordinary sense. To ensure the integrability of all terms contained in the weak-form equation (2.18), the weight function must satisfy the condition

$$\int_{\Omega} (\mathbf{L} \nabla v)^T (\mathbf{L} \nabla v) dA + \int_{\Omega} (\nabla v)^T \nabla v dA + \int_{\Omega} v^2 dA < \infty \quad (2.19)$$

By defining \mathbf{V} as a space of all functions satisfying the condition (2.19), the problem statement can be changed to find the vertical displacement $w = w(\mathbf{x})$ such that the weak-form equation (2.18) is satisfied $\forall v \in \mathbf{V}$ and the boundary conditions along $\Gamma = \Gamma_n \cup \Gamma_e \cup \Gamma_m$ are satisfied.

CHAPTER 3

SCALED BOUNDARY FINITE ELEMENT FORMULATION

This chapter clearly presents the scaled boundary finite element formulation for general plate bending problems. The chapter begins with the introduction of the scaled boundary coordinate transformation and the description of two-dimensional regions in terms of scaled boundary coordinates. Next, the discretization of the plate geometry, the solution, and the weight function based on the scaled boundary finite element approximation are presented. Finally, such approximations are utilized together with the integration by parts via Green-Gauss divergence theorem to deduce the boundary finite element equation

3.1 Scaled Boundary Coordinate Transformation

Let $\mathbf{x}_0 = (x_{10}, x_{20})$ be a point in \mathbb{R}^2 and C be a simple, piecewise smooth curve in \mathbb{R}^2 such that it does not contain the point \mathbf{x}_0 . The curve C is parameterized by a vector valued function $\mathbf{r} : s \in [a, b] \rightarrow (x_{10} + \hat{x}_1(s), x_{20} + \hat{x}_2(s))$ as illustrated in Figure 3.1 and \mathbf{r} is a given one-to-one function on an open interval (a, b) . Let $\theta(s)$ be a swept angle of any point $\mathbf{r}(s)$ on the curve C measured in a counter clockwise direction from a line connecting a point \mathbf{x}_0 and a point $\mathbf{r}(a)$ to a line connecting a point \mathbf{x}_0 and a point $\mathbf{r}(s)$. In the present study, the curve C can be either closed (i.e., $\mathbf{r}(a) = \mathbf{r}(b)$) or opened (i.e., $\mathbf{r}(a) \neq \mathbf{r}(b)$) and is limited to those satisfying the following conditions: (i) $\theta(b) \leq 2\pi$ and (ii) $\theta(s)$ is a monotonically increasing function of s (i.e., $d\theta/ds > 0 \forall s \in (a, b)$). Later, the point \mathbf{x}_0 is known as the scaling center and the curve C is termed the defining curve.

Let us, now, introduce the following two-dimensional coordinate transformation relating the Cartesian coordinates $\{x_1, x_2\}$ and the so-called scaled boundary coordinates $\{\xi, s\}$ such that

$$x_\alpha = x_{\alpha 0} + \xi \hat{x}_\alpha(s) \quad (3.1)$$

where $\alpha \in \{1, 2\}$ and $\xi \geq 0$. This particular coordinate transformation simply scales the defining curve C in the radial direction with respect to the scaling center \mathbf{x}_0 using the coordinate ξ , which is commonly termed the *scaling coordinate*. Any point along a scaled curve S associated with $\xi = \xi_0$ can be completely described by the coordinate s which is known as the *boundary coordinate*. It can also be pointed out that a straight line $\xi = 0, a \leq s \leq b$ and a straight line $\xi = 1, a \leq s \leq b$ in the $\xi - s$ plane are mapped to the scaling center \mathbf{x}_0 and the defining curve C in the $x_1 - x_2$ plane, respectively. In addition, any straight line $s = s_0, \xi \geq 0$ in the $\xi - s$ plane is mapped to a radial line $L(s = s_0)$ passing through the scaling center and the defining curve C .

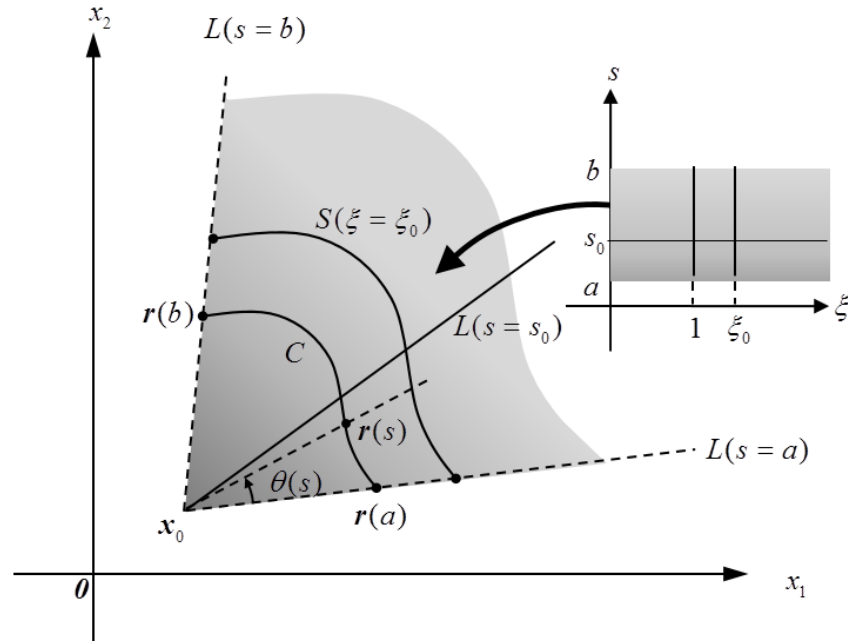


Figure 3.1: Schematic of scaling center \mathbf{x}_0 and defining curve C used in the scaled boundary coordinate transformation

It is apparent from the coordinate transformation (3.1) that partial derivatives with respect to the scaled boundary coordinates $\{\xi, s\}$ can be related to those with respect to the Cartesian coordinates $\{x_1, x_2\}$ by

$$\begin{Bmatrix} \frac{\partial}{\partial \xi} \\ \frac{1}{\xi} \frac{\partial}{\partial s} \end{Bmatrix} = \mathbf{J} \begin{Bmatrix} \frac{\partial}{\partial x_1} \\ \frac{\partial}{\partial x_2} \end{Bmatrix} \quad (3.2)$$

where \mathbf{J} is the Jacobian matrix of transformation given by

$$\mathbf{J} = \begin{bmatrix} \frac{\partial x_1}{\partial \xi} & \frac{\partial x_2}{\partial \xi} \\ \frac{1}{\xi} \frac{\partial x_1}{\partial s} & \frac{1}{\xi} \frac{\partial x_2}{\partial s} \end{bmatrix} = \begin{bmatrix} \hat{x}_1 & \hat{x}_2 \\ \frac{d\hat{x}_1}{ds} & \frac{d\hat{x}_2}{ds} \end{bmatrix} \quad (3.3)$$

By inverting the relation (3.2), it gives rise to

$$\begin{Bmatrix} \frac{\partial}{\partial x_1} \\ \frac{\partial}{\partial x_2} \end{Bmatrix} = \mathbf{J}^{-1} \begin{Bmatrix} \frac{\partial}{\partial \xi} \\ \frac{1}{\xi} \frac{\partial}{\partial s} \end{Bmatrix} = \frac{1}{J} \begin{bmatrix} \frac{d\hat{x}_2}{ds} & -\hat{x}_2 \\ -\frac{d\hat{x}_1}{ds} & \hat{x}_1 \end{bmatrix} \begin{Bmatrix} \frac{\partial}{\partial \xi} \\ \frac{1}{\xi} \frac{\partial}{\partial s} \end{Bmatrix} \quad (3.4)$$

where $J = \det \mathbf{J} = \hat{x}_1 d\hat{x}_2/ds - \hat{x}_2 d\hat{x}_1/ds$. Based on the transformation (3.1), it can also be verified that an infinitesimal element $d\xi$ along any straight line with a constant s in the $\xi - s$ plane is mapped to an infinitesimal element dl in the $x_1 - x_2$ plane such that

$$dl = \sqrt{\hat{x}_1^2 + \hat{x}_2^2} d\xi = J^\xi(s) d\xi, \quad J^\xi(s) = \sqrt{\hat{x}_1^2 + \hat{x}_2^2} \quad (3.5)$$

Similarly, an infinitesimal element ds along any straight line with the constant ξ in the $\xi - s$ plane is mapped to an infinitesimal element dl in the $x_1 - x_2$ plane such that

$$dl = \sqrt{(d\hat{x}_1/ds)^2 + (d\hat{x}_2/ds)^2} \xi ds = J^s(s) \xi ds, \quad J^s(s) = \sqrt{(d\hat{x}_1/ds)^2 + (d\hat{x}_2/ds)^2} \quad (3.6)$$

In addition, the an infinitesimal rectangular area $d\xi ds$ in the $\xi - s$ plane is mapped to an infinitesimal area dA in the $x_1 - x_2$ plane such that

$$dA = J \xi d\xi ds \quad (3.7)$$

Now, by applying the relation (3.4), the linear differential operators ∇ and \mathbf{L} defined in the $x_1 - x_2$ plane by (2.3) and (2.4), respectively, can be expressed in terms of derivative with respect to the scaled boundary coordinates by

$$\mathbf{L} = \hat{\mathbf{b}}_1(s) \frac{\partial}{\partial \xi} + \frac{1}{\xi} \hat{\mathbf{b}}_2(s) \frac{\partial}{\partial s} \quad (3.8)$$

$$\nabla = \hat{\mathbf{b}}_3(s) \frac{\partial}{\partial \xi} + \frac{1}{\xi} \hat{\mathbf{b}}_4(s) \frac{\partial}{\partial s} \quad (3.9)$$

where the matrices $\hat{\mathbf{b}}_1$, $\hat{\mathbf{b}}_2$, $\hat{\mathbf{b}}_3$ and $\hat{\mathbf{b}}_4$ depends only on the boundary coordinate and are given explicitly by

$$\hat{\mathbf{b}}_1(s) = \frac{1}{J} \begin{bmatrix} d\hat{x}_2/ds & 0 \\ 0 & -d\hat{x}_1/ds \\ -d\hat{x}_1/ds & d\hat{x}_2/ds \end{bmatrix}, \quad \hat{\mathbf{b}}_2(s) = \frac{1}{J} \begin{bmatrix} -\hat{x}_2 & 0 \\ 0 & \hat{x}_1 \\ \hat{x}_1 & -\hat{x}_2 \end{bmatrix} \quad (3.10)$$

$$\hat{\mathbf{b}}_3(s) = \frac{1}{J} \begin{bmatrix} d\hat{x}_2/ds \\ -d\hat{x}_1/ds \end{bmatrix}, \quad \hat{\mathbf{b}}_4(s) = \frac{1}{J} \begin{bmatrix} -\hat{x}_2 \\ \hat{x}_1 \end{bmatrix} \quad (3.11)$$

By applying the relations (3.8) and (3.9), the product operator $\mathbf{L}\nabla$ can also be expressed in terms of the scaled boundary coordinates by

$$\mathbf{L}\nabla = \hat{\mathbf{b}}_5 \frac{1}{\xi} \frac{\partial}{\partial \xi} + \hat{\mathbf{b}}_6 \frac{1}{\xi^2} \frac{\partial}{\partial s} + \hat{\mathbf{b}}_7 \frac{\partial^2}{\partial \xi^2} + \hat{\mathbf{b}}_8 \frac{1}{\xi^2} \frac{\partial^2}{\partial s^2} + \hat{\mathbf{b}}_9 \frac{1}{\xi} \frac{\partial^2}{\partial \xi \partial s} \quad (3.12)$$

where the matrices $\hat{\mathbf{b}}_5$, $\hat{\mathbf{b}}_6$, $\hat{\mathbf{b}}_7$ and $\hat{\mathbf{b}}_8$ are defined in terms of the matrices $\hat{\mathbf{b}}_1$, $\hat{\mathbf{b}}_2$, $\hat{\mathbf{b}}_3$ and $\hat{\mathbf{b}}_4$ by

$$\hat{\mathbf{b}}_5 = \hat{\mathbf{b}}_2 \frac{d\hat{\mathbf{b}}_3}{ds}, \hat{\mathbf{b}}_6 = \hat{\mathbf{b}}_2 \frac{d\hat{\mathbf{b}}_4}{ds} - \hat{\mathbf{b}}_1 \hat{\mathbf{b}}_4, \hat{\mathbf{b}}_7 = \hat{\mathbf{b}}_1 \hat{\mathbf{b}}_3, \hat{\mathbf{b}}_8 = \hat{\mathbf{b}}_2 \hat{\mathbf{b}}_4, \hat{\mathbf{b}}_9 = \hat{\mathbf{b}}_1 \hat{\mathbf{b}}_4 + \hat{\mathbf{b}}_2 \hat{\mathbf{b}}_3 \quad (3.13)$$

It should be noted that if \hat{x}_1 and \hat{x}_2 are linear functions of s , the matrix $\hat{\mathbf{b}}_5$ identically vanishes. It is ready, now, to pose the restriction on the geometry of the plate. In the present study, the in-plane geometry Ω must be completely described by a rectangular region $[\xi_1, \xi_2] \times [s_1, s_2]$ in the $\xi-s$ plane via the scaled boundary coordinate transformation (3.1). The scaling center \mathbf{x}_0 and the defining curve C must exist. Based on the description of Ω in the scaled boundary coordinate system, the geometry is said to be *closed* if the defining curve is closed and *opened* if the defining curve is opened. For the opened geometry, portions of Γ associated with $s = s_1$ and $s = s_2$ are termed the *side faces*. The geometry Ω is said to be unbounded if $\xi_2 = \infty$; otherwise, it is bounded. The region contains the scaling center \mathbf{x}_0 if $\xi_1 = 0$.

3.2 Scaled Boundary Finite Element Approximation

In this section, the discretization of the geometry Ω , the vertical deflection w , and the weight function v based on the scaled boundary finite element approximation is introduced.

3.2.1 Approximation of Geometry

Since the geometry Ω is completely described via the transformation (3.1) once the scaling center and the defining curve are selected, its discretization can directly be achieved by approximating the geometry of the defining curve. The defining curve is first discretized into n elements and m nodes with the coordinates $\mathbf{x}_{(i)} = \mathbf{x}_0 + \hat{\mathbf{x}}_{(i)}$, $i = 1, 2, \dots, m$ where $\hat{\mathbf{x}}_{(i)}$ can be viewed as the coordinates of the i^{th} node relative to the scaling center. The coordinates of any point on the defining curve $\mathbf{x} = \mathbf{x}_0 + \hat{\mathbf{x}}(s)$ can be approximated by

$$\mathbf{x}_\alpha^h(s) = x_{\alpha 0} + \hat{x}_\alpha^h(s) = x_{\alpha 0} + \sum_{i=1}^m \phi_{(i)}(s) \hat{x}_{\alpha(i)} = x_{\alpha 0} + N^G \mathbf{X}_\alpha \quad (3.14)$$

where the superscript “ h ” is used to indicate the approximation, $\phi_{(i)} = \phi_{(i)}(s)$ is the nodal basis function defined in terms of the boundary coordinate, $N^G = \{\phi_{(1)} \quad \phi_{(2)} \quad \dots \quad \phi_{(m)}\}$

is a vector containing the nodal basis functions used in the geometry approximation, and $\mathbf{X}_\alpha = \{\hat{x}_{\alpha(1)} \quad \hat{x}_{\alpha(2)} \quad \cdots \quad \hat{x}_{\alpha(m)}\}^T$ is a vector containing the relative coordinates of all nodes. The discretization of the geometry Ω can now be achieved by using the transformation (3.1) along with the chosen scaling center and the discretized defining curve, and the discretized geometry is denoted by Ω^h . With the approximation (3.14), the derivatives $d\hat{x}_\alpha/ds$ can be approximated by

$$\frac{d\hat{x}_\alpha^h}{ds} = \mathbf{B}^G \mathbf{X}_\alpha \quad (3.15)$$

where $\mathbf{B}^G = d\mathbf{N}^G/ds = \{d\phi_{(1)}/ds \quad d\phi_{(2)}/ds \quad \cdots \quad d\phi_{(m)}/ds\}^T$. Then, the parameter J and the matrices $\hat{\mathbf{b}}_1$, $\hat{\mathbf{b}}_2$, $\hat{\mathbf{b}}_3$, and $\hat{\mathbf{b}}_4$ can be approximated by

$$J^h = \mathbf{N}^G \mathbf{X}_1 \mathbf{B}^G \mathbf{X}_2 - \mathbf{N}^G \mathbf{X}_2 \mathbf{B}^G \mathbf{X}_1 \quad (3.16)$$

$$\hat{\mathbf{b}}_1^h = \frac{1}{J^h} \begin{bmatrix} \mathbf{B}^G \mathbf{X}_2 & 0 \\ 0 & -\mathbf{B}^G \mathbf{X}_1 \\ -\mathbf{B}^G \mathbf{X}_1 & \mathbf{B}^G \mathbf{X}_2 \end{bmatrix} \quad (3.17)$$

$$\hat{\mathbf{b}}_2^h = \frac{1}{J^h} \begin{bmatrix} -\mathbf{N}^G \mathbf{X}_2 & 0 \\ 0 & \mathbf{N}^G \mathbf{X}_1 \\ \mathbf{N}^G \mathbf{X}_1 & -\mathbf{N}^G \mathbf{X}_2 \end{bmatrix} \quad (3.18)$$

$$\hat{\mathbf{b}}_3^h = \frac{1}{J^h} \begin{bmatrix} \mathbf{B}^G \mathbf{X}_2 \\ -\mathbf{B}^G \mathbf{X}_1 \end{bmatrix} \quad (3.19)$$

$$\hat{\mathbf{b}}_4^h = \frac{1}{J^h} \begin{bmatrix} -\mathbf{N}^G \mathbf{X}_2 \\ \mathbf{N}^G \mathbf{X}_1 \end{bmatrix} \quad (3.20)$$

The approximation of the matrices $\hat{\mathbf{b}}_5$, $\hat{\mathbf{b}}_6$, $\hat{\mathbf{b}}_7$, and $\hat{\mathbf{b}}_8$ can be obtained using (3.13) (3.13) and (3.16)-(3.20). Finally, the approximate linear differential operator \mathbf{L} , ∇ and $\mathbf{L}\nabla$ are given by

$$\mathbf{L}^h = \hat{\mathbf{b}}_1^h \frac{\partial}{\partial \xi} + \frac{1}{\xi} \hat{\mathbf{b}}_2^h \frac{\partial}{\partial s} \quad (3.21)$$

$$\nabla^h = \hat{\mathbf{b}}_3^h \frac{\partial}{\partial \xi} + \frac{1}{\xi} \hat{\mathbf{b}}_4^h \frac{\partial}{\partial s} \quad (3.22)$$

$$\mathbf{L}^h \nabla^h = \hat{\mathbf{b}}_5^h \frac{1}{\xi} \frac{\partial}{\partial \xi} + \hat{\mathbf{b}}_6^h \frac{1}{\xi^2} \frac{\partial}{\partial s} + \hat{\mathbf{b}}_7^h \frac{\partial^2}{\partial \xi^2} + \hat{\mathbf{b}}_8^h \frac{1}{\xi^2} \frac{\partial^2}{\partial s^2} + \hat{\mathbf{b}}_9^h \frac{1}{\xi} \frac{\partial^2}{\partial \xi \partial s} \quad (3.23)$$

3.2.2 Approximation of Solution and Weight Function

By employing the scaled boundary coordinate transformation along with the approximation (3.14), the vertical deflection $w = w(\xi, s)$ can be approximated by

$$w^h = w^h(\xi, s) = \sum_{i=1}^m \varphi_{(i)}(s) w_{(i)}^h(\xi) + \sum_{i=1}^m \psi_{(i)}(s) \frac{\partial w_{(i)}^h}{\partial s}(\xi) = \mathbf{N}^S \mathbf{W}^h \quad (3.24)$$

where $w_{(i)}^h(\xi)$ and $\partial w_{(i)}^h(\xi)/\partial s$ are the vertical deflection and its gradient along the line $s = s_{(i)}$, $\varphi_{(i)}(s)$ and $\psi_{(i)}(s)$ are nodal basis functions defined in terms of the boundary coordinate, $\mathbf{N}^S = \{\varphi_{(1)} \ \psi_{(1)} \ \varphi_{(2)} \ \psi_{(2)} \ \cdots \ \varphi_{(m)} \ \psi_{(m)}\}$ is a vector containing all nodal basis functions, and $\mathbf{W}^h = \{w_{(1)}^h(\xi) \ \partial w_{(1)}^h(\xi)/\partial s \ w_{(2)}^h(\xi) \ \partial w_{(2)}^h(\xi)/\partial s \ \cdots \ w_{(m)}^h(\xi) \ \partial w_{(m)}^h(\xi)/\partial s\}^T$ is a vector containing all functions $w_{(i)}^h(\xi)$ and $\partial w_{(i)}^h(\xi)/\partial s$. Note that the basic functions $\varphi_{(i)}(s)$ and $\psi_{(i)}(s)$ can be constructed locally based on Hermitian polynomials of a cubic order defined on each element (e.g., [63, 64]) and this, therefore, ensures the satisfaction of the C^1 -continuity and integrability requirement.

Now, the in-plane moment vector $\mathbf{M} = -\mathbf{E}(\mathbf{L}\nabla w)$ and the gradient of the deflection ∇w can also be approximated by

$$\begin{aligned} \mathbf{M}^h &= -\mathbf{E}(\mathbf{L}^h \nabla^h w^h) = -\mathbf{E} \left(\hat{\mathbf{b}}_5^h \frac{1}{\xi} \frac{\partial}{\partial \xi} + \hat{\mathbf{b}}_6^h \frac{1}{\xi^2} \frac{\partial}{\partial s} + \hat{\mathbf{b}}_7^h \frac{\partial^2}{\partial \xi^2} + \hat{\mathbf{b}}_8^h \frac{1}{\xi^2} \frac{\partial^2}{\partial s^2} + \hat{\mathbf{b}}_9^h \frac{1}{\xi} \frac{\partial^2}{\partial \xi \partial s} \right) \mathbf{N}^S \mathbf{W}^h \\ &= -\mathbf{E} \left(\frac{1}{\xi^2} \mathbf{B}_{68} \mathbf{W}^h + \frac{1}{\xi} \mathbf{B}_{59} \frac{d\mathbf{W}^h}{d\xi} + \mathbf{B}_7 \frac{d^2 \mathbf{W}^h}{d\xi^2} \right) \end{aligned} \quad (3.25)$$

$$\nabla^h w^h = \left(\hat{\mathbf{b}}_3^h \frac{\partial}{\partial \xi} + \frac{1}{\xi} \hat{\mathbf{b}}_4^h \frac{\partial}{\partial s} \right) \mathbf{N}^S \mathbf{W}^h = \frac{1}{\xi} \mathbf{B}_4 \mathbf{W}^h + \mathbf{B}_3 \frac{d\mathbf{W}^h}{d\xi} \quad (3.26)$$

where the matrices \mathbf{B}_3 , \mathbf{B}_4 , \mathbf{B}_{59} , \mathbf{B}_{68} and \mathbf{B}_7 are given by

$$\mathbf{B}_3 = \hat{\mathbf{b}}_3^h \mathbf{N}^S \quad (3.27)$$

$$\mathbf{B}_4 = \hat{\mathbf{b}}_4^h \frac{d\mathbf{N}^S}{ds} \quad (3.28)$$

$$\mathbf{B}_{59} = \hat{\mathbf{b}}_5^h \mathbf{N}^S + \hat{\mathbf{b}}_9^h \frac{d\mathbf{N}^S}{ds} \quad (3.29)$$

$$\mathbf{B}_{68} = \hat{\mathbf{b}}_6^h \frac{d\mathbf{N}^S}{ds} + \hat{\mathbf{b}}_8^h \frac{d^2 \mathbf{N}^S}{ds^2} \quad (3.30)$$

$$\mathbf{B}_7 = \hat{\mathbf{b}}_7^h \mathbf{N}^S \quad (3.31)$$

Similarly, the weight function v and the corresponding quantities $\mathbf{L}\nabla v$ and ∇v can be discretized using the same basis functions

$$v^h = v^h(\xi, s) = \sum_{i=1}^m \varphi_{(i)}(s) v_{(i)}^h(\xi) + \sum_{i=1}^m \psi_{(i)}(s) \frac{\partial v_{(i)}^h}{\partial s}(\xi) = \mathbf{N}^s \mathbf{V}^h \quad (3.32)$$

$$\begin{aligned} \mathbf{L}^h \nabla^h v^h &= \left(\hat{\mathbf{b}}_5^h \frac{1}{\xi} \frac{\partial}{\partial \xi} + \hat{\mathbf{b}}_6^h \frac{1}{\xi^2} \frac{\partial}{\partial s} + \hat{\mathbf{b}}_7^h \frac{\partial^2}{\partial \xi^2} + \hat{\mathbf{b}}_8^h \frac{1}{\xi^2} \frac{\partial^2}{\partial s^2} + \hat{\mathbf{b}}_9^h \frac{1}{\xi} \frac{\partial^2}{\partial \xi \partial s} \right) \mathbf{N}^s \mathbf{V}^h \\ &= \frac{1}{\xi^2} \mathbf{B}_{68} \mathbf{V}^h + \frac{1}{\xi} \mathbf{B}_{59} \frac{d\mathbf{V}^h}{d\xi} + \mathbf{B}_7 \frac{d^2 \mathbf{V}^h}{d\xi^2} \end{aligned} \quad (3.33)$$

$$\nabla^h v^h = \left(\hat{\mathbf{b}}_3^h \frac{\partial}{\partial \xi} + \frac{1}{\xi} \hat{\mathbf{b}}_4^h \frac{\partial}{\partial s} \right) \mathbf{N}^s \mathbf{V}^h = \frac{1}{\xi} \mathbf{B}_4 \mathbf{V}^h + \mathbf{B}_3 \frac{d\mathbf{V}^h}{d\xi} \quad (3.34)$$

where $v_{(i)}^h(\xi)$ and $\partial v_{(i)}^h(\xi)/\partial s$ are arbitrary function defined along the line $s = s_{(i)}$ and $\mathbf{V}^h = \{v_{(1)}^h(\xi) \quad \partial v_{(1)}^h(\xi)/\partial s \quad v_{(2)}^h(\xi) \quad \partial v_{(2)}^h(\xi)/\partial s \quad \cdots \quad v_{(m)}^h(\xi) \quad \partial v_{(m)}^h(\xi)/\partial s\}^T$ is an arbitrary vector containing all functions $v_{(i)}^h(\xi)$ and $\partial v_{(i)}^h(\xi)/\partial s$.

3.3 Scaled Boundary Finite Element Equations

In this section, a set of scaled boundary finite element equations are formulated for a representative plate with a general geometry Ω shown in Figure 3.2. The boundary of the domain Γ is assumed consisting of four parts resulting from the scaled boundary coordinate transformation (3.1) with the scaling center \mathbf{x}_0 and defining curve C : the inner boundary Γ_1 , the outer boundary Γ_2 , the side-face-1 Γ_1^s and the side-face-2 Γ_2^s . The approximate geometry Ω^h is achieved via the discretization of the defining curve C^h along with the mapping region $[\xi_1, \xi_2] \times [s_1, s_2]$ in the $\xi - s$ plane. More specifically, the approximate inner boundary Γ_1^h , the approximate outer boundary Γ_2^h , the side-face-1 Γ_1^s , and the side-face-2 Γ_2^s are fully described by a curve $\xi = \xi_1, s_1 \leq s \leq s_2$, a curve, a straight line $s = s_1, \xi_1 \leq \xi \leq \xi_2$, and a straight line $s = s_2, \xi_1 \leq \xi \leq \xi_2$, respectively; $\xi = \xi_2, s_1 \leq s \leq s_2$.

By focusing on the representative geometry Ω shown in Figure 3.2 along with the boundary decomposition $\Gamma = \Gamma_1 \cup \Gamma_2 \cup \Gamma_1^s \cup \Gamma_2^s$, the weak-form equation (2.18) becomes

$$\begin{aligned} \int_{\Omega} (\mathbf{L}\nabla v)^T \mathbf{E}(\mathbf{L}\nabla w) dA &= \int_{\Omega} v p dA + \int_{\Gamma_1} v V_{\Gamma} dl + \int_{\Gamma_2} v V_{\Gamma} dl + \int_{\Gamma_1^s} v V_{\Gamma} dl + \int_{\Gamma_2^s} v V_{\Gamma} dl \\ &+ \int_{\Gamma_1} (\nabla v)^T \mathbf{M}_{\Gamma} dl + \int_{\Gamma_2} (\nabla v)^T \mathbf{M}_{\Gamma} dl + \int_{\Gamma_1^s} (\nabla v)^T \mathbf{M}_{\Gamma} dl + \int_{\Gamma_2^s} (\nabla v)^T \mathbf{M}_{\Gamma} dl \end{aligned} \quad (3.35)$$

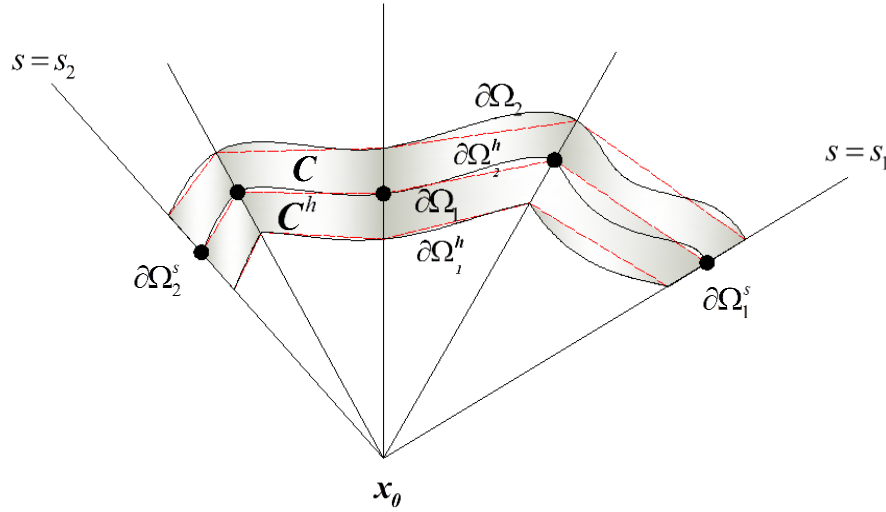


Figure 3.2: Schematic of a representative Ω and its approximation Ω^h . The dashed lines are used to represent the approximation of the defining curve, the inner and outer boundaries.

By applying the transformation eq.(3.1) along with the relations (3.5)-(3.7) to the weak-form equation (3.35), it yields

$$\begin{aligned}
& \int_{s_1}^{s_2} \int_{\xi_1}^{\xi_2} (\mathbf{L}\nabla v)^T \mathbf{E}(\mathbf{L}\nabla w) \xi J d\xi ds = \int_{s_1}^{s_2} \int_{\xi_1}^{\xi_2} v p \xi J d\xi ds + \int_{s_1}^{s_2} v_1 V_{\Gamma_1} J^s(s) \xi_1 ds + \int_{s_1}^{s_2} v_2 V_{\Gamma_2} J^s(s) \xi_2 ds \\
& + \int_{\xi_1}^{\xi_2} v_1^s V_{\Gamma_1^s} J_1^\xi d\xi + \int_{\xi_1}^{\xi_2} v_2^s V_{\Gamma_2^s} J_2^\xi d\xi + \int_{s_1}^{s_2} (\nabla v_1)^T \mathbf{M}_{\Gamma_1} J^s(s) \xi_1 ds + \int_{s_1}^{s_2} (\nabla v_2)^T \mathbf{M}_{\Gamma_2} J^s(s) \xi_2 ds \\
& + \int_{\xi_1}^{\xi_2} (\nabla v_1^s)^T \mathbf{M}_{\Gamma_1^s} J_1^\xi d\xi + \int_{\xi_1}^{\xi_2} (\nabla v_2^s)^T \mathbf{M}_{\Gamma_2^s} J_2^\xi d\xi \quad (3.36)
\end{aligned}$$

where v_1 , v_2 , v_1^s , and v_2^s are the restriction of the weight function v on the boundaries Γ_1 , Γ_2 , Γ_1^s , and Γ_2^s , respectively; V_{Γ_1} , V_{Γ_2} , $V_{\Gamma_1^s}$, and $V_{\Gamma_2^s}$ are the vertical force per unit length on the boundaries Γ_1 , Γ_2 , Γ_1^s , and Γ_2^s , respectively; \mathbf{M}_{Γ_1} , \mathbf{M}_{Γ_2} , $\mathbf{M}_{\Gamma_1^s}$, and $\mathbf{M}_{\Gamma_2^s}$ are the in-plane moments on the boundaries Γ_1 , Γ_2 , Γ_1^s , and Γ_2^s , respectively; $J_1^\xi = J^\xi(s_1)$; and $J_2^\xi = J^\xi(s_2)$. Next, by applying the approximation (3.25) and (3.33) along with the geometry discretization, the first integral on the left-hand side of (3.36), denoted by \mathcal{J}_1 , becomes

$$\mathcal{J}_1 = \int_{s_1}^{s_2} \int_{\xi_1}^{\xi_2} \left(\frac{1}{\xi^2} \mathbf{B}_{68} \mathbf{V}^h + \frac{1}{\xi} \mathbf{B}_{59} \mathbf{V}_{,\xi}^h + \mathbf{B}_7 \mathbf{V}_{,\xi\xi}^h \right)^T \mathbf{E} \left(\frac{1}{\xi^2} \mathbf{B}_{68} \mathbf{W}^h + \frac{1}{\xi} \mathbf{B}_{59} \mathbf{W}_{,\xi}^h + \mathbf{B}_7 \mathbf{W}_{,\xi\xi}^h \right) \xi J d\xi ds \quad (3.37)$$

where $(\cdot)_{,\xi}$ denotes the derivative with respect to the scaling coordinate ξ . By manipulating the involved matrix algebra, the integral \mathcal{J}_1 can be expressed as

$$\begin{aligned} \mathcal{J}_1 &= \int_{\xi_1}^{\xi_2} (\mathbf{V}^h)^T \left(\frac{1}{\xi^3} \mathbf{E}_5 \mathbf{W}^h + \frac{1}{\xi^2} \mathbf{E}_4^T \mathbf{W}_{,\xi}^h + \frac{1}{\xi} \mathbf{E}_2^T \mathbf{W}_{,\xi\xi}^h \right) d\xi \\ &+ \int_{\xi_1}^{\xi_2} (\mathbf{V}_{,\xi}^h)^T \left(\frac{1}{\xi^2} \mathbf{E}_4 \mathbf{W}^h + \frac{1}{\xi} \mathbf{E}_3 \mathbf{W}_{,\xi}^h + \mathbf{E}_1^T \mathbf{W}_{,\xi\xi}^h \right) d\xi \\ &+ \int_{\xi_1}^{\xi_2} (\mathbf{V}_{,\xi\xi}^h)^T \left(\frac{1}{\xi} \mathbf{E}_2 \mathbf{W}^h + \mathbf{E}_1 \mathbf{W}_{,\xi}^h + \xi \mathbf{E}_0 \mathbf{W}_{,\xi\xi}^h \right) d\xi \end{aligned} \quad (3.38)$$

where the matrices \mathbf{E}_0 , \mathbf{E}_1 , \mathbf{E}_2 , \mathbf{E}_3 , \mathbf{E}_4 and \mathbf{E}_5 are defined by

$$\mathbf{E}_0 = \int_{s_1}^{s_2} (\mathbf{B}_7)^T \mathbf{E} \mathbf{B}_7 J ds \quad (3.39)$$

$$\mathbf{E}_1 = \int_{s_1}^{s_2} (\mathbf{B}_7)^T \mathbf{E} \mathbf{B}_{59} J ds \quad (3.40)$$

$$\mathbf{E}_2 = \int_{s_1}^{s_2} (\mathbf{B}_7)^T \mathbf{E} \mathbf{B}_{68} J ds \quad (3.41)$$

$$\mathbf{E}_3 = \int_{s_1}^{s_2} (\mathbf{B}_{59})^T \mathbf{E} \mathbf{B}_{59} J ds \quad (3.42)$$

$$\mathbf{E}_4 = \int_{s_1}^{s_2} (\mathbf{B}_{59})^T \mathbf{E} \mathbf{B}_{68} J ds \quad (3.43)$$

$$\mathbf{E}_5 = \int_{s_1}^{s_2} (\mathbf{B}_{68})^T \mathbf{E} \mathbf{B}_{68} J ds \quad (3.44)$$

It is evident that the matrices \mathbf{E}_0 , \mathbf{E}_3 and \mathbf{E}_5 are symmetric. Now, by integrating the second and third integrals of (3.38) by parts with respect to the scaling coordinate, it leads to

$$\begin{aligned} \mathcal{J}_1 &= \int_{\xi_1}^{\xi_2} (\mathbf{V}^h)^T \left(\frac{1}{\xi^3} (2\mathbf{E}_4 + \mathbf{E}_5) \mathbf{W}^h + \frac{1}{\xi^2} (\mathbf{E}_3 + \mathbf{E}_4^T - \mathbf{E}_4) \mathbf{W}_{,\xi}^h + \frac{1}{\xi} (\mathbf{E}_2^T - \mathbf{E}_3) \mathbf{W}_{,\xi\xi}^h - \mathbf{E}_1^T \mathbf{W}_{,\xi\xi\xi}^h \right) d\xi \\ &- \int_{\xi_1}^{\xi_2} (\mathbf{V}_{,\xi}^h)^T \left(-\frac{1}{\xi^2} \mathbf{E}_2 \mathbf{W}^h + \frac{1}{\xi} \mathbf{E}_2 \mathbf{W}_{,\xi}^h + (\mathbf{E}_0 + \mathbf{E}_1) \mathbf{W}_{,\xi\xi}^h + \xi \mathbf{E}_0 \mathbf{W}_{,\xi\xi\xi}^h \right) d\xi \\ &+ (\mathbf{V}^h)^T \left(\frac{1}{\xi^2} \mathbf{E}_4 \mathbf{W}^h + \frac{1}{\xi} \mathbf{E}_3 \mathbf{W}_{,\xi}^h + \mathbf{E}_1^T \mathbf{W}_{,\xi\xi}^h \right) \Big|_{\xi_1}^{\xi_2} + (\mathbf{V}_{,\xi}^h)^T \left(\frac{1}{\xi} \mathbf{E}_2 \mathbf{W}^h + \mathbf{E}_1 \mathbf{W}_{,\xi}^h + \xi \mathbf{E}_0 \mathbf{W}_{,\xi\xi}^h \right) \Big|_{\xi_1}^{\xi_2} \end{aligned} \quad (3.45)$$

By further performing the integration by parts of the second integral of (3.45), it finally gives rise to

$$\begin{aligned}
\mathcal{J}_1 = & \int_{\xi_1}^{\xi_2} (\mathbf{V}^h)^T \frac{1}{\xi^3} (\boldsymbol{\varepsilon}_0 \mathbf{W}^h + \xi \boldsymbol{\varepsilon}_1 \mathbf{W}_{,\xi}^h + \xi^2 \boldsymbol{\varepsilon}_2 \mathbf{W}_{,\xi\xi}^h + \xi^3 \boldsymbol{\varepsilon}_3 \mathbf{W}_{,\xi\xi\xi}^h + \xi^4 \mathbf{E}_0 \mathbf{W}_{,\xi\xi\xi\xi}^h - \mathcal{F}) d\xi \\
& + (\mathbf{V}^{h2})^T \left\{ \mathcal{G}_0 \mathbf{W}^h + \mathcal{G}_1 \mathbf{W}_{,\xi}^h + \mathcal{G}_2 \mathbf{W}_{,\xi\xi}^h - \xi \mathbf{E}_0 \mathbf{W}_{,\xi\xi\xi}^h - \mathcal{P}_2 \right\}_{\xi=\xi_2} \\
& - (\mathbf{V}^{h1})^T \left\{ \mathcal{G}_0 \mathbf{W}^h + \mathcal{G}_1 \mathbf{W}_{,\xi}^h + \mathcal{G}_2 \mathbf{W}_{,\xi\xi}^h - \xi \mathbf{E}_0 \mathbf{W}_{,\xi\xi\xi}^h + \mathcal{P}_1 \right\}_{\xi=\xi_1} \\
& + (\mathbf{V}_{,\xi}^{h2})^T \left\{ \frac{1}{\xi} \mathbf{E}_2 \mathbf{W}^h + \mathbf{E}_1 \mathbf{W}_{,\xi}^h + \xi \mathbf{E}_0 \mathbf{W}_{,\xi\xi}^h - \mathbf{M}^{22} \right\}_{\xi=\xi_2} \\
& - (\mathbf{V}_{,\xi}^{h1})^T \left\{ \frac{1}{\xi} \mathbf{E}_2 \mathbf{W}^h + \mathbf{E}_1 \mathbf{W}_{,\xi}^h + \xi \mathbf{E}_0 \mathbf{W}_{,\xi\xi}^h + \mathbf{M}^{12} \right\}_{\xi=\xi_1}
\end{aligned} \tag{3.46}$$

where $\mathbf{V}^{h1} = \mathbf{V}^h(\xi = \xi_1)$, $\mathbf{V}^{h2} = \mathbf{V}^h(\xi = \xi_2)$, $\mathbf{V}_{,\xi}^{h1} = \mathbf{V}_{,\xi}^h(\xi = \xi_1)$ and $\mathbf{V}_{,\xi}^{h2} = \mathbf{V}_{,\xi}^h(\xi = \xi_2)$.

Now, the integral associated with the prescribed transverse load p on the right hand side of (3.36), denoted by \mathcal{J}_2 , can be approximated by

$$\mathcal{J}_2 = \int_{s_1}^{s_2} \int_{\xi_1}^{\xi_2} (\mathbf{N}^S \mathbf{V}^h)^T p \xi J d\xi ds = \int_{\xi_1}^{\xi_2} (\mathbf{V}^h)^T \xi \mathbf{F}^p d\xi \tag{3.47}$$

where \mathbf{F}^p is a prescribed matrix defined by

$$\mathbf{F}^p = \int_{s_1}^{s_2} (\mathbf{N}^S)^T p J ds \tag{3.48}$$

Similarly, all the boundary terms associated with the vertical force in the weak-form equation (3.36), denoted by \mathcal{J}_3 , can be approximated by

$$\mathcal{J}_3 = (\mathbf{V}^{h1})^T \mathbf{P}^1 + (\mathbf{V}^{h2})^T \mathbf{P}^2 + \int_{\xi_1}^{\xi_2} (\mathbf{V}^h)^T (\mathbf{F}^{V1} + \mathbf{F}^{V2}) d\xi \tag{3.49}$$

where the matrices \mathbf{P}^1 , \mathbf{P}^2 , \mathbf{F}^{V1} , and \mathbf{F}^{V2} are given by

$$\mathbf{P}^1 = \int_{s_1}^{s_2} (\mathbf{N}^S)^T V_{\Gamma_1} J^s(s) \xi_1 ds \tag{3.50}$$

$$\mathbf{P}^2 = \int_{s_1}^{s_2} (\mathbf{N}^S)^T V_{\Gamma_2} J^s(s) \xi_2 ds \tag{3.51}$$

$$\mathbf{F}^{V1} = \mathbf{F}^{V1}(\xi) = (\mathbf{N}^{S1})^T V_{\Gamma_1} J_1^\xi \tag{3.52}$$

$$\mathbf{F}^{V2} = \mathbf{F}^{V2}(\xi) = (\mathbf{N}^{S2})^T \mathbf{V}_{\Gamma_2^s} J_2^\xi \quad (3.53)$$

and $\mathbf{N}^{S1} = \mathbf{N}^S(s = s_1)$, $\mathbf{N}^{S2} = \mathbf{N}^S(s = s_2)$. By following the same procedure, all the boundary terms associated with the moment in the weak-form equation, denoted by \mathcal{J}_4 , can be approximated by

$$\begin{aligned} \mathcal{J}_4 = & \int_{s_1}^{s_2} \left(\frac{1}{\xi_1} \mathbf{B}_4 \mathbf{V}^{h1} + \mathbf{B}_3 \mathbf{V}_{,\xi}^{h1} \right)^T \mathbf{M}_{\Gamma_1} J^s(s) \xi_1 ds + \int_{s_1}^{s_2} \left(\frac{1}{\xi_2} \mathbf{B}_4 \mathbf{V}^{h2} + \mathbf{B}_3 \mathbf{V}_{,\xi}^{h2} \right)^T \mathbf{M}_{\Gamma_2} J^s(s) \xi_2 ds \\ & + \int_{\xi_1}^{\xi_2} \left(\frac{1}{\xi} \mathbf{B}_4^1 \mathbf{V}^h + \mathbf{B}_3^1 \mathbf{V}_{,\xi}^h \right)^T \mathbf{M}_{\Gamma_1^s} J_1^\xi d\xi + \int_{\xi_1}^{\xi_2} \left(\frac{1}{\xi} \mathbf{B}_4^2 \mathbf{V}^h + \mathbf{B}_3^2 \mathbf{V}_{,\xi}^h \right)^T \mathbf{M}_{\Gamma_2^s} J_2^\xi d\xi \end{aligned} \quad (3.54)$$

where $\mathbf{B}_3^1 = \mathbf{B}_3(s = s_1)$, $\mathbf{B}_3^2 = \mathbf{B}_3(s = s_2)$, $\mathbf{B}_4^1 = \mathbf{B}_4(s = s_1)$, and $\mathbf{B}_4^2 = \mathbf{B}_4(s = s_2)$. By manipulating the matrix operations and performing the integration by parts of terms associated with $\mathbf{V}_{,\xi}^h$, (3.54) reduces to

$$\begin{aligned} \mathcal{J}_4 = & (\mathbf{V}^{h1})^T \mathbf{M}^{11} + (\mathbf{V}_{,\xi}^{h1})^T \mathbf{M}^{12} + (\mathbf{V}^{h2})^T \mathbf{M}^{21} + (\mathbf{V}_{,\xi}^{h2})^T \mathbf{M}^{22} \\ & + \int_{\xi_1}^{\xi_2} (\mathbf{V}^h)^T \left(\mathbf{F}^{M11} + \mathbf{F}^{M21} - \mathbf{F}_{,\xi}^{M12} - \mathbf{F}_{,\xi}^{M22} \right) d\xi \\ & + (\mathbf{V}^{h2})^T \left\{ \mathbf{F}^{M12} + \mathbf{F}^{M22} \right\}_{\xi=\xi_2} - (\mathbf{V}^{h1})^T \left\{ \mathbf{F}^{M12} + \mathbf{F}^{M22} \right\}_{\xi=\xi_1} \end{aligned} \quad (3.55)$$

where all the matrices \mathbf{M}^{11} , \mathbf{M}^{12} , \mathbf{M}^{21} , \mathbf{M}^{22} , \mathbf{F}^{M11} , \mathbf{F}^{M12} , \mathbf{F}^{M21} , and \mathbf{F}^{M22} are defined explicitly by

$$\mathbf{M}^{11} = \int_{s_1}^{s_2} (\mathbf{B}_4)^T \mathbf{M}_{\Gamma_1} J^s(s) ds, \quad \mathbf{M}^{12} = \int_{s_1}^{s_2} (\mathbf{B}_3)^T \mathbf{M}_{\Gamma_1} J^s(s) \xi_1 ds \quad (3.56)$$

$$\mathbf{M}^{21} = \int_{s_1}^{s_2} (\mathbf{B}_4)^T \mathbf{M}_{\Gamma_2} J^s(s) ds, \quad \mathbf{M}^{22} = \int_{s_1}^{s_2} (\mathbf{B}_3)^T \mathbf{M}_{\Gamma_2} J^s(s) \xi_2 ds \quad (3.57)$$

$$\mathbf{F}^{M11} = \mathbf{F}^{M11}(\xi) = \frac{1}{\xi} (\mathbf{B}_4^1)^T \mathbf{M}_{\Gamma_1^s} J_1^\xi, \quad \mathbf{F}^{M12} = \mathbf{F}^{M12}(\xi) = (\mathbf{B}_3^1)^T \mathbf{M}_{\Gamma_1^s} J_1^\xi \quad (3.58)$$

$$\mathbf{F}^{M21} = \mathbf{F}^{M21}(\xi) = \frac{1}{\xi} (\mathbf{B}_4^2)^T \mathbf{M}_{\Gamma_2^s} J_2^\xi, \quad \mathbf{F}^{M22} = \mathbf{F}^{M22}(\xi) = (\mathbf{B}_3^2)^T \mathbf{M}_{\Gamma_2^s} J_2^\xi \quad (3.59)$$

By substituting the approximate integrals \mathcal{J}_1 , \mathcal{J}_2 , \mathcal{J}_3 , and \mathcal{J}_4 into the weak-form equation(3.36), it finally gives

$$\begin{aligned}
& \int_{\xi_1}^{\xi_2} (\mathbf{V}^h)^T \frac{1}{\xi^3} (\boldsymbol{\varepsilon}_0 \mathbf{W}^h + \xi \boldsymbol{\varepsilon}_1 \mathbf{W}_{,\xi}^h + \xi^2 \boldsymbol{\varepsilon}_2 \mathbf{W}_{,\xi\xi}^h + \xi^3 \boldsymbol{\varepsilon}_3 \mathbf{W}_{,\xi\xi\xi}^h + \xi^4 \boldsymbol{\varepsilon}_4 \mathbf{W}_{,\xi\xi\xi\xi}^h - \mathcal{F}) d\xi \\
& + (\mathbf{V}^{h2})^T \left\{ \mathcal{G}_0 \mathbf{W}^h + \mathcal{G}_1 \mathbf{W}_{,\xi}^h + \mathcal{G}_2 \mathbf{W}_{,\xi\xi}^h + \mathcal{G}_3 \mathbf{W}_{,\xi\xi\xi}^h - \mathcal{P}_2 \right\}_{\xi=\xi_2} \\
& - (\mathbf{V}^{h1})^T \left\{ \mathcal{G}_0 \mathbf{W}^h + \mathcal{G}_1 \mathbf{W}_{,\xi}^h + \mathcal{G}_2 \mathbf{W}_{,\xi\xi}^h + \mathcal{G}_3 \mathbf{W}_{,\xi\xi\xi}^h + \mathcal{P}_1 \right\}_{\xi=\xi_1} \\
& + (\mathbf{V}_{,\xi}^{h2})^T \left\{ \frac{1}{\xi} \mathbf{E}_2 \mathbf{W}^h + \mathbf{E}_1 \mathbf{W}_{,\xi}^h + \xi \mathbf{E}_0 \mathbf{W}_{,\xi\xi}^h - \mathbf{M}^{22} \right\}_{\xi=\xi_2} \\
& - (\mathbf{V}_{,\xi}^{h1})^T \left\{ \frac{1}{\xi} \mathbf{E}_2 \mathbf{W}^h + \mathbf{E}_1 \mathbf{W}_{,\xi}^h + \xi \mathbf{E}_0 \mathbf{W}_{,\xi\xi}^h + \mathbf{M}^{12} \right\}_{\xi=\xi_1} = 0 \tag{3.60}
\end{aligned}$$

where the matrices $\mathcal{F}, \boldsymbol{\varepsilon}_0, \boldsymbol{\varepsilon}_1, \boldsymbol{\varepsilon}_2, \boldsymbol{\varepsilon}_3, \boldsymbol{\varepsilon}_4, \mathcal{G}_0, \mathcal{G}_1, \mathcal{G}_2, \mathcal{G}_3, \mathcal{P}_1$ and \mathcal{P}_2 are given by

$$\mathcal{F} = \xi^4 \mathbf{F}^p + \xi^3 (\mathbf{F}^{V1} + \mathbf{F}^{V2} + \mathbf{F}^{M11} + \mathbf{F}^{M21} - \mathbf{F}_{,\xi}^{M12} - \mathbf{F}_{,\xi}^{M22}) \tag{3.61}$$

$$\boldsymbol{\varepsilon}_0 = 2\mathbf{E}_2 + 2\mathbf{E}_4 + \mathbf{E}_5 \tag{3.62}$$

$$\boldsymbol{\varepsilon}_1 = -2\mathbf{E}_2 + \mathbf{E}_3 - \mathbf{E}_4 + \mathbf{E}_4^T \tag{3.63}$$

$$\boldsymbol{\varepsilon}_2 = \mathbf{E}_2^T + \mathbf{E}_2 - \mathbf{E}_3 \tag{3.64}$$

$$\boldsymbol{\varepsilon}_3 = 2\mathbf{E}_0 + \mathbf{E}_1 - \mathbf{E}_1^T \tag{3.65}$$

$$\boldsymbol{\varepsilon}_4 = \mathbf{E}_0 \tag{3.66}$$

$$\mathcal{G}_0 = (\mathbf{E}_2 + \mathbf{E}_4) / \xi^2 \tag{3.67}$$

$$\mathcal{G}_1 = (-\mathbf{E}_2 + \mathbf{E}_3) / \xi \tag{3.68}$$

$$\mathcal{G}_2 = -\mathbf{E}_0 - \mathbf{E}_1 + \mathbf{E}_1^T \tag{3.69}$$

$$\mathcal{G}_3 = -\xi \mathbf{E}_0 \tag{3.70}$$

$$\mathcal{P}_1 = \mathbf{P}^1 + \mathbf{M}^{11} - \mathbf{F}^{M12} - \mathbf{F}^{M22} \tag{3.71}$$

$$\mathcal{P}_2 = \mathbf{P}^2 + \mathbf{M}^{21} + \mathbf{F}^{M12} + \mathbf{F}^{M22} \tag{3.72}$$

Now, by employing the arbitrariness of \mathbf{V}^h and its values and gradient on the boundary, it can be concluded from (3.60) that

$$\boldsymbol{\varepsilon}_0 \mathbf{W}^h + \xi \boldsymbol{\varepsilon}_1 \mathbf{W}_{,\xi}^h + \xi^2 \boldsymbol{\varepsilon}_2 \mathbf{W}_{,\xi\xi}^h + \xi^3 \boldsymbol{\varepsilon}_3 \mathbf{W}_{,\xi\xi\xi}^h + \xi^4 \boldsymbol{\varepsilon}_4 \mathbf{W}_{,\xi\xi\xi\xi}^h = \mathcal{F} \quad \forall \xi \in (\xi_1, \xi_2) \tag{3.73}$$

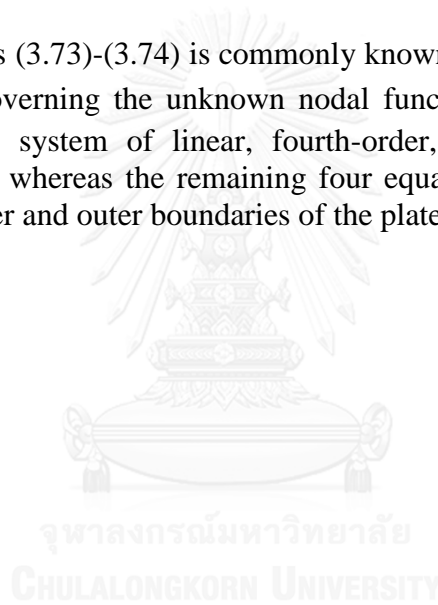
$$\begin{Bmatrix} -\mathbf{q}^h(\xi_1) \\ -\mathbf{m}^h(\xi_1) \\ \mathbf{q}^h(\xi_2) \\ \mathbf{m}^h(\xi_2) \end{Bmatrix} = \begin{Bmatrix} \mathcal{P}_1 \\ \mathbf{M}^{12} \\ \mathcal{P}_2 \\ \mathbf{M}^{22} \end{Bmatrix} \quad (3.74)$$

where the matrices \mathbf{q}^h and \mathbf{m}^h , known as the nodal internal force and moment, are given by

$$\mathbf{q}^h(\xi) = \mathcal{G}_0 \mathbf{W}^h + \mathcal{G}_1 \mathbf{W}_{,\xi}^h + \mathcal{G}_2 \mathbf{W}_{,\xi\xi}^h + \mathcal{G}_3 \mathbf{W}_{,\xi\xi\xi}^h \quad (3.75)$$

$$\mathbf{m}^h(\xi) = \frac{1}{\xi} \mathbf{E}_2 \mathbf{W}^h + \mathbf{E}_1 \mathbf{W}_{,\xi}^h + \xi \mathbf{E}_0 \mathbf{W}_{,\xi\xi}^h \quad (3.76)$$

A system of equations (3.73)-(3.74) is commonly known as the scaled boundary finite element equations governing the unknown nodal functions $\mathbf{W}^h = \mathbf{W}^h(\xi)$. The first equation (3.73) is a system of linear, fourth-order, non-homogeneous, ordinary differential equations whereas the remaining four equations constitute the boundary conditions on the inner and outer boundaries of the plate.



CHAPTER 4

SOLUTION METHODOLOGY

This chapter presents the procedure for obtaining the analytical solution of a linear system, fourth-order, ordinary differential equations, nonhomogeneous(3.73) and the boundary conditions(3.74). A corresponding nonlinear eigenvalue problem is first solved to determine the homogeneous solution. A particular solution of the obtained system of linear differential equations using the method of undetermined coefficient with the distributed transverse loads and the prescribed conditions on the side faces. The general solution is obtained, the boundary conditions on the boundary of the plate are enforced to determine all involved constants. Finally, the post-process for all field quantities of interest such as the vertical deflection, internal shear forces and bending moments are presented.

4.1 Determination of Homogeneous Solution

The homogenous solution of a system of Euler-Cauchy differential equations (3.73), denoted by \mathbf{W}_h^h , is obtained by solving a system of Euler-Cauchy ordinary differential equations

$$\mathcal{E}_0 \mathbf{W}_h^h + \xi \mathcal{E}_1 \mathbf{W}_{h,\xi}^h + \xi^2 \mathcal{E}_2 \mathbf{W}_{h,\xi\xi}^h + \xi^3 \mathcal{E}_3 \mathbf{W}_{h,\xi\xi\xi}^h + \xi^4 \mathcal{E}_4 \mathbf{W}_{h,\xi\xi\xi\xi}^h = 0 \quad (4.1)$$

It is well known that \mathbf{W}_h^h must admit the following form

$$\mathbf{W}_h^h = \sum_{i=1}^N c_i \xi^{\lambda_i} \phi \quad (4.2)$$

where N denotes the number of solution terms, λ_i denotes the i^{th} modal scaling factor for the radial direction, and ϕ represents the i^{th} independent deformation mode. By substituting (4.2) into(4.1), it leads to a fourth-order eigenvalue system governing both λ_i and ϕ :

$$[\lambda_i^4 \mathcal{E}_4 + \lambda_i^3 (\mathcal{E}_3 - 6\mathcal{E}_4) + \lambda_i^2 (\mathcal{E}_2 - 3\mathcal{E}_3 + 11\mathcal{E}_4) + \lambda_i (\mathcal{E}_1 - \mathcal{E}_2 + 2\mathcal{E}_3 - 6\mathcal{E}_4) + \mathcal{E}_4] \phi = 0 \quad (4.3)$$

This eigenvalue problem (4.3) can be solved numerically by a selected efficient Eigen search algorithm (e.g., QZ factorization, polynomial root search, etc.). The homogeneous solution now can be expressed as

$$\mathbf{W}_h^h(\xi) = \Phi^{\phi^+} \Pi^+ \mathbf{C}^+ + \Phi^{\phi^-} \Pi^- \mathbf{C}^- = \mathbf{F}_w(\xi) \mathbf{C} \quad (4.4)$$

where $\mathbf{F}_w(\xi) = \mathbf{\Phi}\mathbf{\Pi}$, $\mathbf{\Phi}$ is a matrix whose i^{th} column containing the eigenvector ϕ_i , $\mathbf{\Pi}$ is a diagonal matrix containing ξ^{λ_i} ; \mathbf{C} is a vector containing unknown constants; $\mathbf{\Phi}^{\phi^+}$ and $\mathbf{\Phi}^{\phi^-}$ are matrices whose columns containing eigenvectors associated with eigenvalues with the positive real part and negative real part, respectively; $\mathbf{\Pi}^+$ and $\mathbf{\Pi}^-$ are diagonal matrices whose the diagonal containing function ξ^{λ_i} for eigenvalues with the positive real part and negative real part, respectively; and \mathbf{C}^+ and \mathbf{C}^- are arbitrary constants. Note that the arbitrary constants \mathbf{C}^+ and \mathbf{C}^- reflect the weightings of the corresponding modal deformation due to the boundary conditions. It is apparent that the diagonal entries of $\mathbf{\Pi}^+$ and $\mathbf{\Pi}^-$ become infinite when $\xi \rightarrow \infty$ and $\xi \rightarrow 0$, respectively. As a result, \mathbf{C}^+ is taken to $\mathbf{0}$ to ensure the boundedness of the solution for unbounded bodies and, similarly, the condition $\mathbf{C}^- = \mathbf{0}$ is enforced for bodies containing the scaling center. Once the homogeneous solution \mathbf{W}_h^h is obtained, by substituting (4.4) into (3.75)-(3.76), the corresponding nodal internal force and bending moment, denoted by $\mathbf{q}_h^h(\xi)$ and $\mathbf{m}_h^h(\xi)$, respectively, are given by

$$\mathbf{q}_h^h(\xi) = \left(\mathcal{G}_0 \mathbf{F}_w(\xi) + \mathcal{G}_1 \mathbf{F}_w(\xi)_{,\xi} + \mathcal{G}_2 \mathbf{F}_w(\xi)_{,\xi\xi} + \mathcal{G}_3 \mathbf{F}_w(\xi)_{,\xi\xi\xi} \right) \mathbf{C} = \mathbf{F}_q(\xi) \mathbf{C} \quad (4.5)$$

$$\mathbf{m}_h^h(\xi) = \left(\frac{1}{\xi} \mathbf{E}_2 \mathbf{F}_w(\xi) + \mathbf{E}_1 \mathbf{F}_w(\xi)_{,\xi} + \xi \mathbf{E}_0 \mathbf{F}_w(\xi)_{,\xi\xi} \right) \mathbf{C} = \mathbf{F}_m(\xi) \mathbf{C} \quad (4.6)$$

4.2 Determination of Particular Solution

A particular solution of the obtained system of linear differential equations (3.73) associated with applied transverse loads and prescribed conditions on the side faces, denoted by $\mathbf{W}_p^h(\xi)$, is obtained systematically using the method of undermined coefficients. In the present study, the transverse load p , the vertical forces on the side-face-1 $V_{\Gamma_1^s}$, the vertical forces on the side-face-2 $V_{\Gamma_2^s}$, the in-plane moment vector on the side-face-1 $\mathbf{M}_{\Gamma_1^s}$, and the in-plane moment vector on the side-face-2 $\mathbf{M}_{\Gamma_2^s}$ of the plate are assumed to admit the form

$$p(\xi, s) = \sum_{\gamma_j \in \mathfrak{R}^*} \xi^{\gamma_j} \bar{p}_j(s) \quad (4.7)$$

$$V_{\Gamma_1^s}(\xi) = \sum_{\beta_j \in \mathfrak{R}^*} \xi^{\beta_j} \bar{V}_{\Gamma_1^s} \quad (4.8)$$

$$V_{\Gamma_2^s}(\xi) = \sum_{\tau_j \in \mathfrak{R}^*} \xi^{\tau_j} \bar{V}_{\Gamma_2^s} \quad (4.9)$$

$$\mathbf{M}_{\Gamma_1^s}(\xi) = \sum_{\omega_j \in \mathfrak{R}^*} \xi^{\omega_j} \bar{\mathbf{M}}_{\Gamma_1^s} \quad (4.10)$$

$$\mathbf{M}_{\Gamma_2^s}(\xi) = \sum_{\kappa_j \in \mathfrak{R}^*} \xi^{\kappa_j} \bar{\mathbf{M}}_{\Gamma_2^s} \quad (4.11)$$

where \mathfrak{R}^* denotes a set of non-negative real numbers, $\bar{p}_j(s)$ are prescribed functions of s and $\bar{V}_{\Gamma_{1j}^s}$, $\bar{V}_{\Gamma_{2j}^s}$, $\bar{\mathbf{M}}_{\Gamma_{1j}^s}$ and $\bar{\mathbf{M}}_{\Gamma_{2j}^s}$ are prescribed constants. Substituting (4.7) into (3.48), (4.8) into (3.52), (4.9) into (3.53), (4.10) into (3.58) and (4.11) into (3.59) yields

$$\mathbf{F}^p = \sum_{\gamma_j \in \mathfrak{R}^*} \xi^{\gamma_j} \bar{\mathbf{F}}_j^p \quad (4.12)$$

$$\mathbf{F}^{V1} = \sum_{\beta_j \in \mathfrak{R}^*} \xi^{\beta_j} \bar{\mathbf{F}}_j^{V1} \quad (4.13)$$

$$\mathbf{F}^{V2} = \sum_{\tau_j \in \mathfrak{R}^*} \xi^{\tau_j} \bar{\mathbf{F}}_j^{V2} \quad (4.14)$$

$$\mathbf{F}^{M11} = \sum_{\omega_j \in \mathfrak{R}^*} \xi^{\omega_j-1} \bar{\mathbf{F}}_j^{M11}, \quad \mathbf{F}_{,\xi}^{M12} = \sum_{\omega_j \in \mathfrak{R}^*} \xi^{\omega_j-1} \omega_j \bar{\mathbf{F}}_{j,\xi}^{M12} \quad (4.15)$$

$$\mathbf{F}^{M21} = \sum_{\kappa_j \in \mathfrak{R}^*} \xi^{\kappa_j-1} \bar{\mathbf{F}}_j^{M21}, \quad \mathbf{F}^{M22} = \sum_{\kappa_j \in \mathfrak{R}^*} \xi^{\kappa_j-1} \kappa_j \bar{\mathbf{F}}_{j,\xi}^{M22} \quad (4.16)$$

where $\bar{\mathbf{F}}_j^p$ is defined, in terms of the prescribed data, by

$$\bar{\mathbf{F}}_j^p = \int_{s_1}^{s_2} (\mathbf{N}^S)^T \bar{p}_j(s) J ds = \left\{ \int_{s_i}^{s_o} \varphi_{(1)}(s) \bar{p}_j(s) J ds \quad \int_{s_i}^{s_o} \psi_{(1)}(s) \bar{p}_j(s) J ds \quad \dots \right. \\ \left. \int_{s_i}^{s_o} \varphi_{(j)}(s) \bar{p}_j(s) J ds \quad \int_{s_i}^{s_o} \psi_{(j)}(s) \bar{p}_j(s) J ds \right\}^T \quad (4.17)$$

and $\bar{\mathbf{F}}_j^{V1}$, $\bar{\mathbf{F}}_j^{V2}$, $\bar{\mathbf{F}}_j^{M11}$, $\bar{\mathbf{F}}_j^{M12}$, $\bar{\mathbf{F}}_j^{M21}$ and $\bar{\mathbf{F}}_j^{M22}$ can be defined as follows. Without loss of generality, the first node (1) and the last node (j) resulting from the discretization of opened bodies are taken as a node on the side-face-1 and a node on the side-face-2, respectively, and this applies in what follows. It should be remarked from the Kronecker property of the nodal basis function that $\varphi_{(1)}(s_1) = 1$, $\varphi_{(j)}(s_1) = 0$, $\psi_{(1)}(s_1) = 0$, $\psi_{(j)}(s_1) = 0$ $\forall j \geq 2$, $\varphi_{(1)}(s_2) = 0$, $\varphi_{(j)}(s_2) = 0$, $\psi_{(1)}(s_2) = 1$ and $\psi_{(j)}(s_2) = 0$ $\forall j \leq m-2$. Now, both the matrices \mathbf{N}^{S1} and \mathbf{N}^{S2} clearly contain many zero entries and simply take the form

$$\mathbf{N}^{S1} = \left\{ \mathbf{I}_{m \times m} \quad \mathbf{0}_{m \times m} \quad \mathbf{0}_{m \times m} \quad \mathbf{0}_{m \times m} \right\} \quad (4.18)$$

$$\mathbf{N}^{S2} = \left\{ \mathbf{0}_{m \times m} \quad \mathbf{0}_{m \times m} \quad \mathbf{I}_{m \times m} \quad \mathbf{0}_{m \times m} \right\} \quad (4.19)$$

Substituting (4.18) into (4.13) and (4.19) into (4.14) leads to

$$\bar{\mathbf{F}}_j^{V1} = (\mathbf{N}^{S1})^T \bar{\mathbf{V}}_{\Gamma_{1j}^s} J_1^\xi = \left\{ \bar{\mathbf{V}}_{\Gamma_{1j}^s} J_1^\xi \quad \mathbf{0} \quad \mathbf{0} \quad \dots \quad \mathbf{0} \right\}^T \quad (4.20)$$

$$\bar{\mathbf{F}}_j^{V2} = (\mathbf{N}^{S2})^T \bar{\mathbf{V}}_{\Gamma_{2j}^s} J_2^\xi = \left\{ \mathbf{0} \quad \dots \quad \mathbf{0} \quad \bar{\mathbf{V}}_{\Gamma_{2j}^s} J_2^\xi \quad \mathbf{0} \quad \mathbf{0} \right\}^T \quad (4.21)$$

$$\bar{\mathbf{F}}_j^{M11} = (\mathbf{B}_4^1)^T \bar{\mathbf{M}}_{\Gamma_{1j}^s} J_1^\xi \quad (4.22)$$

$$\bar{\mathbf{F}}_{j,\xi}^{M12} = (\mathbf{B}_3^1)^T \bar{\mathbf{M}}_{\Gamma_{1j}^s} J_1^\xi \quad (4.23)$$

$$\bar{\mathbf{F}}_j^{M21} = (\mathbf{B}_4^2)^T \bar{\mathbf{M}}_{\Gamma_2^s} J_2^\xi \quad (4.24)$$

$$\bar{\mathbf{F}}_{j,\xi}^{M22} = (\mathbf{B}_3^2)^T \bar{\mathbf{M}}_{\Gamma_2^s} J_2^\xi \quad (4.25)$$

Based on this form of prescribed data, the particular solution $\mathbf{W}_p^h(\xi)$ must take the form

$$\begin{aligned} \mathbf{W}_p^h(\xi) = & \sum_{\gamma_j \in \mathfrak{R}^*} \xi^{\gamma_j+4} c_j^p + \xi^3 \left\{ \sum_{\beta_j \in \mathfrak{R}^*} \xi^{\beta_j} c_j^{V1} + \sum_{\tau_j \in \mathfrak{R}^*} \xi^{\tau_j} c_j^{V2} + \sum_{\omega_j \in \mathfrak{R}^*} \xi^{\omega_j-1} c_j^{M11} + \sum_{\kappa_j \in \mathfrak{R}^*} \xi^{\kappa_j-1} c_j^{M21} \right. \\ & \left. - \sum_{\omega_j \in \mathfrak{R}^*} \omega_j \xi^{\omega_j-1} c_j^{dM12} - \sum_{\kappa_j \in \mathfrak{R}^*} \kappa_j \xi^{\kappa_j-1} c_j^{dM22} \right\} \quad (4.26) \end{aligned}$$

where c_j^p , c_j^{V1} , c_j^{V2} , c_j^{M11} , c_j^{dM12} , c_j^{M21} , c_j^{dM22} and c_j^{dM22} are vectors of unknown constants. By substituting (4.12)-(4.16) and (4.26) into (3.73), it leads to

$$\begin{aligned} & \sum_{\gamma_j \in \mathfrak{R}^*} \xi^{\gamma_j+4} \left[\{\mathcal{E}_0 + \mathcal{E}_1(\gamma_j+4) + \mathcal{E}_2(\gamma_j+4)(\gamma_j+3) + \mathcal{E}_3(\gamma_j+4)(\gamma_j+3)(\gamma_j+2) \right. \\ & \left. + \mathcal{E}_4(\gamma_j+4)(\gamma_j+3)(\gamma_j+2)(\gamma_j+1)\} c_j^p - \bar{\mathbf{F}}_j^p \right] + \\ & \sum_{\beta_j \in \mathfrak{R}^*} \xi^{\beta_j+3} \left[\{\mathcal{E}_0 + \mathcal{E}_1(\beta_j+3) + \mathcal{E}_2(\beta_j+3)(\beta_j+2) + \mathcal{E}_3(\beta_j+3)(\beta_j+2)(\beta_j+1) \right. \\ & \left. + \mathcal{E}_4(\beta_j+3)(\beta_j+2)(\beta_j+1)\beta_j\} c_j^{V1} - \bar{\mathbf{F}}_j^{V1} \right] + \\ & \sum_{\tau_j \in \mathfrak{R}^*} \xi^{\tau_j+3} \left[\{\mathcal{E}_0 + \mathcal{E}_1(\tau_j+3) + \mathcal{E}_2(\tau_j+3)(\tau_j+2) + \mathcal{E}_3(\tau_j+3)(\tau_j+2)(\tau_j+1) \right. \\ & \left. + \mathcal{E}_4(\tau_j+3)(\tau_j+2)(\tau_j+1)\tau_j\} c_j^{V2} - \bar{\mathbf{F}}_j^{V2} \right] + \end{aligned}$$

$$\begin{aligned}
& \sum_{\omega_j \in \mathfrak{H}^*} \xi^{\omega_j+2} \left[\{ \mathcal{E}_0 + \mathcal{E}_1(\omega_j+2) + \mathcal{E}_2(\omega_j+2)(\omega_j+1) + \mathcal{E}_3(\omega_j+2)(\omega_j+1)\omega_j \right. \\
& \left. + \mathcal{E}_4(\omega_j+2)(\omega_j+1)\omega_j(\omega_j-1) \right\} c_j^{M11} - \bar{\mathbf{F}}_j^{M11} \Big] + \\
& \sum_{\kappa_j \in \mathfrak{H}^*} \xi^{\kappa_j+2} \left[\{ \mathcal{E}_0 + \mathcal{E}_1(\kappa_j+2) + \mathcal{E}_2(\kappa_j+2)(\kappa_j+1) + \mathcal{E}_3(\kappa_j+2)(\kappa_j+1)\kappa_j \right. \\
& \left. + \mathcal{E}_4(\kappa_j+2)(\kappa_j+1)\kappa_j(\kappa_j-1) \right\} c_j^{M21} - \bar{\mathbf{F}}_j^{M21} \Big] \\
& \sum_{\omega_j \in \mathfrak{H}^*} \xi^{\omega_j+2} \left[\{ \mathcal{E}_0\omega_j + \mathcal{E}_1\omega_j(\omega_j+2) + \mathcal{E}_2\omega_j(\omega_j+2)(\omega_j+1) + \mathcal{E}_3\omega_j^2(\omega_j+2)(\omega_j+1) \right. \\
& \left. + \mathcal{E}_4\omega_j^2(\omega_j+2)(\omega_j+1)(\omega_j-1) \right\} c_j^{dM12} + \bar{\mathbf{F}}_{j,\xi}^{M12} \Big] + \\
& \sum_{\kappa_j \in \mathfrak{H}^*} \xi^{\kappa_j+2} \left[\{ \mathcal{E}_0\kappa_j + \mathcal{E}_1\kappa_j(\kappa_j+2) + \mathcal{E}_2\kappa_j(\kappa_j+2)(\kappa_j+1) + \mathcal{E}_3\kappa_j^2(\kappa_j+2)(\kappa_j+1) \right. \\
& \left. + \mathcal{E}_4\kappa_j^2(\kappa_j+2)(\kappa_j+1)(\kappa_j-1) \right\} c_j^{dM22} + \bar{\mathbf{F}}_{j,\xi}^{M22} \Big] = 0 \tag{4.27}
\end{aligned}$$

Equation (4.27) can be satisfied $\forall \xi \in (\xi_1, \xi_2)$ if and only if

$$\begin{aligned}
& \{ \mathcal{E}_0 + \mathcal{E}_1(\gamma_j+4) + \mathcal{E}_2(\gamma_j+4)(\gamma_j+3) + \mathcal{E}_3(\gamma_j+4)(\gamma_j+3)(\gamma_j+2) \\
& + \mathcal{E}_4(\gamma_j+4)(\gamma_j+3)(\gamma_j+2)(\gamma_j+1) \} c_j^p = \bar{\mathbf{F}}_j^p \tag{4.28}
\end{aligned}$$

$$\begin{aligned}
& \{ \mathcal{E}_0 + \mathcal{E}_1(\beta_j+3) + \mathcal{E}_2(\beta_j+3)(\beta_j+2) + \mathcal{E}_3(\beta_j+3)(\beta_j+2)(\beta_j+1) \\
& + \mathcal{E}_4(\beta_j+3)(\beta_j+2)(\beta_j+1)\beta_j \} c_j^{V1} = \bar{\mathbf{F}}_j^{V1} \tag{4.29}
\end{aligned}$$

$$\begin{aligned}
& \{ \mathcal{E}_0 + \mathcal{E}_1(\tau_j+3) + \mathcal{E}_2(\tau_j+3)(\tau_j+2) + \mathcal{E}_3(\tau_j+3)(\tau_j+2)(\tau_j+1) \\
& + \mathcal{E}_4(\tau_j+3)(\tau_j+2)(\tau_j+1)\tau_j \} c_j^{V2} = \bar{\mathbf{F}}_j^{V2} \tag{4.30}
\end{aligned}$$

$$\begin{aligned}
& \{ \mathcal{E}_0 + \mathcal{E}_1(\omega_j+2) + \mathcal{E}_2(\omega_j+2)(\omega_j+1) + \mathcal{E}_3(\omega_j+2)(\omega_j+1)\omega_j \\
& + \mathcal{E}_4(\omega_j+2)(\omega_j+1)\omega_j(\omega_j-1) \} c_j^{M11} = \bar{\mathbf{F}}_j^{M11} \tag{4.31}
\end{aligned}$$

$$\begin{aligned}
& \{ \mathcal{E}_0 + \mathcal{E}_1(\kappa_j+2) + \mathcal{E}_2(\kappa_j+2)(\kappa_j+1) + \mathcal{E}_3(\kappa_j+2)(\kappa_j+1)\kappa_j \\
& + \mathcal{E}_4(\kappa_j+2)(\kappa_j+1)\kappa_j(\kappa_j-1) \} c_j^{M21} = \bar{\mathbf{F}}_j^{M21} \tag{4.32}
\end{aligned}$$

$$\begin{aligned}
& \{ \mathcal{E}_0\omega_j + \mathcal{E}_1\omega_j(\omega_j+2) + \mathcal{E}_2\omega_j(\omega_j+2)(\omega_j+1) + \mathcal{E}_3\omega_j^2(\omega_j+2)(\omega_j+1) \\
& + \mathcal{E}_4\omega_j^2(\omega_j+2)(\omega_j+1)(\omega_j-1) \} c_j^{dM12} + \bar{\mathbf{F}}_{j,\xi}^{M12} = 0 \tag{4.33}
\end{aligned}$$

$$\begin{aligned}
& \{ \mathcal{E}_0\kappa_j + \mathcal{E}_1\kappa_j(\kappa_j+2) + \mathcal{E}_2\kappa_j(\kappa_j+2)(\kappa_j+1) + \mathcal{E}_3\kappa_j^2(\kappa_j+2)(\kappa_j+1) \\
& + \mathcal{E}_4\kappa_j^2(\kappa_j+2)(\kappa_j+1)(\kappa_j-1) \} c_j^{dM22} + \bar{\mathbf{F}}_{j,\xi}^{M22} = 0 \tag{4.34}
\end{aligned}$$

A system of linear algebraic equations (4.28)-(4.34) is sufficient for determining all unknown constant vectors c_j^p , c_j^{V1} , c_j^{V2} , c_j^{M11} , c_j^{M21} , c_j^{dM12} and c_j^{dM22} . Once the particular solution $\mathbf{W}_p^h(\xi)$ is obtained, the corresponding particular the nodal internal force and moment, denoted by $\mathbf{q}_p^h(\xi)$ and $\mathbf{m}_p^h(\xi)$ respectively, are given by

$$\mathbf{q}_p^h(\xi) = \mathcal{G}_0 \mathbf{W}_p^h + \mathcal{G}_1 \mathbf{W}_{p,\xi}^h + \mathcal{G}_2 \mathbf{W}_{p,\xi\xi}^h + \mathcal{G}_3 \mathbf{W}_{p,\xi\xi\xi}^h \quad (4.35)$$

$$\mathbf{m}_p^h(\xi) = \frac{1}{\xi} \mathbf{E}_2 \mathbf{W}_p^h + \mathbf{E}_1 \mathbf{W}_{p,\xi}^h + \xi \mathbf{E}_0 \mathbf{W}_{p,\xi\xi}^h \quad (4.36)$$

4.3 Final General Solution

The general solution $\mathbf{W}^h(\xi)$ of the system of differential equations (3.73) and the corresponding general nodal internal force $\mathbf{q}^h(\xi)$ and general nodal bending moment $\mathbf{m}^h(\xi)$ are then given by

$$\mathbf{W}^h(\xi) = \mathbf{W}_h^h(\xi) + \mathbf{W}_p^h(\xi) = \mathbf{F}_w(\xi) \mathbf{C} + \mathbf{W}_p^h(\xi) \quad (4.37)$$

$$\mathbf{q}^h(\xi) = \mathbf{q}_h^h(\xi) + \mathbf{q}_p^h(\xi) = \mathbf{F}_q(\xi) \mathbf{C} + \mathbf{q}_p^h(\xi) \quad (4.38)$$

$$\mathbf{m}^h(\xi) = \mathbf{m}_h^h(\xi) + \mathbf{m}_p^h(\xi) = \mathbf{F}_m(\xi) \mathbf{C} + \mathbf{m}_p^h(\xi) \quad (4.39)$$

where $\mathbf{q}_h^h(\xi)$, $\mathbf{m}_h^h(\xi)$, $\mathbf{q}_p^h(\xi)$ and $\mathbf{m}_p^h(\xi)$ are given by (4.5), (4.6), (4.35) and (4.36), respectively. To determine the constants contained in \mathbf{C} , the boundary conditions on both inner and outer boundaries are enforced. By substituting (4.38) and (4.39) into (3.74), it results in

$$-\begin{bmatrix} \mathcal{G}_3 & \mathcal{G}_2 & \mathcal{G}_1 & \mathcal{G}_0 \\ 0 & \xi \mathbf{E}_0 & \mathbf{E}_1 & \frac{1}{\xi} \mathbf{E}_2 \end{bmatrix} \begin{bmatrix} \mathbf{F}_w(\xi_1)_{,\xi\xi\xi\xi} \\ \mathbf{F}_w(\xi_1)_{,\xi\xi\xi} \\ \mathbf{F}_w(\xi_1)_{,\xi\xi} \\ \mathbf{F}_w(\xi_1)_{,\xi} \\ \mathbf{F}_w(\xi_1) \end{bmatrix} \mathbf{C} - \begin{bmatrix} \mathcal{G}_3 & \mathcal{G}_2 & \mathcal{G}_1 & \mathcal{G}_0 \\ 0 & \xi \mathbf{E}_0 & \mathbf{E}_1 & \frac{1}{\xi} \mathbf{E}_2 \end{bmatrix} \begin{bmatrix} \mathbf{W}_p^h(\xi_1)_{,\xi\xi\xi\xi} \\ \mathbf{W}_p^h(\xi_1)_{,\xi\xi\xi} \\ \mathbf{W}_p^h(\xi_1)_{,\xi\xi} \\ \mathbf{W}_p^h(\xi_1)_{,\xi} \\ \mathbf{W}_p^h(\xi_1) \end{bmatrix} = \begin{Bmatrix} \mathcal{P}_1 \\ \mathbf{M}^{12} \end{Bmatrix} \quad (4.40)$$

$$\begin{bmatrix} \mathcal{G}_3 & \mathcal{G}_2 & \mathcal{G}_1 & \mathcal{G}_0 \\ 0 & \xi \mathbf{E}_0 & \mathbf{E}_1 & \frac{1}{\xi} \mathbf{E}_2 \end{bmatrix} \begin{bmatrix} \mathbf{F}_w(\xi_2)_{,\xi\xi\xi\xi} \\ \mathbf{F}_w(\xi_2)_{,\xi\xi\xi} \\ \mathbf{F}_w(\xi_2)_{,\xi\xi} \\ \mathbf{F}_w(\xi_2)_{,\xi} \\ \mathbf{F}_w(\xi_2) \end{bmatrix} \mathbf{C} + \begin{bmatrix} \mathcal{G}_3 & \mathcal{G}_2 & \mathcal{G}_1 & \mathcal{G}_0 \\ 0 & \xi \mathbf{E}_0 & \mathbf{E}_1 & \frac{1}{\xi} \mathbf{E}_2 \end{bmatrix} \begin{bmatrix} \mathbf{W}_p^h(\xi_2)_{,\xi\xi\xi\xi} \\ \mathbf{W}_p^h(\xi_2)_{,\xi\xi\xi} \\ \mathbf{W}_p^h(\xi_2)_{,\xi\xi} \\ \mathbf{W}_p^h(\xi_2)_{,\xi} \\ \mathbf{W}_p^h(\xi_2) \end{bmatrix} = \begin{Bmatrix} \mathcal{P}_2 \\ \mathbf{M}^{22} \end{Bmatrix} \quad (4.41)$$

The two systems of equations (4.40) and (4.41) can be combined to obtain

$$\begin{Bmatrix} \mathcal{P}_1 \\ \mathbf{M}^{12} \\ \mathcal{P}_2 \\ \mathbf{M}^{22} \end{Bmatrix} = \begin{Bmatrix} -\mathbf{F}_q(\xi_1) \\ -\mathbf{F}_m(\xi_1) \\ \mathbf{F}_q(\xi_2) \\ \mathbf{F}_m(\xi_2) \end{Bmatrix} \mathbf{C} + \begin{Bmatrix} -\mathbf{q}_p^h(\xi_1) \\ -\mathbf{m}_p^h(\xi_1) \\ \mathbf{q}_p^h(\xi_2) \\ \mathbf{m}_p^h(\xi_2) \end{Bmatrix} = \mathbf{F}_f \mathbf{C} + \mathbf{F}_{fp} \quad (4.42)$$

Similarly, kinematical conditions on both inner and outer boundaries of the domain can be also obtained as

$$\begin{Bmatrix} \mathbf{w}_1 \\ \theta_1 \\ \mathbf{w}_2 \\ \theta_2 \end{Bmatrix} = \begin{Bmatrix} \mathbf{W}^h(\xi_1) \\ \mathbf{W}_{,\xi}^h(\xi_1) \\ \mathbf{W}^h(\xi_2) \\ \mathbf{W}_{,\xi}^h(\xi_2) \end{Bmatrix} = \mathbf{F}_c \mathbf{C} + \mathbf{F}_{cp} \quad (4.43)$$

where \mathbf{F}_c and \mathbf{F}_{cp} are defined by

$$\mathbf{F}_c = \begin{Bmatrix} \mathbf{F}_w(\xi_1) \\ \mathbf{F}_{w,\xi}(\xi_1) \\ \mathbf{F}_w(\xi_2) \\ \mathbf{F}_{w,\xi}(\xi_2) \end{Bmatrix}, \quad \mathbf{F}_{cp} = \begin{Bmatrix} \mathbf{W}_p^h(\xi_1) \\ \mathbf{W}_{p,\xi}^h(\xi_1) \\ \mathbf{W}_p^h(\xi_2) \\ \mathbf{W}_{p,\xi}^h(\xi_2) \end{Bmatrix} \quad (4.44)$$

From the relation (4.43), the constant vector \mathbf{C} can be expressed as

$$\mathbf{C} = \mathbf{F}_c^{-1} \mathbf{U} - \mathbf{F}_c^{-1} \mathbf{F}_{cp} \quad (4.45)$$

where the vector \mathbf{U} is defined by

$$\mathbf{U} = \begin{Bmatrix} \mathbf{w}_1 \\ \theta_1 \\ \mathbf{w}_2 \\ \theta_2 \end{Bmatrix} \quad (4.46)$$

By substituting (4.45) into the relation (4.42), it leads to a well-known system of linear algebraic equations

$$\mathbf{P} = \mathbf{K} \mathbf{U} \quad (4.47)$$

where the load vector \mathbf{P} and the stiffness matrix \mathbf{K} are defined by

$$\mathbf{P} = \mathbf{P}_h + \mathbf{P}_p; \mathbf{P}_h = \begin{Bmatrix} \mathcal{P}_1 \\ \mathbf{M}^{12} \\ \mathcal{P}_2 \\ \mathbf{M}^{22} \end{Bmatrix}, \mathbf{P}_p = \mathbf{F}_f \mathbf{F}_c^{-1} \mathbf{F}_{cp} - \mathbf{F}_{fp} \quad (4.48)$$

$$\mathbf{K} = \mathbf{F}_f \mathbf{F}_c^{-1} \quad (4.49)$$

By enforcing both essential and natural boundary conditions on the inner and outer boundaries of the plate, the system of linear algebraic equations (4.47) can be solved to obtain all unknowns on the boundary. Once (4.47) is solved, the constant vector \mathbf{C} and the general solution $\mathbf{W}^h(\xi)$ can be obtained from equations (4.45) and (4.37), respectively.

4.4 Post-Process for Field Quantities

Once the approximate general solution $\mathbf{W}^h(\xi)$ is obtained, the approximate transverse displacement at any point (ξ, s) can be obtained from (3.24) as

$$w^h(\xi, s) = \mathbf{N}^S \mathbf{W}^h = \mathbf{N}^S \left[\mathbf{W}_h^h(\xi) + \mathbf{W}_p^h(\xi) \right] \quad (4.50)$$

The approximate in-plane moment \mathbf{M}^h can be also computed from (3.25) as

$$\begin{aligned} \mathbf{M}^h(\xi, s) = -\mathbf{E} \left(\frac{1}{\xi^2} \mathbf{B}_{68} \left(\mathbf{W}_h^h(\xi) + \mathbf{W}_p^h(\xi) \right) + \frac{1}{\xi} \mathbf{B}_{59} \left(\mathbf{W}_h^h(\xi)_{,\xi} + \mathbf{W}_p^h(\xi)_{,\xi} \right) \right. \\ \left. + \mathbf{B}_7 \left(\mathbf{W}_h^h(\xi)_{,\xi\xi} + \mathbf{W}_p^h(\xi)_{,\xi\xi} \right) \right) \end{aligned} \quad (4.51)$$

CHAPTER 5

H-HIERARCHICAL ADAPTIVITY

A level of discretization in the boundary direction has the significant effect on the accuracy of approximation solutions by the scaled boundary finite element method. An insufficient discretization level can lead to incorrect numerical results [65]. Since the exact solution is unknown a priori, the error of approximate solutions must be estimated in a certain fashion. In the present study, a moment-recovery error estimator is developed to control the adaptive procedure and to provide a solution with an optimal error within a prescribed cost range. The discretization along the boundary direction is adapted automatically and the solution procedure described above is repeated until the estimated error is less than the target error. To specify exact values of all displacements or moments under a specified tolerance, the general criterion used for indicating total error in engineering use is the energy norm. It is required that the error does not exceed a specified percentage of the total energy norm of the solution. However, using a moments-recovery of error estimator, it is possible to adaptively refine the mesh in order to acquire the accuracy of certain quantities of interest. The h -refinement with the same class of elements but different in size, either larger or smaller in some locations, is introduced in order to provide optimal economy in achieving the desired solution.

5.1 Moments-recovery and Error Estimation

An error estimator is determined based on the recovered moment field and the bending energy norm specialized for plate bending problems using the SBFEM. The procedure is analogous to that employed by [31] for linear elasticity problems. In this approach, a recovery procedure is utilized to construct an approximation of an exact moment field within the plate. The recovery total error estimator $\bar{\eta}^*$ can be defined as

$$\bar{\eta}^* = \frac{\|e_M^*(\xi, s)\|_A}{\|\mathbf{M}^*(\xi, s)\|_A} \times 100\% \quad (5.1)$$

where $\mathbf{M}^*(\xi, s)$ is the recovered moment field, $e_M^*(\xi, s) = \mathbf{M}^*(\xi, s) - \mathbf{M}^h(\xi, s)$ is the error function of the approximate moment field $\mathbf{M}^h(\xi, s)$, and $\|\cdot\|_A$ is a properly selected norm. The approximate moment $\mathbf{M}^h(\xi, s)$ given by (3.25), which is a weighted sum of the modal vertical deflections, can be re-written as

$$\mathbf{M}^h = \sum_{i=1}^N c_i \mathbf{m}_i(\xi, s) \quad (5.2)$$

where the modal moment $\mathbf{m}_i(\xi, s)$ is defined by

$$\mathbf{m}_i(\xi, s) = -\mathbf{E}[\mathbf{B}_{68} + \lambda_i \mathbf{B}_{59} + \lambda_i(\lambda_i - 1)\mathbf{B}_7] \phi_i^{\xi \lambda_i - 2} \quad (5.3)$$

A recovered modal moment, denoted by $\mathbf{m}_i^*(\xi, s)$, is sought in a form

$$\mathbf{m}_i^*(\xi, s) = \mathbf{N}^S \bar{\mathbf{m}}_i^* \xi^{\lambda_i - 2} \quad (5.4)$$

where $\bar{\mathbf{m}}_i^*$ denotes the recovered modal moment at the boundary nodes. In the present study, a procedure analogous to the work of [31] together with the least square technique is employed to construct $\bar{\mathbf{m}}_i^*$. It is evident from (5.4) that each modal moment field is C^2 -continuous in radial and circumferential directions. The total recovered moment field can be formed by multiplying each recovered modal moment field by the corresponding modal participation factor c_i by

$$\mathbf{M}^*(\xi, s) = \sum_{i=1}^N c_i \mathbf{m}_i^*(\xi, s) = \sum_{i=1}^N c_i \xi^{\lambda_i - 2} \mathbf{N}^S \bar{\mathbf{m}}_i^* \quad (5.5)$$

The recovery error function is then obtained as

$$\begin{aligned} \mathbf{e}_M^*(\xi, s) &= \mathbf{M}^*(\xi, s) - \mathbf{M}^h(\xi, s) \\ &= \sum_{i=1}^N c_i \xi^{\lambda_i - 2} \left[\mathbf{N}^S \bar{\mathbf{m}}_i^* + \mathbf{E} \left[\mathbf{B}_{68} + \lambda_i \mathbf{B}_{59} + \lambda_i (\lambda_i - 1) \mathbf{B}_7 \right] \boldsymbol{\phi} \right] \\ &= \sum_{i=1}^N c_i \xi^{\lambda_i - 2} \mathbf{e}_{M_i}^*(s) \end{aligned} \quad (5.6)$$

In the present study, $\|\cdot\|_A$ is chosen as the total energy norm defined for any function $f(\xi, s)$ such that

$$\|f(\xi, s)\|_A = \left(\int_A \mathbf{f}^T \mathbf{E}^{-1} \mathbf{f} dA \right)^{1/2} \quad (5.7)$$

The energy norm of the error function $\mathbf{e}_M^*(\xi, s)$ can then be obtained by substituting (3.7) and (5.6) into (5.7) and the result is given by

$$\|\mathbf{e}_M^*(\xi, s)\|_A = \left(\sum_{e=1}^n \|\mathbf{e}_M^*(\xi, s)\|_e^2 \right)^{1/2} \quad (5.8)$$

where n is the number of elements in the discretization, $\|\mathbf{e}_M^*(\xi, s)\|_e$ denotes the energy norm of the error in moment within the region modeled by an element e . By using (5.6), it leads to

$$\|\mathbf{e}_M^*(\xi, s)\|_e = \left(\sum_{i=1}^N \sum_{j=1}^N c_i c_j I(\lambda_i, \lambda_j) \int_{S_e} (\mathbf{e}_{M_i}^*(s))^T \mathbf{E}^{-1} \mathbf{e}_{M_j}^*(s) J ds \right)^{1/2} \quad (5.9)$$

where $I(\lambda_i, \lambda_j)$ is a constant resulting from the direct integration of the function $\xi^{\lambda_i + \lambda_j - 3}$ in the radial direction. It is evident that the value of $I(\lambda_i, \lambda_j)$ depends on the values of eigenvalues λ_i, λ_j and the range of integration from the inner to outer boundaries. The energy norm of the recovered moment field can be also computed in the same way as

$$\|\mathbf{M}^*(\xi, s)\|_A = \left(\sum_{i=1}^N \sum_{j=1}^N c_i c_j I(\lambda_i, \lambda_j) \int_S (\bar{\mathbf{m}}_j^*(s))^T \mathbf{E}^{-1} \bar{\mathbf{m}}_j^*(s) J ds \right)^{1/2} \quad (5.10)$$

where $\bar{\mathbf{m}}_j^*(s)$ denotes the recovered modal moment on the boundary and $\mathbf{e}_{M_j}^*(s)$ is the modal moment error on the boundary. Equations (5.9) and (5.10) can be substituted into (5.1) to determine the total error estimator $\bar{\eta}^*$.

5.2 An h -hierarchical Adaptive Procedure

In general, the size of elements used in the approximation is reduced in regions possessing large error under the h -hierarchical adaptive scheme. The whole mesh is regenerated from the definition of the domain boundary and the profile of computed errors at each analysis step. This type of adaptive procedure can be simply incorporated into the existing scaled boundary finite element method [59]. The basic algorithm for the adaptivity is straightforward and can be illustrated in Figure 5.1.

The shape functions from the coarser meshes are retained as the basis for constructing the shape functions for the finer meshes in the h -hierarchical scheme. A simple method to achieve this is to subdivide any elements in which its error is higher than the target error at each analysis step in the adaptive process. Every subsequent mesh always contains all nodes of the previous mesh. In addition, the mesh structure can be demonstrated efficiently by a tree structure as illustrated in Figure 5.2. Ideally, such approach is suitable for object-oriented programming and recursive techniques. For one-dimensional elements, a binary tree may be utilized in order to describe the refined mesh. A basic example is shown in Figure 5.2. The aim of all adaptive procedure is to offer the user a specified level of accuracy at a minimal computational cost. In the present investigation, the following optimal criterion is employed

$$\|\mathbf{e}_M^*(\xi, s)\|_e \leq \eta^* \sqrt{\|\mathbf{M}^*(\xi, s)\|_A^2 / n} \quad (5.11)$$

where η^* denotes the target error in the energy norm of each element. When the initial coarse mesh is built, a first scale boundary finite element analysis is performed and the energy norm of the error for a region described by each element $\|\mathbf{e}_M^*(\xi, s)\|_e$ is computed. Each element will be refined if the above criterion (5.11) is not satisfied. The analysis process is repeated until the estimated error of each element becomes less than the target error for the entire discretization.

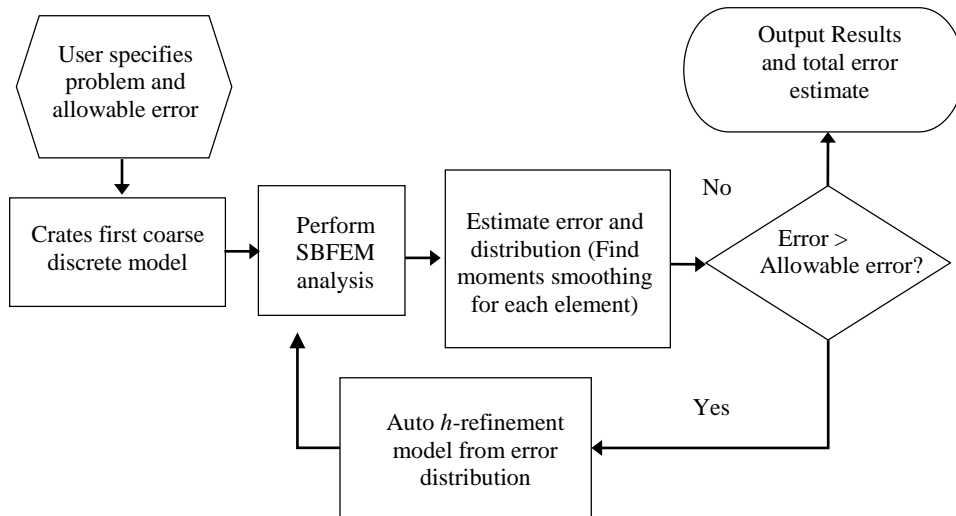


Figure 5.1: Diagram indicating algorithm for h -hierarchical adaptive scheme in scaled boundary finite element method (Adapted from “The scaled boundary finite element method” by Wolf, J.P., 2003, *Book of John Wiley & Sons Ltd*, p. 336 [30])

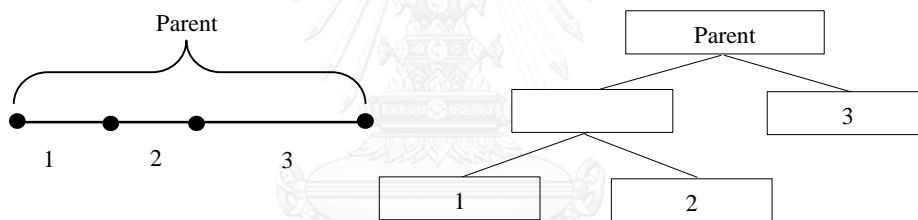


Figure 5.2: Local refinement strategies; an h -hierarchical refinement is related to a binary tree of two-node line elements (Adapted from “The scaled boundary finite element method” by Wolf, J.P., 2003, *Book of John Wiley & Sons Ltd*, p. 336 [30])

CHAPTER 6

NUMERICAL RESULTS

The proposed scaled boundary finite element method together with the h -hierarchical adaptive scheme has been successfully implemented in terms of an in-house computer code. In this chapter, results of various representative examples are reported to not only verify the formulation and numerical implementation but also demonstrate the accuracy and computational efficiency of the developed SBFEM. In the verification, plate problems with existing reference and analytical solutions are considered.

6.1 Verifications

Several problems with analytical or reference solutions are presented in this section to verify the implemented SBFEM without using the adaptive algorithm. Standard two-node elements with Hermite cubic shape functions are employed in the discretization of the trial and test functions whereas standard two-node, linear, straight and circular-arc elements are utilized to discretize the straight and circular-arc defining curves, respectively.

6.1.1 Circular plate with concentric hole under transverse shear

First, consider a circular elastic plate containing a concentric circular hole as shown schematically in Figure 6.1. The thickness, outer radius and inner radius of the plate are given by t , b and a , respectively, and Young modulus and Poisson ratio of the constituting material are given by $E = 200,000 \text{ N/mm}^2$ and $\nu = 0.3$. The plate is fully fixed against the movement along the entire outer boundary whereas its inner boundary is subjected to a uniform transverse shear load $\bar{V} = 10 \text{ N/cm}$. For this particular problem, the analytical solution for the deflection and the bending moment can be readily constructed using results from the work of [66].

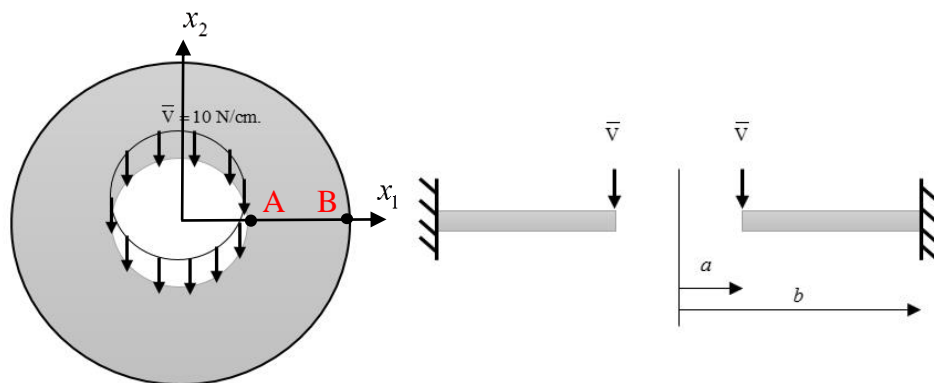


Figure 6.1: Schematic of circular plate containing concentric circular hole clamped along its entire outer boundary and loaded by uniform transverse shear load along its entire inner boundary

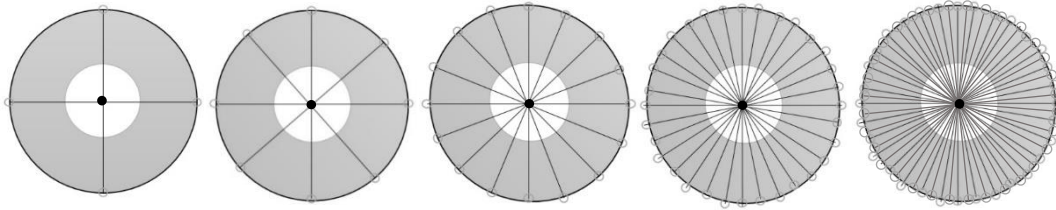


Figure 6.2: Schematic of uniform meshes with 4, 8, 16, 32 and 64 two-node elements used in discretization of defining curve

The center of the plate and the outer boundary are chosen as the scaling center and the defining curve, respectively. Meshes of the defining curve used in the analysis are shown in Figure 6.2. The computed numerical results are reported in Table 6.1-Table 6.3 for the deflection at a point A, the bending moment at a point B and the radial rotation at a point A, respectively. It can be seen that numerical solutions generated by the proposed technique for all meshes are in good agreement with the analytical solutions. The convergence of numerical results is investigated and confirmed, and the percent error of field quantities is also plotted against the number of elements used in the discretization in Figure 6.3. Obtained results indicate that the rate of convergence for the bending moment is lower than that of the deflection. It is evident from results shown in Figure 6.4 that the proposed technique exhibit excellent convergence characteristics to analytical solutions as the number of elements in the discretization increases; the discretization with only four elements can accurately capture the solution with error less than $1 \times 10^{-6}\%$ in comparison with the analytical solution.

Table 6.1: Deflection at point A for circular plate containing concentric circular hole clamped along its outer boundary and loaded by uniform transverse shear load along inner boundary for various ratios of t/b .

Elem. (Dof.)	t/b			
	0.1 (e-3)	0.05 (e-2)	0.02	0.005
4 (8)	0.1271928833	0.1017543068	0.0158991104	1.0175430620
8 (16)	0.1271928829	0.1017543063	0.0158991104	1.0175430639
16 (32)	0.1271928830	0.1017543064	0.0158991104	1.0175430642
32 (64)	0.1271928832	0.1017543065	0.0158991104	1.0175430638
64 (128)	0.1271928829	0.1017543061	0.0158991104	1.0175430645
Analytical sol.	0.1271928830	0.1017543064	0.0158991104	1.0175430639

Table 6.2: Radial bending moment at point B ($M_r \times 10^2$) for circular plate containing concentric circular hole clamped along its outer boundary and loaded by uniform transverse shear load along inner boundary for various ratios of t/b .

Elem. (Dof.)	t/b			
	0.1	0.05	0.02	0.005
4 (8)	-2.3793796522	-2.3793796788	-2.3793796813	-2.3793796846
8 (16)	-2.3793796581	-2.3793796798	-2.3793796838	-2.3793797197
16 (32)	-2.3793796235	-2.3793796585	-2.3793796423	-2.3793796749
32 (64)	-2.3793794513	-2.3793794449	-2.3793795144	-2.3793795784
64 (128)	-2.3793802323	-2.3793802683	-2.3793807904	-2.3793796653
Analytical sol.	-2.3793796765	-2.3793796765	-2.3793796765	-2.3793796765

Table 6.3: Radial rotation at point A (θ_r) for circular plate containing concentric circular hole clamped along its outer boundary and loaded by uniform transverse shear load along inner boundary for various ratios of t/b .

Elem. (Dof.)	t/b			
	0.1 (e-5)	0.05 (e-4)	0.02 (e-3)	0.005 (e-2)
4 (8)	-0.4236789258	-0.3389431402	-0.5295986603	-3.3894314393
8 (16)	-0.4236789281	-0.3389431423	-0.5295986603	-3.3894314251
16 (32)	-0.4236789284	-0.3389431427	-0.5295986606	-3.3894314265
32 (64)	-0.4236789286	-0.3389431434	-0.5295986604	-3.3894314265
64 (128)	-0.4236789282	-0.3389431410	-0.5295986602	-3.3894314286
Analytical sol.	-0.4236789283	-0.3389431426	-0.5295986603	-3.3894314261

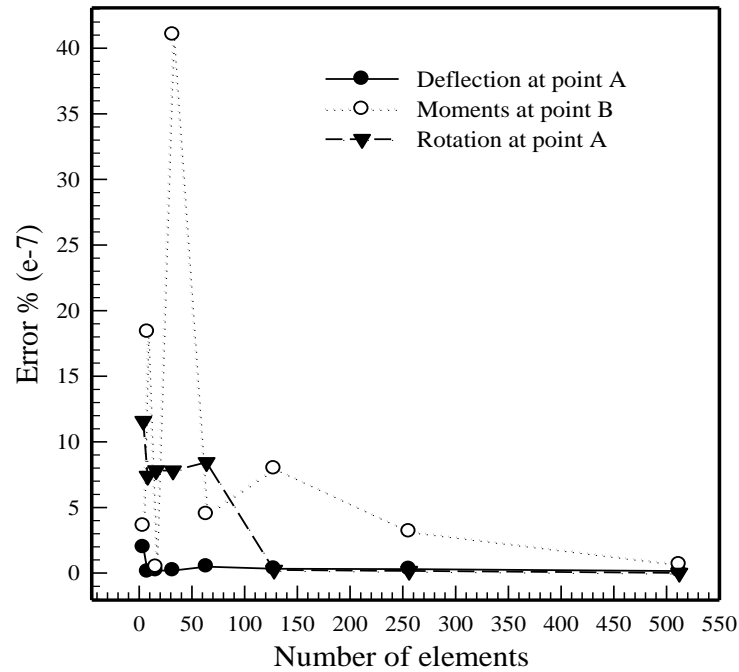


Figure 6.3: Percent error of numerical solutions versus number of elements for circular plate containing concentric circular hole clamped along its outer boundary and loaded by uniform transverse shear load along inner boundary ($t/b = 0.05$).

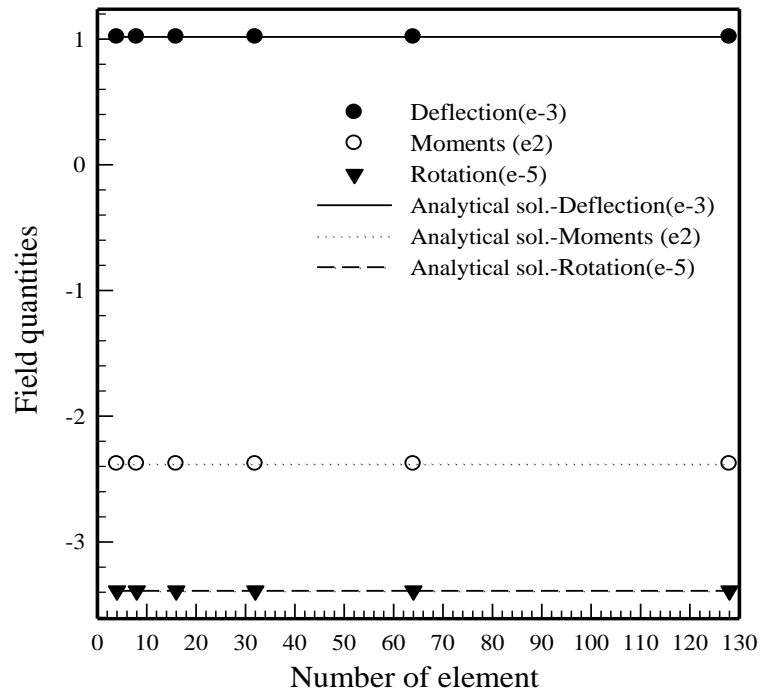


Figure 6.4: Deflection at point A, radial bending moment at point B, and radial rotation at point A of circular plate containing concentric circular hole clamped along its outer boundary and loaded by uniform transverse shear load along inner boundary ($t/b = 0.05$).

6.1.2 Circular plate under applied moment

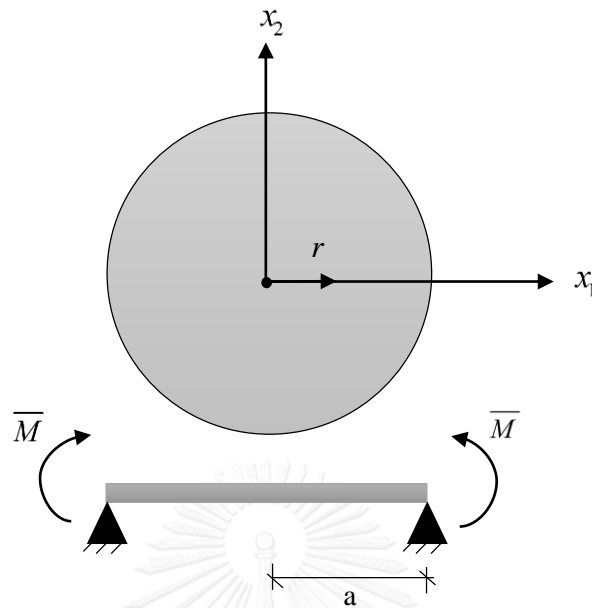


Figure 6.5: Schematic of simply-supported, elastic, circular plate subjected to moments along its boundary

Now, consider a simply-supported, elastic, circular plate of radius $a = 20$ cm and thickness $t = 0.2$ cm as shown in Figure 6.6. The plate is made of an isotropic, linearly elastic material with Young modulus $E = 200,000$ N/mm² and Poisson ratio $\nu = 0.3$ and subjected to the distributed moment $\bar{M} = 275$ N-cm/cm. The scaling center is chosen at the center of the plate and the outer boundary is treated as the defining curve. For this particular problem, the analytical solution for the transverse displacement is given, again, by [66].

Table 6.4: Deflection for simply-supported, elastic, circular plate subjected to distributed moments along its boundary.

Elem. (Dof.)	r/a				
	0	0.25	0.5	0.75	1
2(4)	2.8586169	2.7070244	2.1656213	1.2632802	0.0000000
4 (8)	2.8586444	2.7070306	2.1656240	1.2632808	0.0000000
8 (16)	2.8640574	2.7070500	2.1656298	1.2632825	0.0000000
16 (32)	2.8641574	2.7070300	2.1656264	1.2632825	0.0000000
Analytical sol.	2.8875000	2.7070312	2.1656250	1.2632813	0.0000000

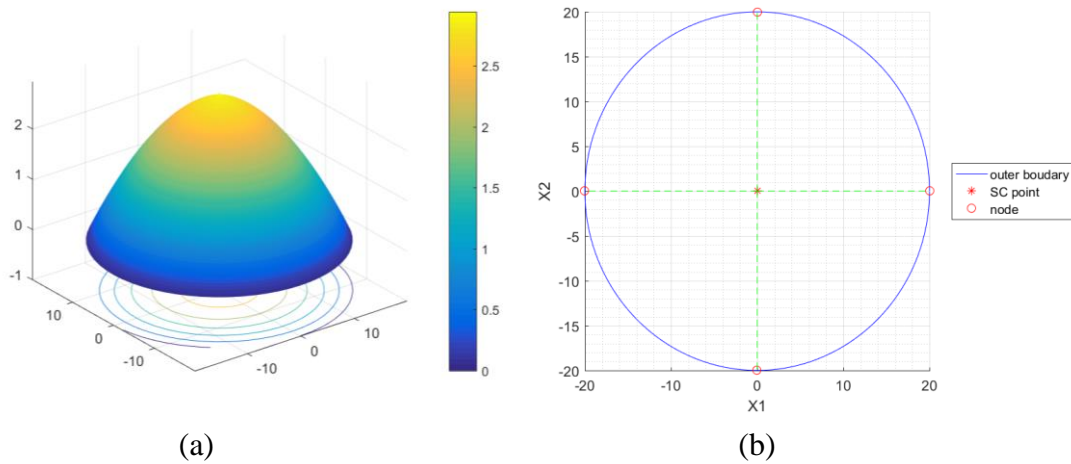


Figure 6.6: (a) Plot of deflection for simply-supported, elastic, circular plate subjected to distributed moments along its boundary and (b) mesh containing 4 elements.

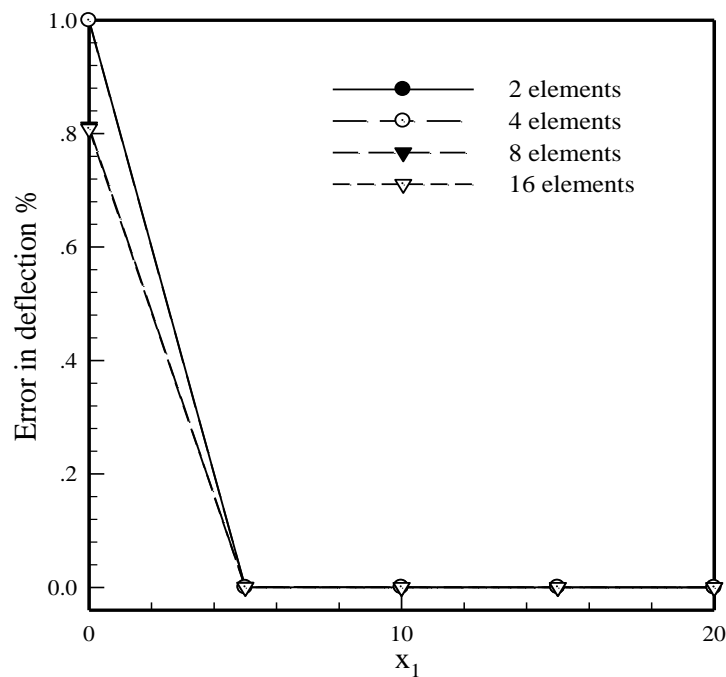


Figure 6.7: Error in deflection of simply-supported, elastic, circular plate subjected to distributed moments along its boundary

The scaled boundary finite element mesh used in the analysis is shown in Figure 6.6(b). The transverse deflection along the radial direction of the plate is reported in Table 6.4 for various values of the ratio r/a and, as illustrated in Figure 6.6(a), the maximum deflection occurs at the center of the plate. The percent error of computed deflection along the x_1 -direction is also shown in Figure 6.7 for four different levels of discretization. Clearly, the maximum error in deflection occurs at the scaling center.

6.1.3 Circular plate with concentric hole under applied moment

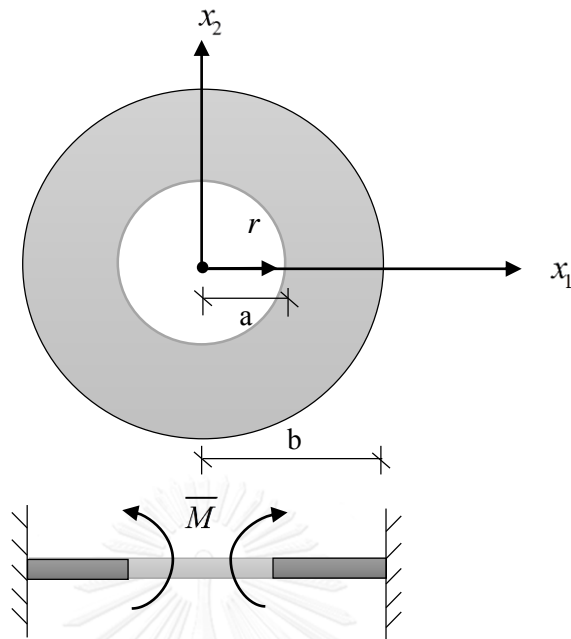


Figure 6.8: Schematic of circular plate containing concentric circular hole and subjected to uniform moments along its inner boundary

Consider, next, an elastic circular plate containing a concentric circular hole and fully clamped along its outer boundary as shown in Figure 6.8. The thickness t , the inner radius a , and the outer radius b of the plate are taken as $t = 5$ cm, $a = 50$ cm, and $b = 100$ cm, respectively. The plate is made of an isotropic, linearly elastic material with Young modulus $E = 200,000$ N/mm² and Poisson ratio $\nu = 0.3$ and subjected to uniformly distributed moment $\bar{M} = 250$ N-cm/cm along its entire inner boundary. The closed form solution for the transverse displacement for this particular case is obtained by the method of superposition along with results reported by [66]. In the analysis, the scaling center and the defining curve are chosen at the center of the plate and the outer boundary, respectively, and six meshes containing 4, 8, 16, 32, 64 and 128 two-node elements are adopted as indicated in Figure 6.9.

The computed deflections along the radial direction of the plate for different levels of discretization are reported in Figure 6.10 and Table 6.5 in comparison with the analytical solution. The percent error of the computed deflection along the x_1 -direction is also shown in Figure 6.11. It is evident from these results that the discretization with only four elements can accurately capture the solution with error less than 0.0004% in comparison with the analytical solution. The maximum deflection of the plate occurs along the inner boundary of the plate for this particular loading condition as can be seen in Figure 6.12(a). In addition, profiles of the bending moments M_{11}^h , M_{22}^h and M_{12}^h obtained from the mesh with 8 elements are also shown in Figure 6.12(b)-(c).

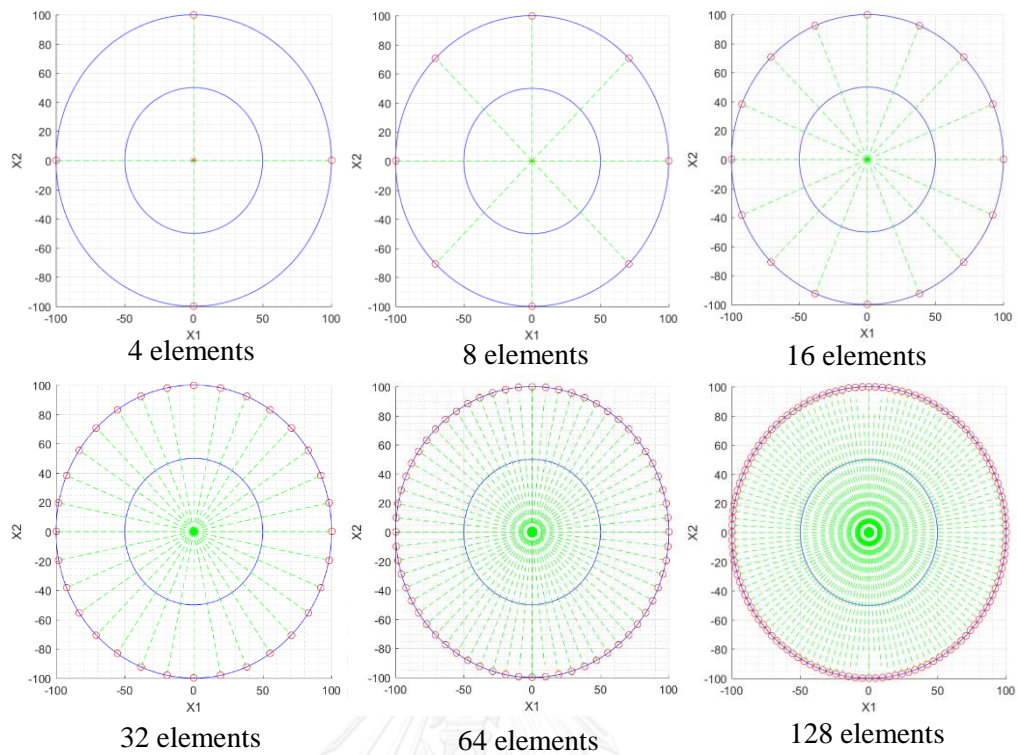


Figure 6.9: Schematic of six meshes containing 4, 8, 16, 32, 64 and 128 elements used in discretization of defining curve.

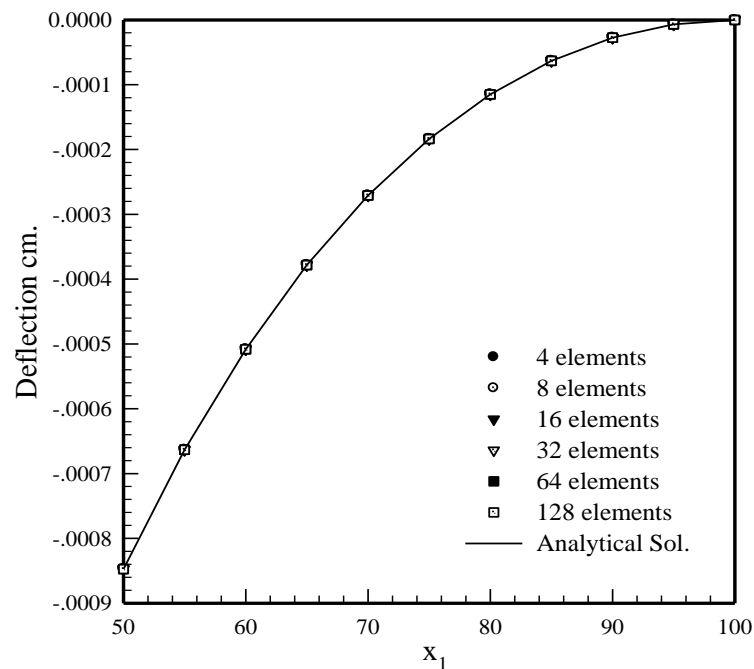


Figure 6.10: Deflections along the radial direction of circular plate containing concentric circular hole and subjected to uniform moments along its inner boundary for different levels of discretization.

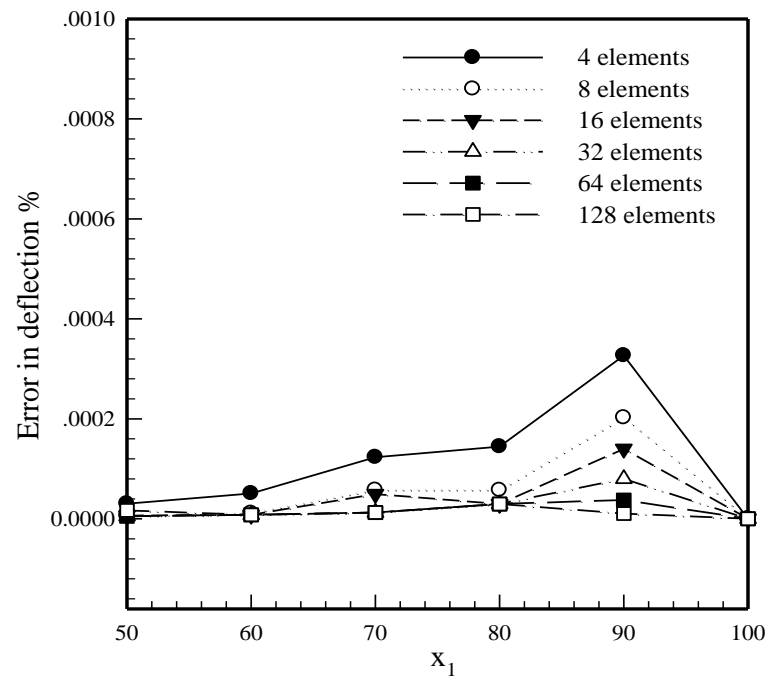


Figure 6.11: Percent error in deflection along the radial direction of circular plate containing concentric circular hole and subjected to uniform moments along its inner boundary.

Table 6.5: Deflection along radial direction of circular plate containing concentric circular hole and subjected to uniform moments along its inner boundary.

Elem. (Dof.)	r/b					
	0.5	0.6	0.7	0.8	0.9	1
4 (8)	0.0008473576	0.0005082475	0.0002708022	0.0001149090	0.0000275940	0.0000000001
8 (16)	0.0008473578	0.0005082477	0.0002708021	0.0001149091	0.0000275941	0.0000000000
16 (32)	0.0008473578	0.0005082478	0.0002708024	0.0001149092	0.0000275942	0.0000000000
32 (64)	0.0008473579	0.0005082478	0.0002708025	0.0001149092	0.0000275942	0.0000000000
64 (128)	0.0008473579	0.0005082478	0.0002708025	0.0001149092	0.0000275943	0.0000000000
128(256)	0.0008473580	0.0005082478	0.0002708025	0.0001149092	0.0000275943	0.0000000000
Analytical sol.	0.0008473579	0.0005082478	0.0002708025	0.0001149092	0.0000275943	0.0000000000

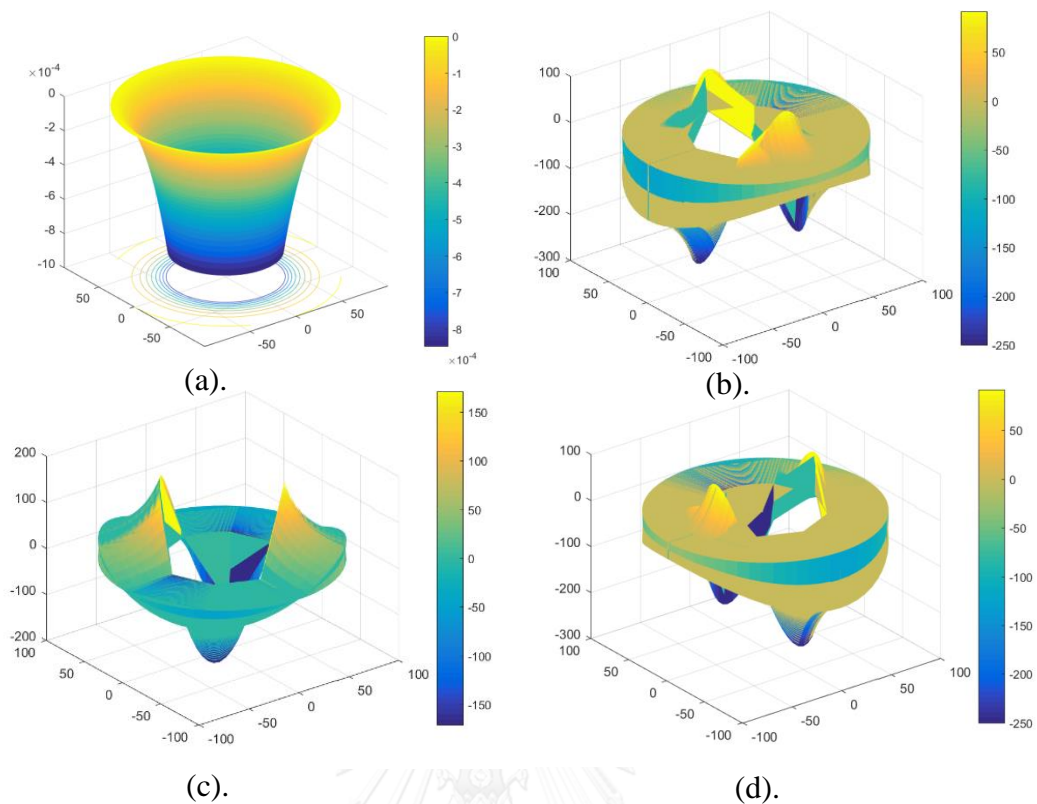


Figure 6.12: Plots of (a) deflected shape, (b) moment M_{11}^h , (c) moment M_{22}^h , and (d) moments M_{12}^h of circular plate containing concentric circular hole and subjected to uniform moments along its inner boundary obtained from mesh with 8 element.

6.1.4 Circular plate with concentric hole under applied moments

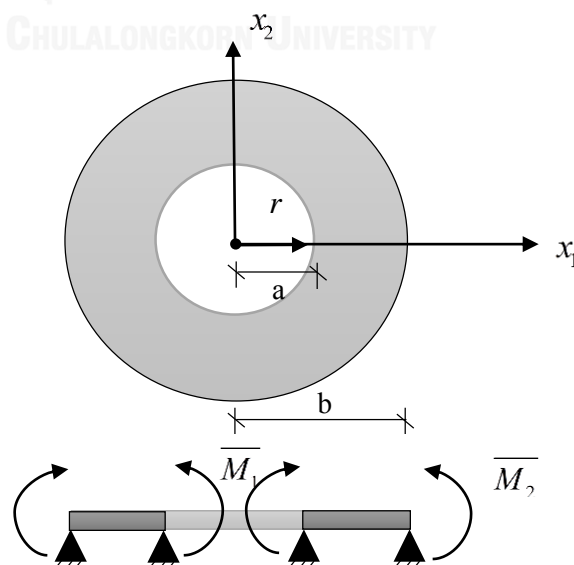


Figure 6.13: Schematic of elastic, circular plate containing concentric circular hole and subjected moments along its inner and outer boundaries.

Consider, next, an elastic, circular plate containing a concentric circular hole and simply-supported along its outer boundary as shown in Figure 6.13. The thickness t , the inner radius a , and the outer radius b of the plate are taken as $t = 5$ cm, $a = 50$ cm, and $b = 100$ cm, respectively. The plate is made of an isotropic, linearly elastic material with Young modulus $E = 200,000$ N/mm² and Poisson ratio $\nu = 0.3$ and subjected to uniformly distributed moment $\bar{M}_1 = 500$ N-cm/cm along its entire inner boundary and $\bar{M}_2 = 250$ N-cm/cm along its entire outer boundary. Again, the reference solution for the transverse displacement for this particular case is generated by using results reported by [66] and the method of superposition. In the numerical study, the scaling center and the defining curve are chosen at the center of the plate and the outer boundary, respectively, and six meshes containing 4, 8, 16, 32, 64 and 128 two-node elements are adopted as indicated in Figure 6.9.

The computed deflection for various locations along the radial direction of the plate is reported in Table 6.6 for $t/b = 0.05$. Clearly, as the number elements used in the discretization of the defining curve increases, numerical results converge rapidly to the benchmark solution. In addition, the plots of the maximum deflection versus the number of elements and the percent error of computed deflections along the x1-direction are presented in Figure 6.14 and Figure 6.15, respectively. To further demonstrate the accuracy of the computed numerical solutions, the bending moments M_{11}^h , M_{22}^h and M_{12}^h along the circumferential direction for $\xi = 0.5, 0.6, 0.7, 0.8, 0.9$ and 1 are plotted in Figure 6.16. The deflected shape of the plate and its contour plot are shown in Figure 6.17. As is evident from this set of results, the maximum deflection occur within the plate approximately $\xi = 0.75$.

Table 6.6: Deflection for circular plate containing concentric circular hole and subjected moments along its inner and outer boundaries for $t/b = 0.05$

Elem. (Dof.)	r/b					
	0.5	0.6	0.7	0.8	0.9	1
4 (8)	5.78E-11	0.00031707	0.000445178	0.000420299	0.000266301	9.66E-11
8 (16)	0.0000000000	0.0003170704	0.0004451780	0.0004202988	0.0002663012	0.0000000000
16 (32)	0.0000000000	0.0003170704	0.0004451780	0.0004202988	0.0002663012	0.0000000000
32 (64)	0.0000000000	0.0003170704	0.0004451780	0.0004202988	0.0002663011	0.0000000000
64 (128)	0.0000000000	0.0003170704	0.0004451780	0.0004202988	0.0002663012	0.0000000000
128(256)	0.0000000000	0.0003170704	0.0004451780	0.0004202988	0.0002663012	0.0000000000
Analytical sol.	0.0000000000	0.0003170704	0.0004451780	0.0004202988	0.0002663012	0.0000000000

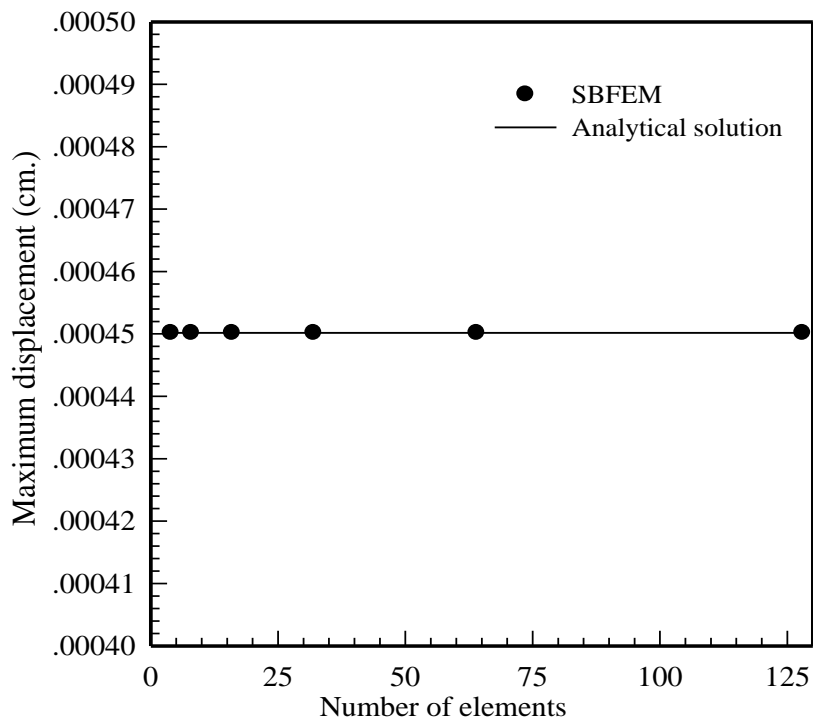


Figure 6.14 : Maximum deflection of circular plate containing concentric circular hole and subjected moments along its inner and outer boundaries versus the number of elements used in discretization of defining curve for $t/b = 0.05$

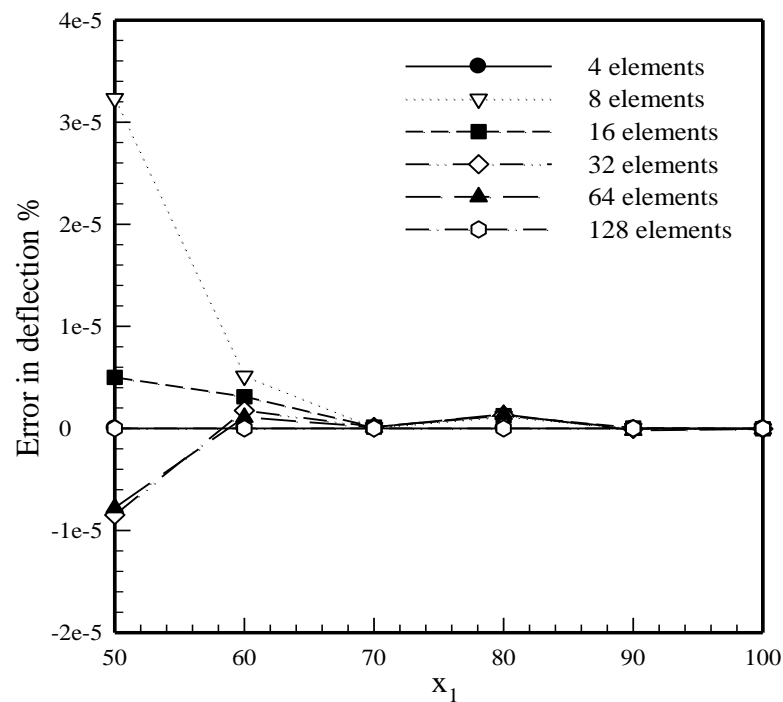


Figure 6.15: Percent error of computed deflection of circular plate containing concentric circular hole and subjected moments along its inner and outer boundaries for $t/b = 0.05$

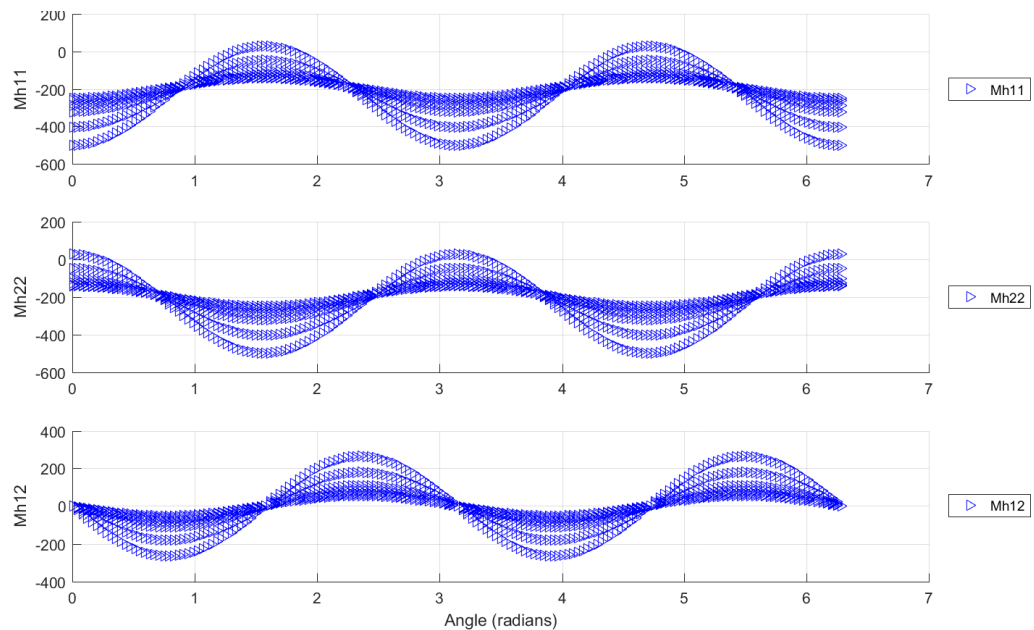


Figure 6.16: Bending moments M_{11}^h , M_{22}^h and M_{12}^h along circumferential direction of circular plate containing concentric circular hole and subjected moments along its inner and outer boundaries for $\xi=0.5, 0.6, 0.7, 0.8, 0.9$ and 1.

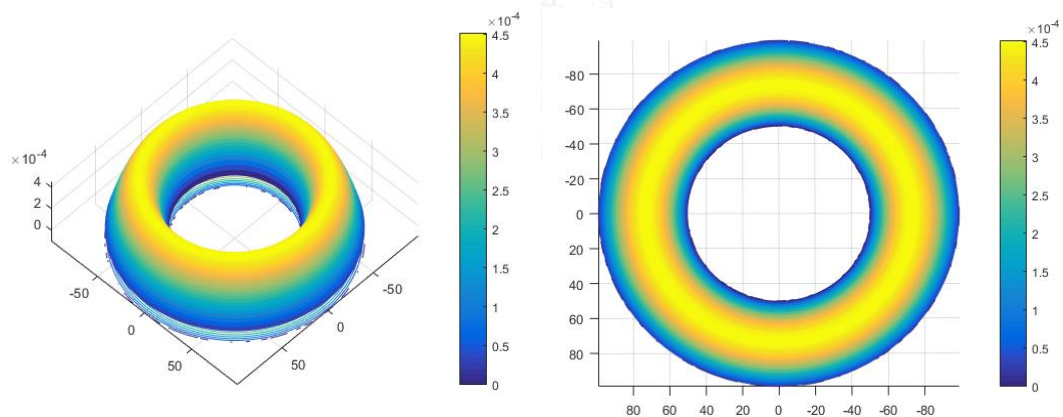


Figure 6.17: Deflected shape and contour plot of the deflection of circular plate containing concentric circular hole and subjected moments along its inner and outer boundaries obtained from mesh with 8 element and $t/b = 0.005$.

6.1.5 Trapezoidal plate under transverse shear

Consider, as the final example used in the verification process, a trapezoidal plate of thickness $t = 1$ mm and clamped along its inner boundary with all other sides free as shown schematically in Figure 6.18. The plate is made of an isotropic material with Young modulus = 210,000 N/mm² and Poisson ratio = 0.3 and loaded by a uniform transverse shear force 10 N/mm along the outer boundary.

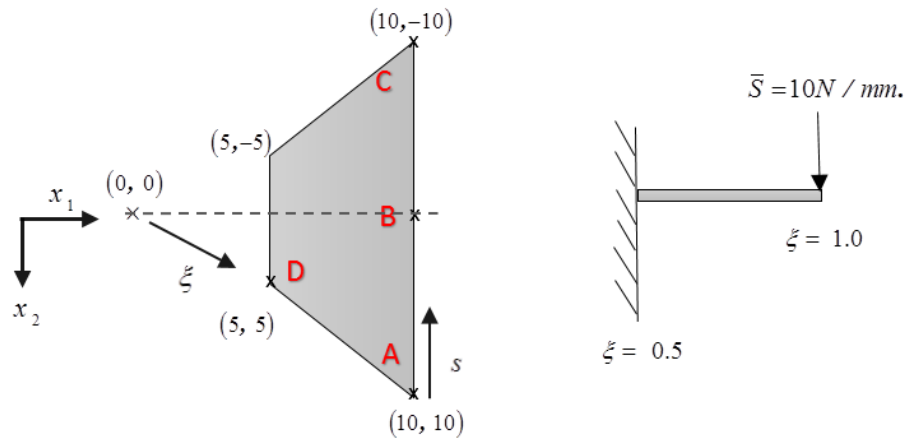


Figure 6.18: Schematic of trapezoidal plate clamped along the inner boundary and loaded by uniform transverse shear along the outer boundary.

For this particular problem, the scaling center is located outside the plate at the origin of the $x_1 - x_2$ reference coordinate system and the free outer boundary is chosen as the defining curve. Results reported by Dieringer and Becker [23] are employed as the reference solution. The spectrum of all eigenvalues obtained by solving the fourth-order eigenvalue system is reported in Figure 6.20 for the discretized plate with 10 elements along its outer boundary. It is evident that the spectrum plot is symmetric with respect to both vertical and horizontal axes and show the good agreement with that reported in [23].

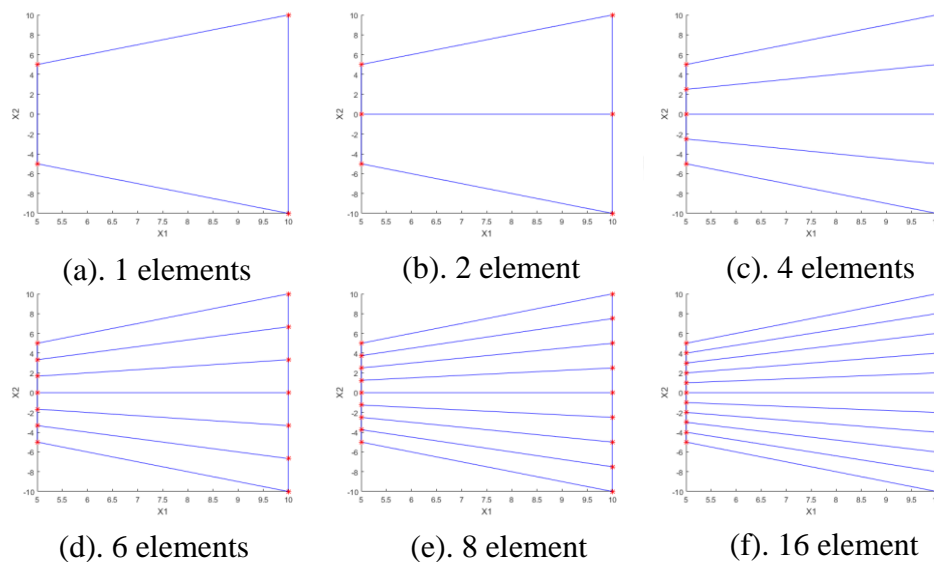


Figure 6.19: Schematic of six meshes used in discretization of defining curve of trapezoidal plate

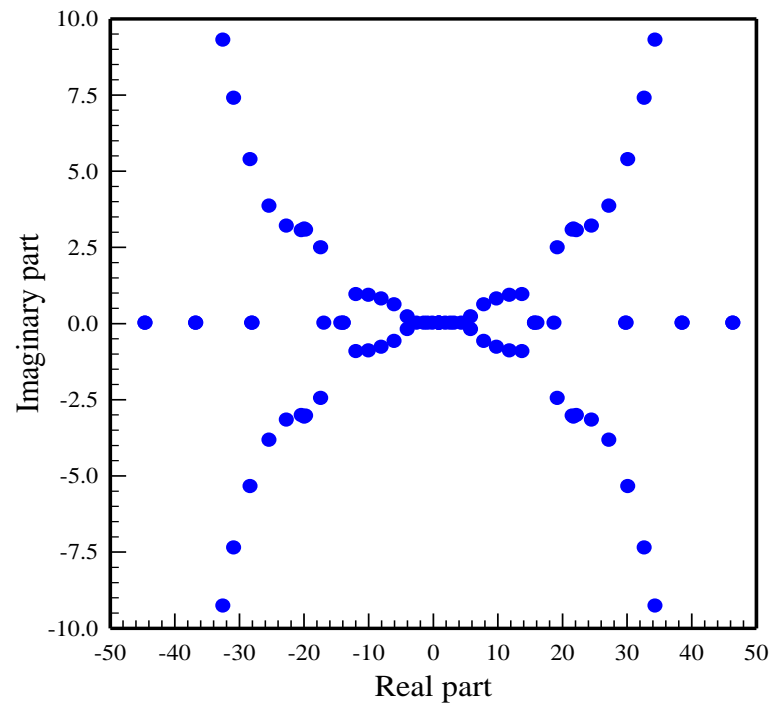


Figure 6.20: Spectrum of eigenvalues for the discretization of plate with 10 elements

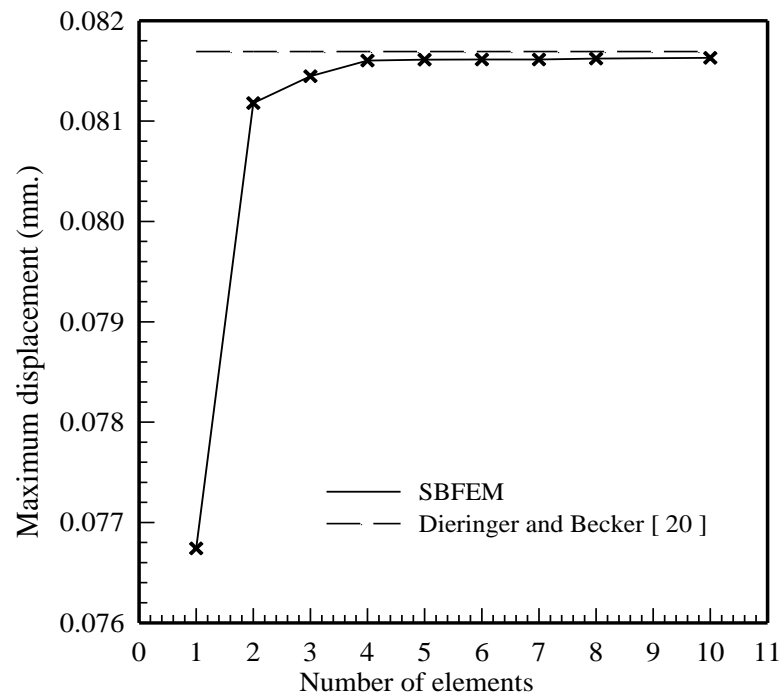


Figure 6.21: Maximum transverse displacement of trapezoidal plate versus number of elements used in discretization of defining curve.

Table 6.7: Transverse displacement at points A, B and C of trapezoidal plate (mm) loaded by uniform transverse shear force along the outer boundary.

At point	Number of elements							Ref. [20]
	1	2	4	6	8	10	20	
A	0.076742	0.081179	0.081603	0.081613	0.081620	0.081628	0.081681	0.081692
B	0.031661	0.029377	0.029929	0.030039	0.030099	0.030137	0.030225	0.030390
C	0.076742	0.081179	0.081603	0.081608	0.081620	0.081628	0.081683	0.081692

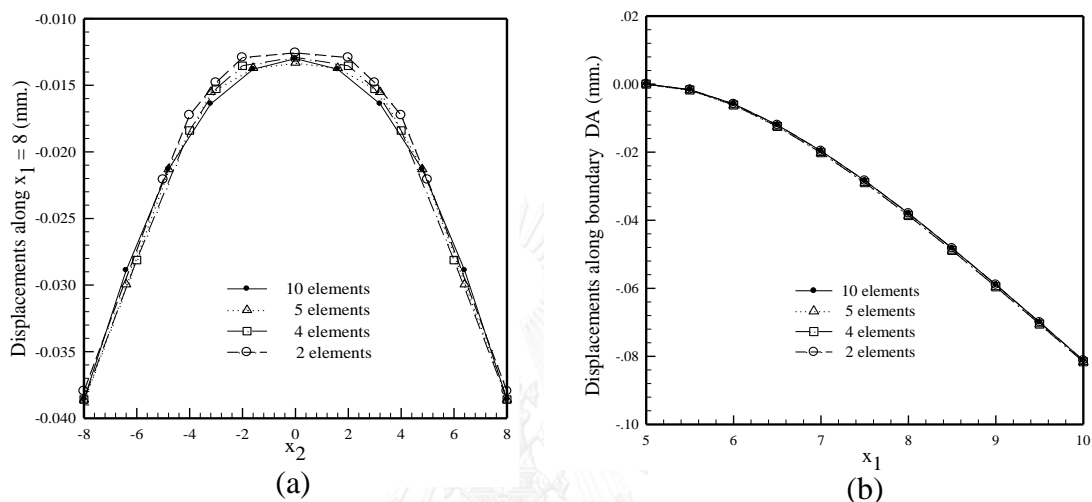


Figure 6.22: (a) Deflections along the straight line = 8 mm for different levels of discretization and (b) deflections along the radial boundary for different levels of discretization.

To demonstrate the convergence of the computed numerical solutions, the maximum deflection of the plate (occurring at the corners on the outer boundary, i.e., points A and C) is reported for different levels of discretization in Figure 6.21. It is evident from this set of results that the computed solutions converge rapidly to the reference result reported by Dieringer and Becker [23] as the number of elements in the discretization increases; the discretization with only four elements can accurately capture the solution with error less than 1 % in comparison with the reference solution. The deflections along the straight line = 8 mm and along the radial boundary are also reported for different levels of discretization in Figure 6.22, and the same convergence behavior is observed. The percent error of computed deflection at points A, B, and C (as indicated in Figure 6.18) versus the number of elements used to discretize the defining curve is also reported in Figure 6.23. These results additionally confirm the convergence of numerical solutions. In particular, the percent error of the computed deflection at point A and C are less than 0.2% and at point B is less than 1 % when the mesh with 8 elements is employed. The values of the computed deflection at points A, B and C are also reported in Table 6.7 along with the reference solutions generated by Dieringer and Becker [23]. It can be seen that the proposed SBFEM can yield very accurate deflection; the discrepancy relative to the reference solution is less than 2% and 0.9% for discretization with 4 and 10 elements, respectively. These results confirm the good convergence behavior as the mesh is refined. It should be noted also that the high quality

of the approximate solution should stem from the analytical feature of the solution along the scaling direction.

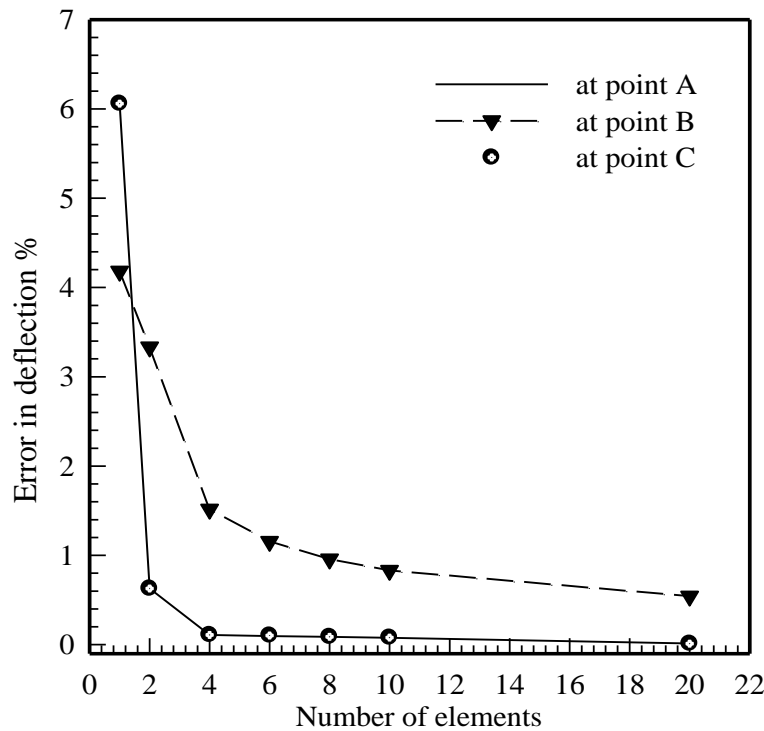


Figure 6.23: Percent error of computed deflection of trapezoidal plate clamped along the inner boundary and loaded by uniform transverse shear along the outer boundary at points A, B and C.

6.2 Results from h -hierarchical adaptive SBFEM

In the particular section, three examples are presented to demonstrate the accuracy and computational performance of the implemented h -hierarchical adaptive scaled boundary finite element method (denoted, for convenience, by ASBFEM).

6.2.1 Circular plate with concentric hole under transverse shear

Consider, again, the circular plate containing a concentric circular hole and subjected to the uniformly distributed transverse shear along its entire inner boundary as shown in Figure 6.1. In the analysis, the initial mesh containing four elements which is the same as that indicated in Figure 6.2 and the target allowable error in the energy norm $\eta^* = 0.001\%$ are employed. The energy norm of the analytical moment obtained from [66] can be also computed using equation (5.7) and denoted by $\|\mathbf{M}\|_A$. Intermediate meshes resulting from the ASBFEM are reported in Figure 6.24 along with the corresponding maximum error in each element, denoted by η_m^* . It is evident that five analysis steps are required to achieve the target error and the final mesh contains 64 elements of equal size. The obtained final uniform mesh is anticipated since the

problem data is axisymmetric. The plots of energy norms of the recovered moment for all five analysis steps of ASBFEM and the analytical moment $\|\mathbf{M}\|_A$ are also shown in Figure 6.25. It is evident that as the analysis progresses, the energy norm of the recovered moment converges to the benchmark solution and this additionally confirm the validity of the proposed scheme. The total error estimate $\bar{\eta}^*$ computed from (5.1) versus the computational time associated with the SBFEM with the uniform refinement scheme (denoted, here and in what follows, by USBFEM) and the ASBFEM is reported in Figure 6.26. It can be seen that numerical results generated by the proposed technique obtained from the final mesh are in good agreement with the analytical solutions. It is worth noting that the improvement of computational efficiency from using the ASBFEM is insignificant for this particular case since there is no variation of the solution in the circumferential direction. Converged bending moments along the circumferential direction at $\xi = 1$ (along the defining curve) is also shown in Figure 6.27. As can be seen from these results, the bending moments are smooth along the discretized direction.

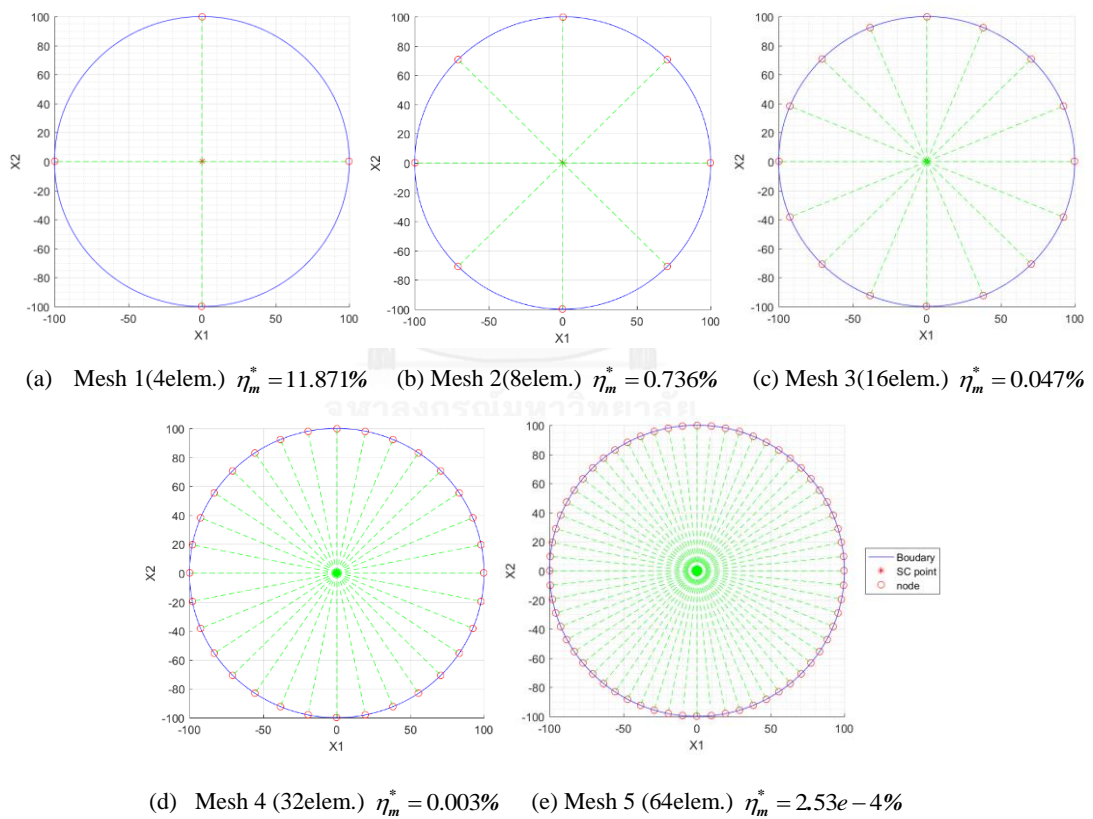


Figure 6.24: Sequence of meshes resulting from the analysis by ASBFEM for target error $\eta^* = 0.001\%$.

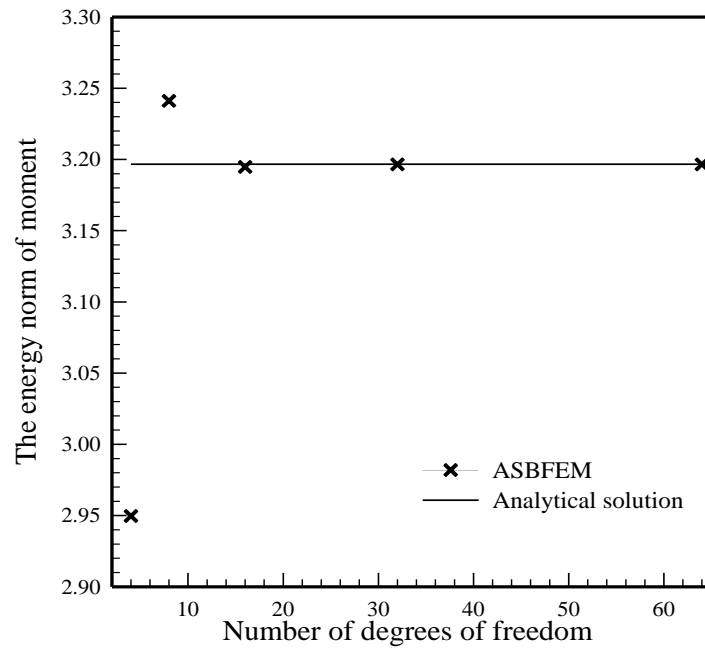


Figure 6.25: The energy norms of recovered moment and analytical moment obtained from [63].

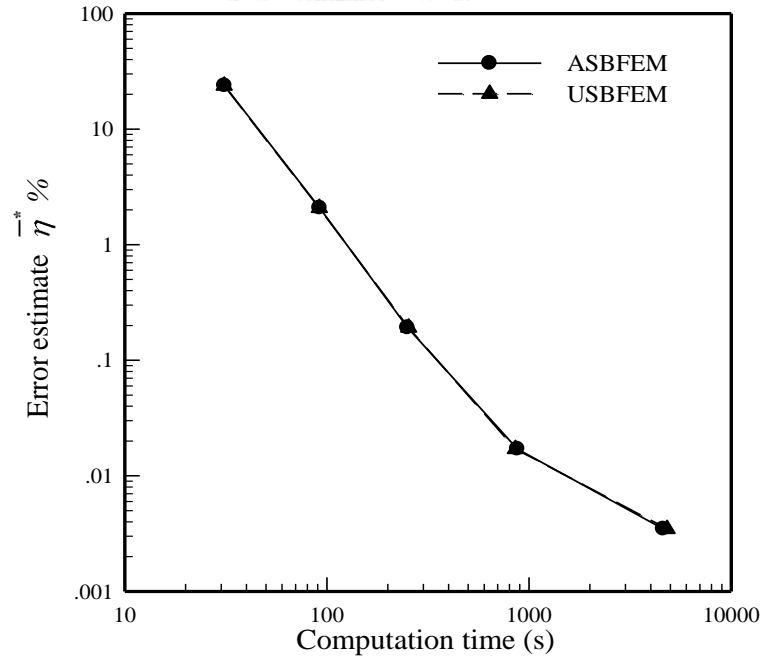


Figure 6.26: Relationship between total error estimate $\bar{\eta}^*$ and the computational time using USBFEM and ASBFEM.

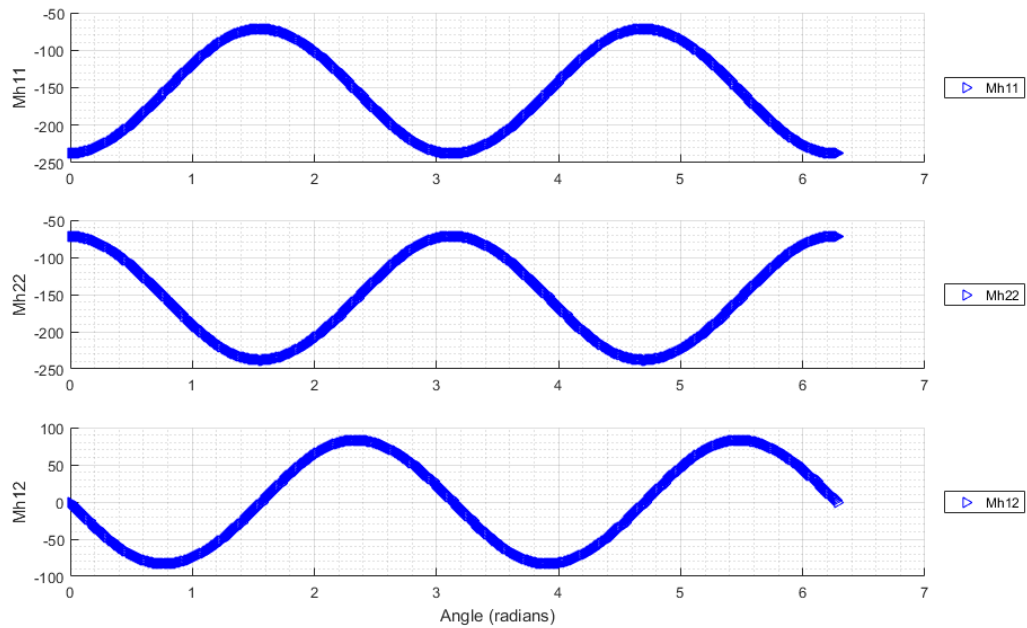


Figure 6.27: Bending moment along circumferential direction at $\xi = 1$ of circular plate with concentric circular hole loaded by transverse shear along its entire inner boundary.

6.2.2 Circular plate with concentric hole under partially loaded transverse shear

Consider, next, a circular elastic plate containing a concentric circular hole as shown schematically in Figure 6.28. The thickness t , the outer radius b and the inner radius a of the plate are chosen such that $t = 0.5$ cm, $b = 100$ cm, and $a = 50$ cm, respectively, and Young modulus and Poisson ratio of the constituting material are given by $E = 200,000$ N/mm² and $\nu = 0.3$. The plate is fully fixed against the movement along the entire outer boundary whereas its inner boundary is subjected to a uniform transverse shear load $\bar{V} = 175$ N/cm along $-\pi/6 \leq \theta \leq \pi/6$ where θ denotes the angle measured relative to the x_1 -axis. Again, the center of the plate and its outer boundary are taken as the scaling center and the defining curve in the analysis, respectively.

Results for the maximum computed deflection obtained from the ASBFEM with USBFEM are reported in Table 6.8. These results indicate that use of ASBFEM can significantly reduce the computational time and number of degrees of freedom to achieve the same level of accuracy in comparison with the USBFEM. Meshes resulting from the sequence of analysis steps required in the ASBFEM to achieve the target error $\eta^* = 1\%$ of the energy norm of the moment error are illustrated in Figure 6.29. The bending moments obtained from the final mesh of the ASBFEM with $\eta^* = 1\%$ are smooth in the circumferential direction as can be seen in Figure 6.30. It is apparent from the sequence of refinements that the discretization is concentrated in the region where the load applied. The total error estimate of computed moments $\bar{\eta}^*$ versus the number of degrees of freedom and the computational time is reported in Figure 6.31 and Figure 6.32, respectively for both USBFEM and ASBFEM. As can be seen from these results, the ASBFEM yields the higher rate of convergence and requires less computational

time to achieve the same level of accuracy in comparison with the USBFEM. The deflected shape of the plate and the contour plot of the transverse deflection obtained from the final mesh for the target error $\eta^* = 1\%$ are also shown in Figure 6.33.

Table 6.8: Comparison of computational performance of USBFEM and ASBFEM for circular plate with concentric hole under partially loaded transverse shear

Refine mesh	Dof.	computation time (sec.)	The target error $\eta^* \%$	iteration	Max. disp (cm.)
USBFEM	80	1498	5.00	4	4.222552
ASBFEM	22	195		3	4.694672
USBFEM	160	3102	1.00	5	5.840132
ASBFEM	46	730		5	5.727749
USBFEM	320	4545	0.10	6	5.846216
ASBFEM	122	1725		7	5.841390

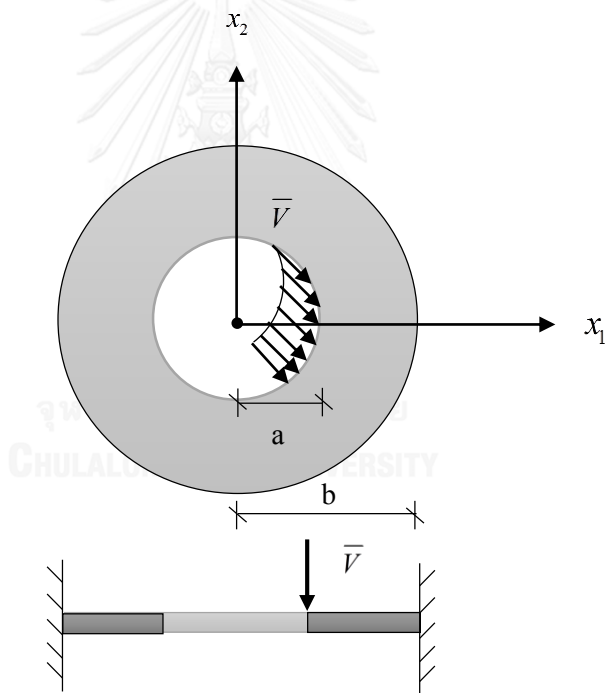


Figure 6.28: Schematic of circular plate containing concentric hole, clamped at its outer boundary and subjected to transverse shear along $-\pi/6$ to $\pi/6$

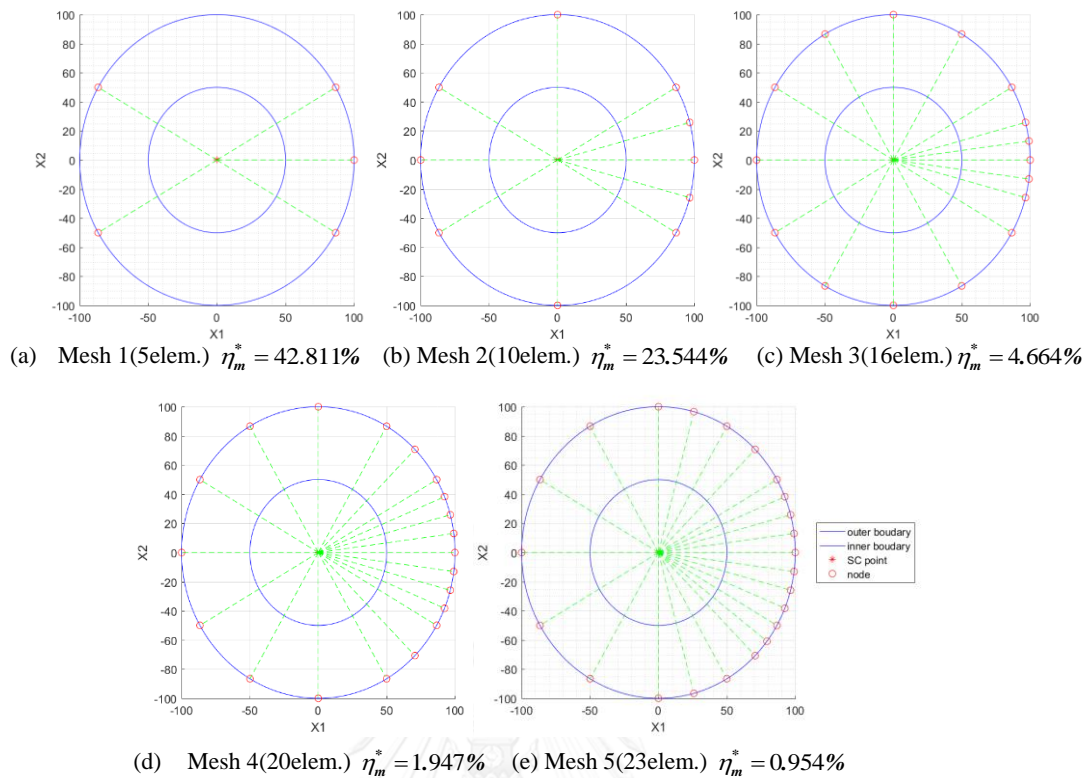


Figure 6.29: Sequence of meshes resulting from the analysis by ASBFEM for target error $\eta^* = 1\%$.

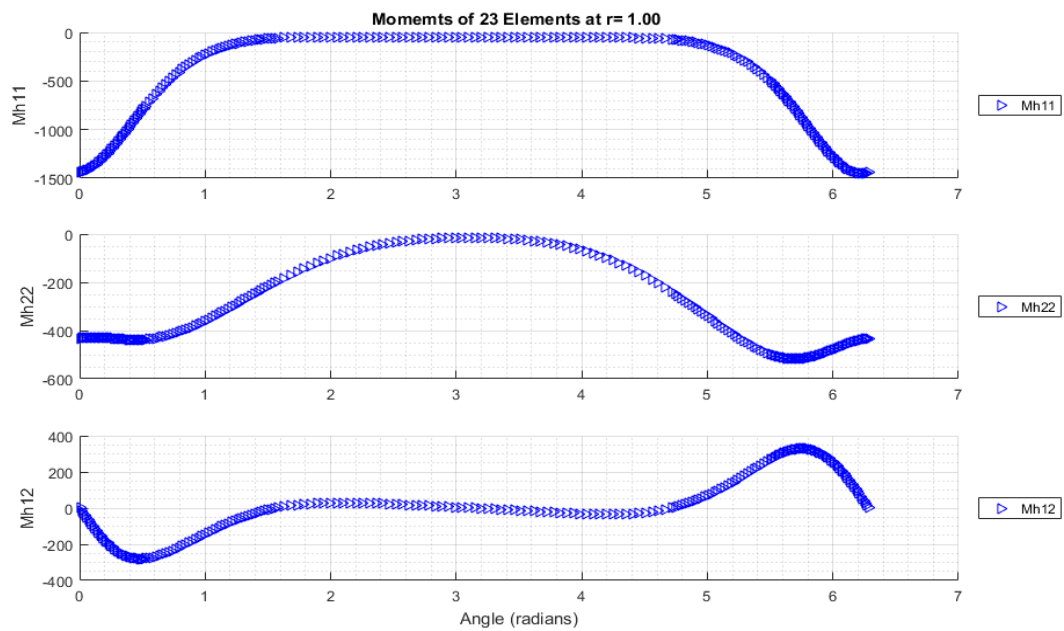


Figure 6.30: Bending moment along circumferential direction at the defining curve after adaptive process to target error.

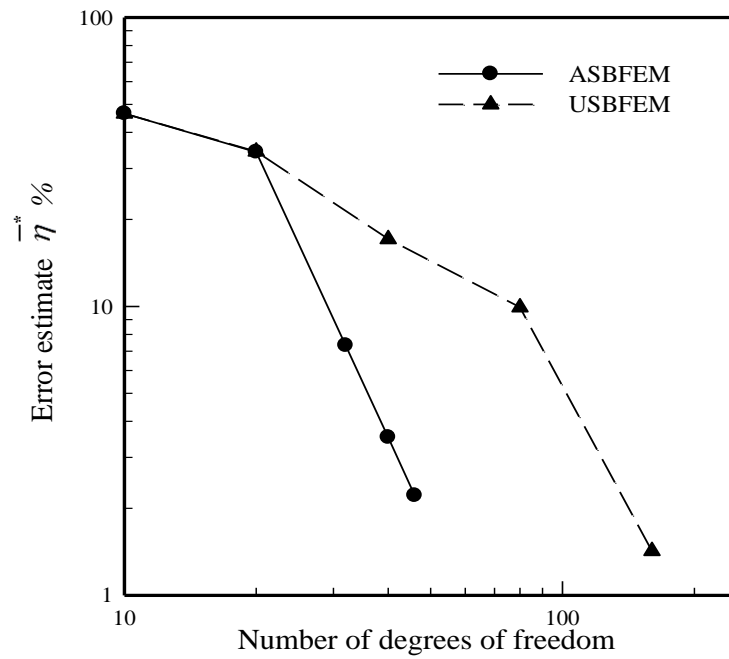


Figure 6.31: Relationship between total error estimate of computed moment and the number of degrees of freedom using USBFEM and ASBFEM.

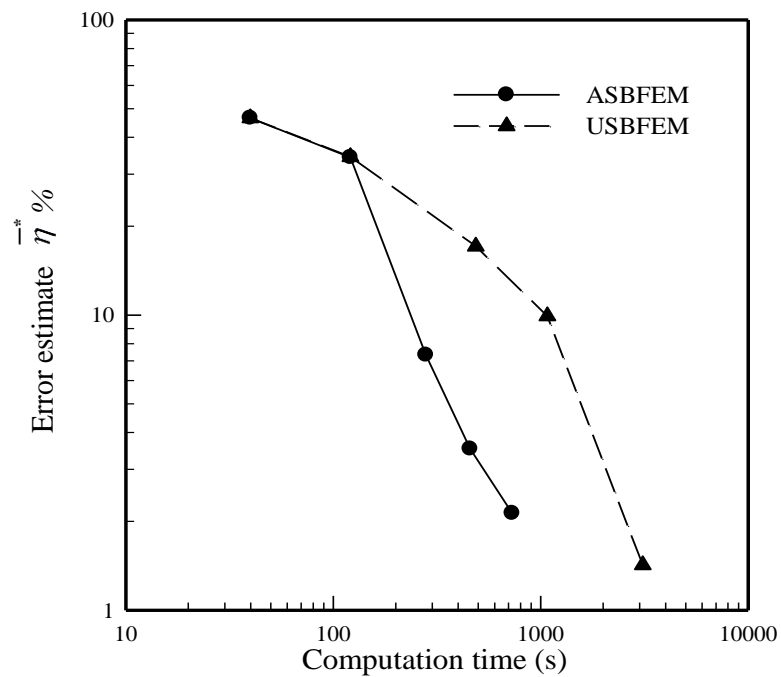


Figure 6.32: Relationship between total error estimate of computed moment and the computational time using USBFEM and ASBFEM.

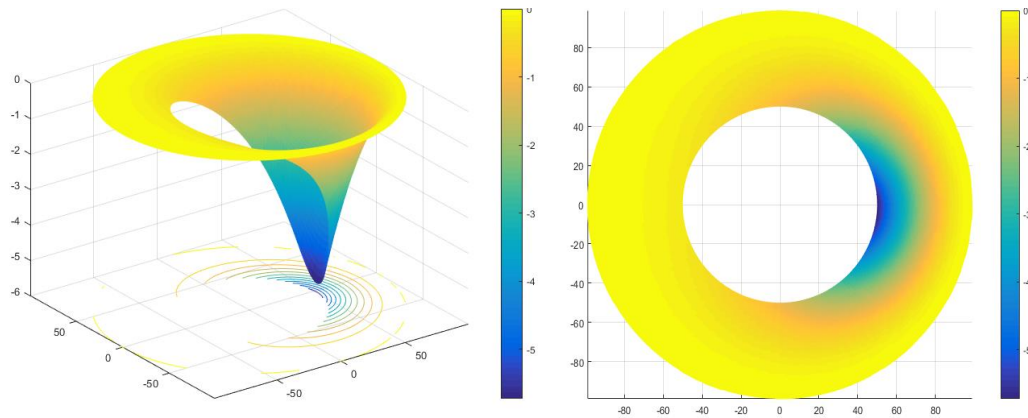


Figure 6.33: Deflected shape and contour plot of transverse deflection for circular plate containing concentric circular hole, clamped at its outer boundary and subjected to partial transverse shear obtained from final mesh for target error $\eta^* = 1\%$.

6.2.3 Semi-circular plate subjected to sinusoidal transverse shear

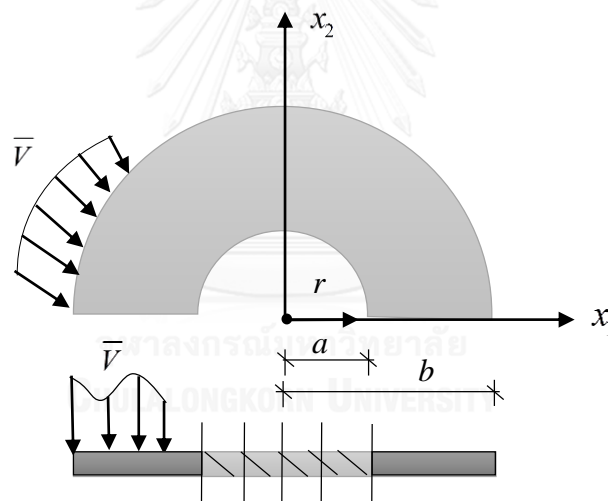


Figure 6.34: Schematic of semi-circular plate containing concentric semi-circular hole, clamped at its inner boundary and subjected to sinusoidal transverse shear at the outer boundary along $5\pi/6 \leq \theta \leq \pi$.

Consider, as a final example, a semi-circular plate containing a concentric semi-circular hole as shown schematically in Figure 6.28. The thickness t , the outer radius b and the inner radius a of the plate are chosen such that $t = 2$ cm, $b = 100$ cm, and $a = 30$ cm, respectively, and Young modulus and Poisson ratio of the constituting material are given by $E = 200,000$ N/mm² and $\nu = 0.3$. The plate is fully fixed against the movement along the entire inner boundary whereas its outer boundary is subjected to a sinusoidal transverse shear load $\bar{V} = 45 [2 + \sin(2\theta^2)]$ N/cm for $5\pi/6 \leq \theta \leq \pi$ where θ denotes the angle measured relative to the x_1 -axis. Again, the center of the plate and its outer

boundary are taken as the scaling center and the defining curve in the analysis, respectively.

In the analysis, the initial mesh containing two elements as indicated in Figure 6.35(a) is employed. The computational performance of the proposed technique is investigated, again, by comparing results with those of the USBFEM. Meshes resulting from the analysis by the ASBFEM with the target error $\eta^* = 1\%$ are illustrated in Figure 6.35. The relationship between the total error estimate and the number of degrees of freedom and the computational time using both USBFEM and ASBFEM is illustrated in Figure 6.36 and Figure 6.37, respectively. This set of results additionally confirms the advantage gained by using the ASBFEM. The final mesh obtained adaptively to achieve the specified target error contains only 32 degrees of freedom, while a uniform mesh with the same number of degrees of freedom achieves total error of 4.62%. It is evident, from results in Figure 6.38 and Figure 6.38, that rate of decreasing in the error estimate, for the ASBFEM, increases as the number of degrees of freedom used in the approximation the computational time consumed increases. The deflected shape and contour plot of the transverse deflection of the plate obtained from the final mesh with the target error are reported in Figure 6.38.

Table 6.9: Comparison of computational performance of USBFEM and ASBFEM for semi-circular plate with concentric semi-circular hole under sinusoidal transverse shear

Refine mesh	Dof.	computation time (sec.)	The target error $\eta^* \%$	iteration	Max. disp (cm.)
USBFEM	18	234	5.00	3	0.549631
ASBFEM	14	125		4	0.551464
USBFEM	66	1636	1.00	5	0.547434
ASBFEM	32	724		9	0.542825
USBFEM	130	2686	0.10	6	0.542434
ASBFEM	58	1064		6	0.542729

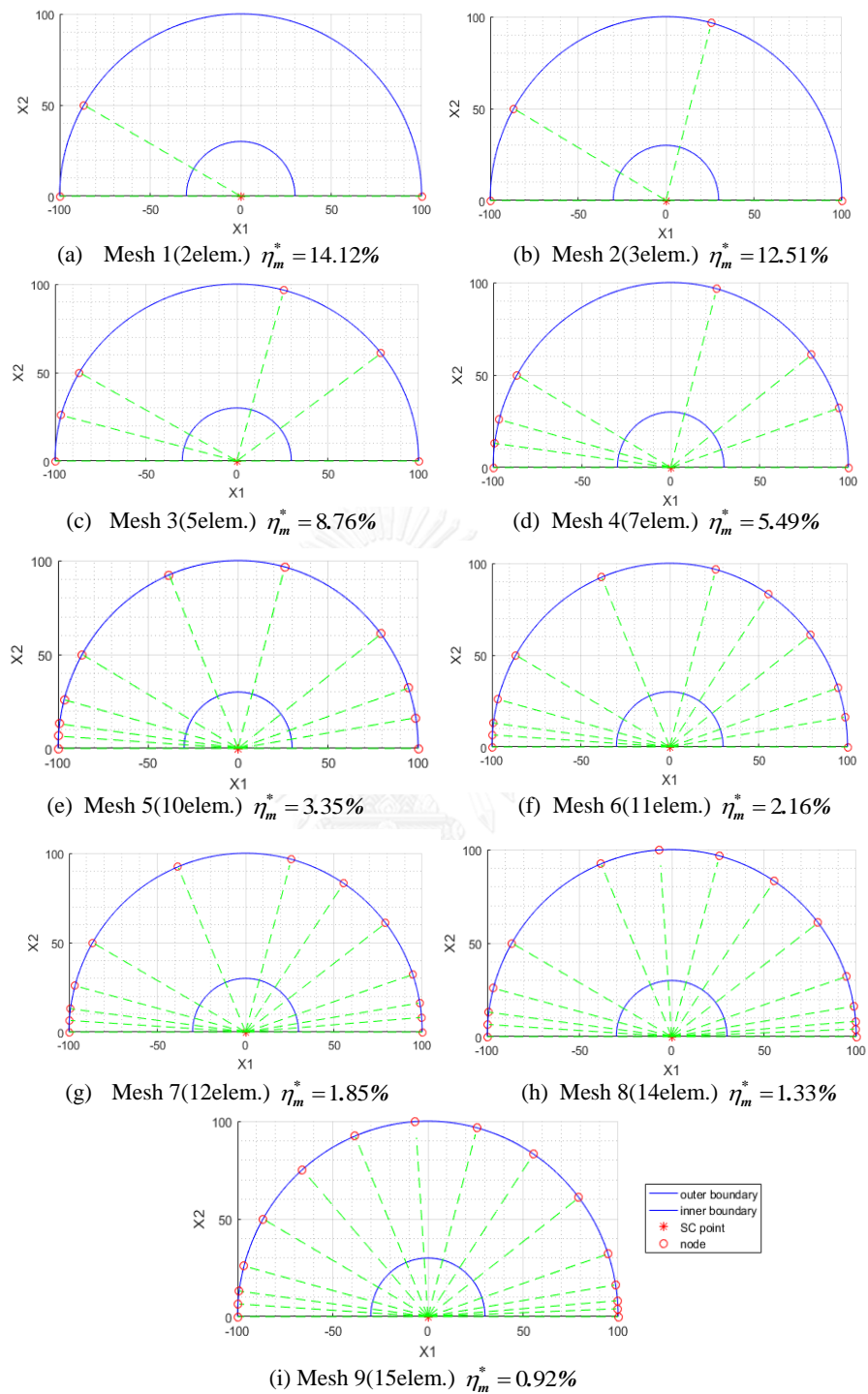


Figure 6.35 : Sequence of meshes resulting from the analysis by ASBFEM for target error $\eta^* = 1\%$.

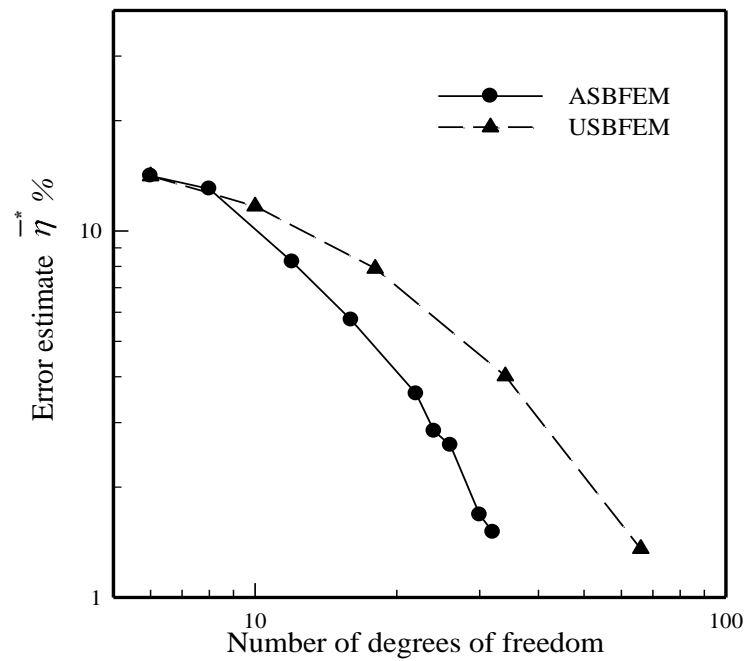


Figure 6.36: Relationship between total error estimate of computed moment and the number of degrees of freedom using USBFEM and ASBFEM.

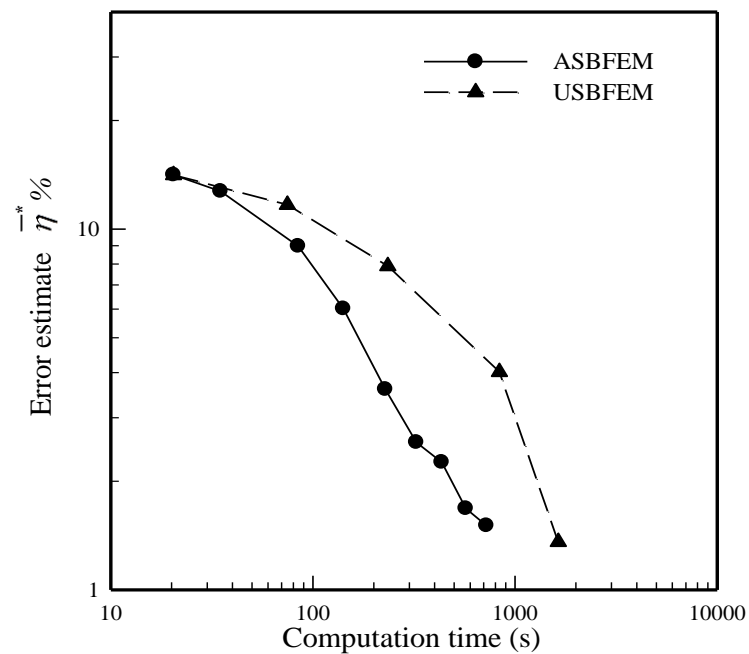


Figure 6.37: Relationship between total error estimate of computed moment and the computational time using USBFEM and ASBFEM.

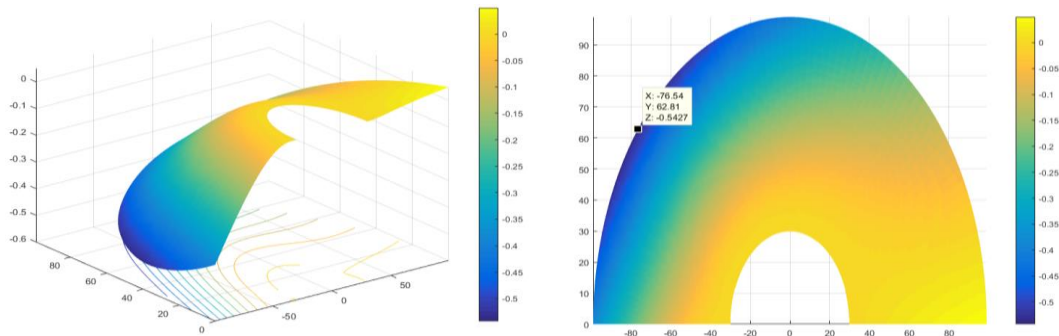


Figure 6.38: Deflected shape and contour plot of transverse deflection for semi-circular plate containing concentric semi-circular hole, clamped at its inner boundary and subjected to sinusoidal transverse shear obtained from final mesh for target error $\eta^* = 1\%$.

6.2.4 Trapezoidal plate under partially loaded transverse shear

Consider, as the final example, a trapezoidal plate of thickness $t = 1$ cm and clamped along a shorter paralleled side as clearly indicated in Figure 6.39. The plate is made of an isotropic material with Young modulus $E = 210,000$ N/mm² and Poisson ratio $\nu = 0.3$ and loaded by a linearly distributed transverse force $\bar{S} = 10x_2$ N/cm, $x_2 \in [0, -10$ cm] along a longer paralleled side.

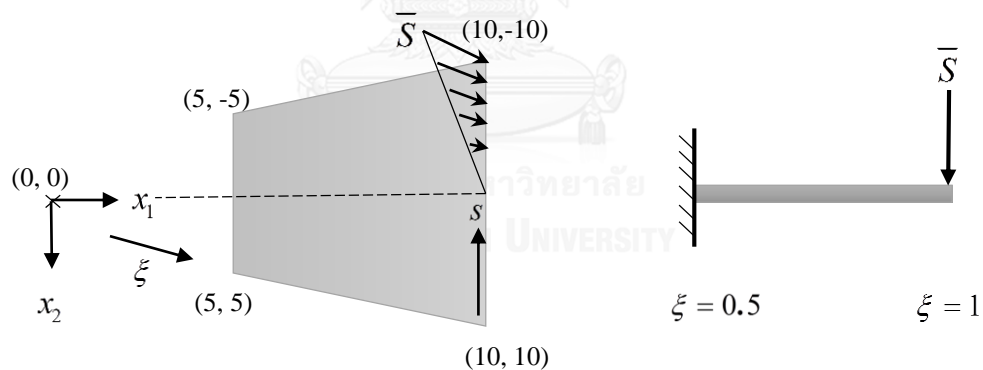


Figure 6.39: Schematic of trapezoidal plate clamped along shorter paralleled side and subjected to linearly distributed transverse shear along longer paralleled side.

To describe the geometry of the plate, the scaling center is located outside the plate at the origin of the $x_1 - x_2$ reference coordinate system (see Figure 6.39) and the free outer boundary is chosen as the defining curve. In the analysis, the initial mesh containing only two elements as indicated in Figure 6.40(a) is employed. The computational performance of the proposed technique is investigated, again, by comparing obtained results with those of the USBFEM. Meshes resulting from the analysis steps of the ASBFEM with the target error $\eta^* = 0.1\%$ is shown in Figure 6.40. The relationship between the total error estimate versus the number of degrees of freedom used in the

approximation and the computational time consumed for both USBFEM and ASBFEM is illustrated in Figure 6.41 and Figure 6.42, respectively. This set of results additionally confirms the computational advantage of using the ASBFEM. The final mesh obtained adaptively to achieve the specified target error $\eta^* = 0.1\%$ contains only 26 degrees of freedom, while a uniform mesh with about the same number of degrees of freedom achieves only total error of 2.01%. The deflected shape and the contour plot of the transverse deflection of the plate obtained from the final mesh with the target error $\eta^* = 0.1\%$ are also reported in Figure 6.43.

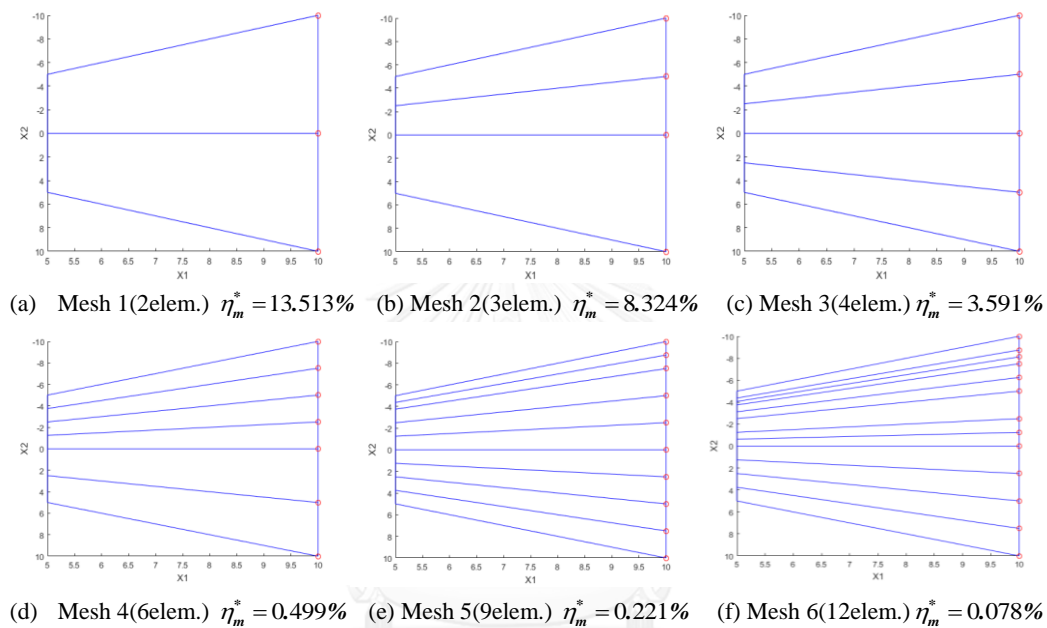


Figure 6.40: Sequence of meshes resulting from the analysis by ASBFEM for target error $\eta^* = 0.1\%$.

Table 6.10: Comparison of computational performance of USBFEM and ASBFEM for trapezoidal plate clamped along shorter paralleled side and subjected to linearly distributed transverse shear along longer paralleled side

Refine mesh	Dof.	computation time (sec.)	The target error $\eta^* \%$	iteration	Max. disp (cm.)
USBFEM	18	23	5	3	0.049738708
ASBFEM	10	11		3	0.046612868
USBFEM	34	83	1	4	0.045199153
ASBFEM	14	18		4	0.045152133
USBFEM	66	499	0.1	5	0.042808039
ASBFEM	26	59		6	0.042853386

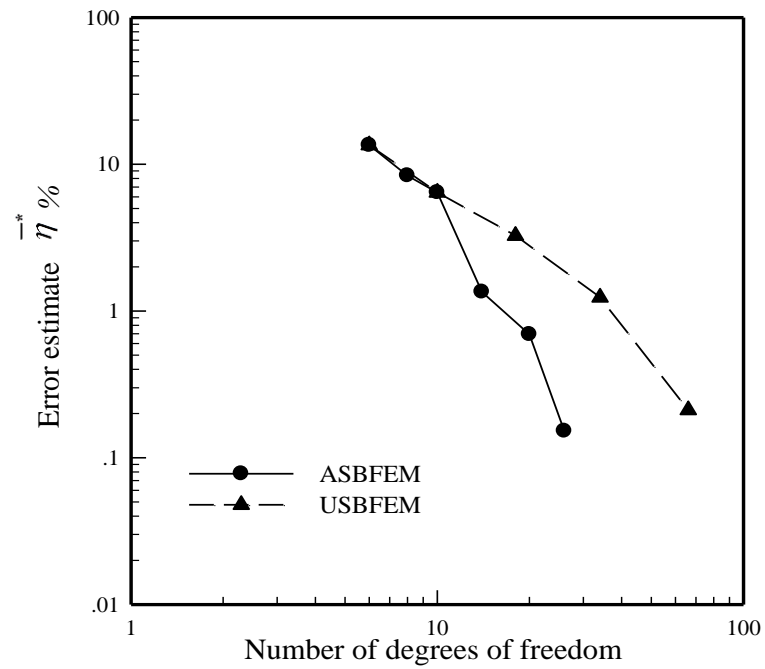


Figure 6.41: Relationship between total error estimate of computed moment and the number of degrees of freedom using USBFEM and ASBFEM.

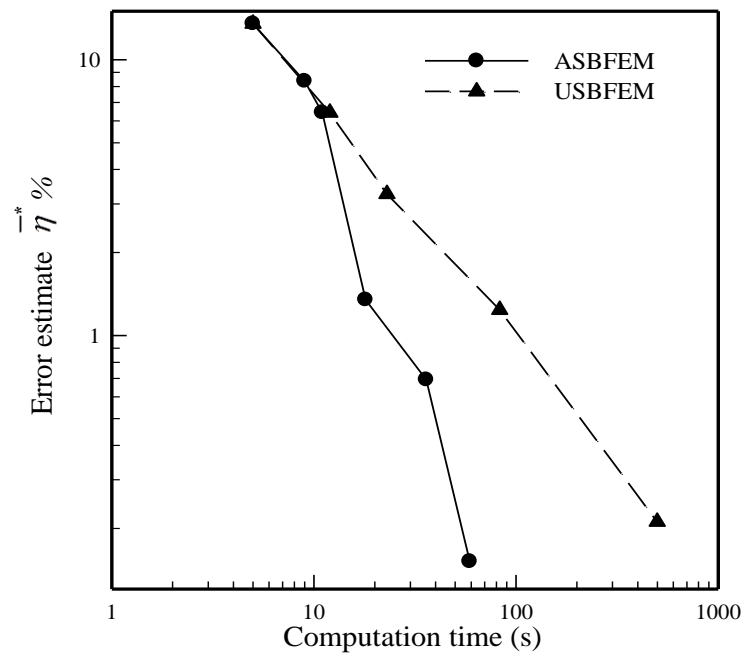


Figure 6.42: Relationship between total error estimate of computed moment and the computational time using USBFEM and ASBFEM.

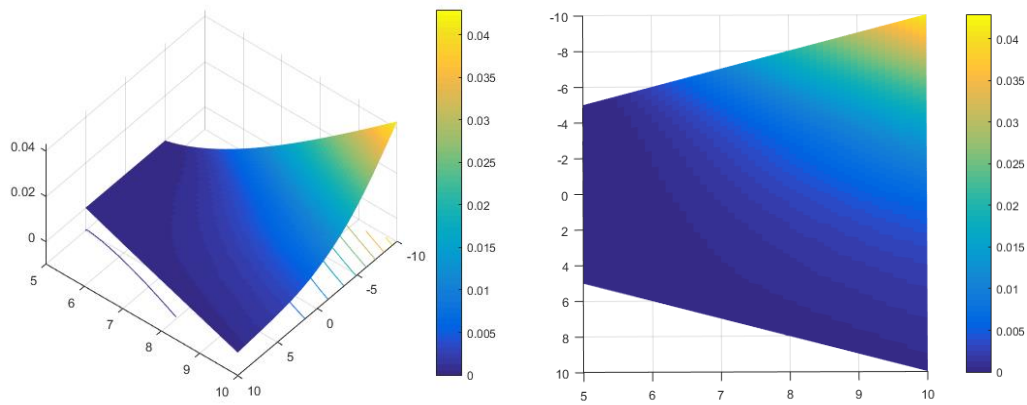


Figure 6.43: Deflected shape and contour plot of transverse deflection for trapezoidal plate clamped along shorter paralleled side and subjected to linearly distributed transverse shear along longer paralleled side obtained from final mesh for target error $\eta^* = 0.1\%$.



CHAPTER 7

CONCLUSIONS AND REMARKS

The efficient computational procedure, based upon the scaled boundary finite element method (SBFEM) and the h -hierarchical adaptive scheme, has been established to solve plate bending problems. In the formulation, the Kirchhoff's plate theory has been adopted along with the standard weighted residual technique and the scaled boundary approximation to form a complete set of scaled boundary finite element equations. The resulting system of linear, non-homogeneous, fourth-order ordinary Euler-Cauchy differential equations has been successfully solved using conventional techniques such as the solution representations and method of undetermined coefficients to obtain the general solution. The involved fourth-order Eigen problem has been solved by an efficient Eigen search algorithm to obtain all Eigen pairs. The prescribed conditions on the boundary of the plate have been enforced to establish a system of linear algebraic equations governing all unknowns on the domain boundary. Other field quantities of interest have been readily post-processed from the general solution of the transverse displacement of the plate. An extensive numerical study on various scenarios has indicated that the proposed technique can yield highly accurate numerical solutions even when relatively coarse meshes with few degrees of freedom are employed to discretize solutions along the scaled boundary direction and, in addition, the good convergence behavior is observed as the mesh is refined. To further enhance the computational efficiency and corresponding cost, the h -hierarchical adaptivity has been integrated into the scaled boundary finite element method to automatically obtain an adequate and optimal level of refinement within the specified error tolerance. The smoothing process via the least square technique has been adopted to obtain the reference solution for the internal bending moment used in the error estimation for each analysis step. The implemented adaptive procedure has led to the significant improvement in the computational time over the use of uniform meshes.

Results obtained from the analysis of several examples have indicated that the h -hierarchical adaptive procedure implemented in the scaled boundary finite element method for solving Kirchhoff's plate bending problems can significantly reduce the number of degrees of freedom and the computational time in comparison with that using the uniform mesh. This significant improvement becomes more apparent when problems possessing significant spatial variation of the solution are considered. In particular, the proposed technique has been found able to reduce the computational time by approximately 40 percent of that spent by the SBFEM with uniform meshes. Using the h -hierarchical adaptivity has automatically identified regions requiring the mesh refinement and finally led to the level of discretization that is commonly termed optimal. While the h -hierarchical adaptive SBFEM has been successfully established, its development is still restricted to certain settings. Extension of the present work to treat corner effects, multiple scaling centers, and non-zero prescribed data on the side-face is considered essential since it can further enhance the capability of the technique to model more general plate bending problems.

REFERENCES

- [1]. *A reinforced concrete building with flat plate system under construction, Kenya (K. Jaiswal)*. [Online] GEM NEXUS: Available from: <https://www.nexus.globalquakemodel.org/gem-building-taxonomy/overview/glossary/flat-slab-plate-or-waffle-slab--lfls> [2015,4 July].
- [2]. *The Sampoong Department Store collapse* [Online] Available from: <http://jsy2125.tistory.com/32> [2015, 12 April]: National Geographic South Korea.
- [3]. Charles, G.S. and E.J. John, *Steel Structures Design and Behavior*. Fourth edition ed. 1996, University of Wisconsin-Madison: HarperCollins College Publishers, . p.327-358.
- [4]. Levinson, M., *The simply supported rectangular plate: An exact, three dimensional, linear elasticity solution*. Journal of Elasticity, 1985. **15**(3): p. 283-291.
- [5]. Reddy, J.N., *Theory and analysis of elastic plates and shells*. 2006: CRC press.
- [6]. Batista, M., *New analytical solution for bending problem of uniformly loaded rectangular plate supported on corner points*. The IES Journal Part A: Civil & Structural Engineering, 2010. **3**(2): p. 75-84.
- [7]. Zienkiewicz, O.C. and R.L. Taylor, *The finite element method*. Vol. 3. 1977: McGraw-hill London.
- [8]. Swenson, D. and A. Ingraffea, *Modeling mixed-mode dynamic crack propagation using finite elements: theory and applications*. Computational Mechanics, 1988. **3**(6): p. 381-397.
- [9]. Yang, Z., J. Chen, and D. Proverbs, *Finite element modelling of concrete cover separation failure in FRP plated RC beams*. Construction and Building Materials, 2003. **17**(1): p. 3-13.
- [10]. Dasgupta, G., *A finite element formulation for unbounded homogeneous continua*. Journal of Applied Mechanics, 1982. **49**(1): p. 136-140.
- [11]. Rybicki, E.F. and M. Kanninen, *A finite element calculation of stress intensity factors by a modified crack closure integral*. Engineering Fracture Mechanics, 1977. **9**(4): p. 931-938.
- [12]. White, W., I.K. Lee, and S. Valliappan, *Unified boundary for finite dynamic models*. Journal of the Engineering Mechanics Division, 1977. **103**(5): p. 949-964.
- [13]. Brebbia, C.A. and J. Dominguez, *Boundary elements: an introductory course*. 1996: WIT press.
- [14]. Brebbia, C.A. and D.J. Danson, *The Boundary Element Technique for the Analysis of Automotive Structures*. 1984, SAE Technical Paper.
- [15]. Song, C. and J.P. Wolf, *The scaled boundary finite-element method—alias consistent infinitesimal finite-element cell method—for elastodynamics*. Computer Methods in applied mechanics and engineering, 1997. **147**(3): p. 329-355.
- [16]. Wolf, J.P. and C. Song, *The scaled boundary finite-element method—a primer: derivations*. Computers & Structures, 2000. **78**(1): p. 191-210.

- [17]. Liu, J. and G. Lin, *A scaled boundary finite element method applied to electrostatic problems*. Engineering Analysis with Boundary Elements, 2012. **36**(12): p. 1721-1732.
- [18]. Yang, Z. and A. Deeks, *A frequency-domain approach for modelling transient elastodynamics using scaled boundary finite element method*. Computational Mechanics, 2007. **40**(4): p. 725-738.
- [19]. Man, H., et al., *Semi-analytical analysis for piezoelectric plate using the scaled boundary finite-element method*. Computers & Structures, 2014. **137**: p. 47-62.
- [20]. Yang, Z. and A. Deeks, *Fully-automatic modelling of cohesive crack growth using a finite element–scaled boundary finite element coupled method*. Engineering fracture mechanics, 2007. **74**(16): p. 2547-2573.
- [21]. Song, C., *A matrix function solution for the scaled boundary finite-element equation in statics*. Computer Methods in Applied Mechanics and Engineering, 2004. **193**(23): p. 2325-2356.
- [22]. Man, H., et al., *A unified 3D-based technique for plate bending analysis using scaled boundary finite element method*. International Journal for Numerical Methods in Engineering, 2012. **91**(5): p. 491-515.
- [23]. Dieringer R, H.R., Becker W, *The scaled boundary finite element method for plate bending problems*. CMM-2011 – Computer Methods in Mechanics, May 2011. **PaperID: 50**: p. 169–170.
- [24]. Hebel, J. and W. Becker, *Analysis of thin laminated plates by means of the scaled boundary finite element method*. PAMM, 2008. **8**(1): p. 10285-10286.
- [25]. Tsach, U., *Locking of thin plate/shell elements*. International Journal for Numerical Methods in Engineering, 1981. **17**(4): p. 633-644.
- [26]. Zrahia, U. and P. Bar-Yoseph, *Plate spectral elements based upon Reissner–Mindlin theory*. International journal for numerical methods in engineering, 1995. **38**(8): p. 1341-1360.
- [27]. Xenophontos, C., J. Kurtz, and S. Fulton, *A p-version MITC finite element method for Reissner–Mindlin plates with curved boundaries*. Journal of computational and applied mathematics, 2006. **192**(2): p. 374-395.
- [28]. Chowdhury, M.S., C. Song, and W. Gao, *Probabilistic fracture mechanics by using Monte Carlo simulation and the scaled boundary finite element method*. Engineering Fracture Mechanics, 2011. **78**(12): p. 2369-2389.
- [29]. Li, C., et al., *Fracture analysis of piezoelectric materials using the scaled boundary finite element method*. Engineering Fracture Mechanics, 2013. **97**: p. 52-71.
- [30]. Wolf, J.P., *The scaled boundary finite element method*. 2003: John Wiley & Sons.
- [31]. Deeks, A.J. and J.P. Wolf, *Stress recovery and error estimation for the scaled boundary finite-element method*. International journal for numerical methods in engineering, 2002. **54**(4): p. 557-583.
- [32]. Euler, L., *De motu vibratorio tympanorum*. Novi Commentari Acad Petropolit, 1766. **10**: p. 243–260
- [33]. Vlasov, V.Z., *General theory of shells and its applications in engineering*. Vol. 99. 1964: National Aeronautics and Space Administration.

- [34]. S.Timoshenko, *Theory of Plates and Shells*, ed. E.M. Series. 1940, M cGraw-Hill.: Pitman. Hallert, B. Shewell, HAL. .
- [35]. Zienkiewicz, O., Cheung, YK, *The finite element method in structural and continuum mechanics*. Numerical Solution of Problems in Structural and Continuum Mechanics, 1967: p. 245.
- [36]. Cui, X., et al., *A smoothed finite element method (SFEM) for linear and geometrically nonlinear analysis of plates and shells*. Comput Model Eng Sci, 2008. **28**(2): p. 109-125.
- [37]. Liu, G., K. Dai, and T. Nguyen, *A smoothed finite element method for mechanics problems*. Computational Mechanics, 2007. **39**(6): p. 859-877.
- [38]. Zozulya, V., *Numerical solution of the Kirchhoff plate bending problem with BEM*. ISRN Mechanical Engineering, 2011. **2011**.
- [39]. Providakis, C.P. and D.E. Beskos, *Dynamic analysis of plates by boundary elements*. Applied Mechanics Reviews, 1999. **52**(7): p. 213-236.
- [40]. Jin, W., Y. Cheung, and O. Zienkiewicz, *Trefftz method for Kirchhoff plate bending problems*. International Journal for Numerical Methods in Engineering, 1993. **36**(5): p. 765-781.
- [41]. Jirousek, J., *Hybrid-Trefftz plate bending elements with p-method capabilities*. International journal for numerical methods in engineering, 1987. **24**(7): p. 1367-1393.
- [42]. Man, H., et al., *High-order plate bending analysis based on the scaled boundary finite element method*. International Journal for Numerical Methods in Engineering, 2013. **95**(4): p. 331-360.
- [43]. Silvester, P., et al. *Exterior finite elements for 2-dimensional field problems with open boundaries*. in *Proceedings of the Institution of Electrical Engineers*. 1977. IET.
- [44]. Song, C. and J.P. Wolf, *CONSISTENT INFINITESIMAL FINITE-ELEMENT CELL METHOD: THREE-DIMENSIONAL VECTOR WAVE EQUATION*. International Journal for Numerical Methods in Engineering, 1996. **39**(13): p. 2189-2208.
- [45]. Wolf, J.P. and C. Song, *Finite-element modelling of unbounded media*. 1996: Wiley Chichester.
- [46]. Song, C. and J.P. Wolf, *Body loads in scaled boundary finite-element method*. Computer Methods in Applied Mechanics and Engineering, 1999. **180**(1): p. 117-135.
- [47]. Deeks, A. and J. Wolf, *A virtual work derivation of the scaled boundary finite-element method for elastostatics*. Computational Mechanics, 2002. **28**(6): p. 489-504.
- [48]. Yang, Z., *Fully automatic modelling of mixed-mode crack propagation using scaled boundary finite element method*. Engineering Fracture Mechanics, 2006. **73**(12): p. 1711-1731.
- [49]. Mayland, W. and W. Becker, *Scaled boundary finite element analysis of stress singularities in piezoelectric multi-material systems*. PAMM, 2009. **9**(1): p. 99-102.
- [50]. Song, H. and L. Tao, *An efficient scaled boundary FEM model for wave interaction with a nonuniform porous cylinder*. International journal for numerical methods in fluids, 2010. **63**(1): p. 96-118.

- [51]. Doherty, J.P., A.J. Deeks, and G.T. Houlsby, *Scaled Boundary Finite Element Analysis of non-homogeneous elastic half-space*. International Journal for Numerical Methods in Engineering, 2003. **57**: p. 955-973.
- [52]. Dieringer, R. and W. Becker, *Analysis of notches and cracks in circular Kirchhoff plates using the scaled boundary finite element method*. PAMM, 2012. **12**(1): p. 189-190.
- [53]. Babuška, I. and W. Rheinboldt, *Adaptive approaches and reliability estimations in finite element analysis*. Computer Methods in Applied Mechanics and Engineering, 1979. **17**: p. 519-540.
- [54]. Zhu, J., Z. Taylor, and O. Zienkiewicz, *The finite element method: its basis and fundamentals*. 2013: Elsevier.
- [55]. Deeks, A., *An adaptive h-hierarchical finite element system*. Adv. FE Procedures and Techniques, Civil-Comp, Edinburgh, 1998: p. 115.
- [56]. Rank, E. and I. Babuška, *An expert system for the optimal mesh design in the hp-version of the finite element method*. International journal for numerical methods in engineering, 1987. **24**(11): p. 2087-2106.
- [57]. Guiggiani, M. and F. Lombardi, *Self-adaptive boundary elements with h-hierarchical shape functions*. Advances in Engineering Software, 1992. **15**(3): p. 269-277.
- [58]. Charafi, A., A. Neves, and L. Wrobel, *h-Hierarchical adaptive boundary element method using local reanalysis*. International journal for numerical methods in engineering, 1995. **38**(13): p. 2185-2207.
- [59]. Deeks, A.J. and J.P. Wolf, *An h-hierarchical adaptive procedure for the scaled boundary finite-element method*. International Journal for Numerical Methods in Engineering, 2002. **54**(4): p. 585-605.
- [60]. Yang, Z., et al., *An h-hierarchical adaptive scaled boundary finite element method for elastodynamics*. Computers & Structures, 2011. **89**(13): p. 1417-1429.
- [61]. Bauchau, O. and J. Craig, *Kirchhoff plate theory*, in *Structural Analysis*. 2009, Springer. p. 819-914.
- [62]. Timoshenko, S., S. Woinowsky-Krieger, and S. Woinowsky-Krieger, *Theory of plates and shells*. Vol. 2. 1959: McGraw-hill New York.
- [63]. Bittencourt, M.L. and C. Pereiray, *Procedures for Teaching Variational Formulation and Finite Element Approximation of Mechanical Problems applied to the Kirchhoff Plate Model*. Department of Mechanical Design, State University of Campinas, Campinas, Brazil, 2004.
- [64]. Reddy, J.N., *An introduction to the finite element method*. 1993: McGraw-Hill International Editions.
- [65]. Craig, A., *Accuracy estimates and adaptive refinements in finite element computations, I*. Babuška, OC Zienkiewicz, J. Gago, ER deA. Oliviera (eds.), Wiley, Chichester, 1986. No. of pages: 408. Price:£ 49.50/\$87.15. ISBN 0-471 908622. 1987, Wiley Online Library.
- [66]. Timoshenko, S., *Theory of Plates and Shells*,(1940). Engineering Monographs Series. Schwidofsky, K.—'An outline of Photogrammetry'. Pitman. Hallert, B. Shewell, HAL.

VITA

Name: Miss. Siriporn Thongpaknum

Date of birth: February 07, 1990

Education:

2008-2012 Bachelor's degree in Civil Engineering, 2nd Class Honor, Faculty of Engineering, Thammasat University, Bangkok, Thailand.

2010-2011 Student exchange in Japan, Short-Term Exchange Program of Engineering, Saitama University, Japan

2013-2016 Master's degree student in Structural Engineering, Department of Civil Engineering, Faculty of Engineering, Chulalongkorn University, Bangkok, Thailand.

Publications:

S. Thongpaknum and J. Rungamornrat (2016). An h-hierarchical adaptive scaled boundary finite element method (SBFEM) for Kirchhoff's plate bending problems. Paper presented at the 21th National Convention on Civil engineering, June 28 - 30, 2016, BP Samila Beach Hotel, Songkhla

CHULALONGKORN UNIVERSITY